
Dynamics and Stability of Axially Lengthening and Shortening Heavy Cables with End Mass

*A thesis submitted in partial fulfilment of the requirements
for the degree of Master of Technology*

by

Dipayan Mukherjee



DEPARTMENT OF MECHANICAL ENGINEERING
INDIAN INSTITUTE OF TECHNOLOGY KANPUR

June 2016

Certificate

It is certified that the work contained in this thesis entitled **Dynamics and Stability of Axially Lengthening and Shortening Heavy Cables with End Mass** by **Dipayan Mukherjee** has been carried out under my supervision and that it has not been submitted elsewhere for a degree.

Ishan Sharma

Associate Professor

Department of Mechanical Engineering

Indian Institute of Technology Kanpur

June 2016

Abstract

We investigate dynamics and stability of axially lengthening/shortening heavy cables, used in deployment of aerostats. First, we model the cable to be a linear string and consider its configuration as vertical. We model the aerostat to be a rigid sphere, which is attached to the top of the cable. Asymptotic analysis of a reduced-order model in the limit of lengthening/shortening rates to be small gives good approximations. Investigation of stability of lengthening cables reveals that the system always goes unstable after a certain time, depending on rate of its deployment. Through stability analysis, shortening cables are found to be *inherently unstable*. Aerostat system, subjected to aerodynamic forces are investigated through computations. We obtain frequency domain responses for lengthening/shortening cables, subjected to periodic forcing. Finally, we investigate some practical cases of deployments with non-constant rates.

In the second part of the thesis, the cable is modeled to be a geometrically exact (GE) beam. Stability of unperturbed, lengthening cables are found to be dependent upon extensibility of the cable. Consequently, inextensible, unperturbed/slightly perturbed GE cables are found to be behaving like linear elastic cables. Stability of lengthening cables are affected by large initial perturbations and also by aerodynamic forces. Frequency domain response of base-excited, lengthening cables shows a sub-frequency resonance and broadening of resonance bandwidths with rate of deployment. A reduced-order model of the system reveals that the sub-frequency resonance is captured due to the fundamental consideration of an additional rotational degree-of-freedom in GEBT. Resonance bandwidths broaden with rate of lengthening/shortening due to continuous decrease/increase in the natural frequencies of lengthening/shortening cables, respectively.

Acknowledgements

I would like to extend my sincere gratitude to my thesis supervisor Prof. Ishan Sharma. His guidance and motivation helped me a lot in this endeavour. Our discussions were never bounded in the narrow domain of this thesis. His way of thinking, academic penchant always motivated me. I would also like to thank Prof. Shakti S. Gupta for his guidance and critical remarks on my work, throughout the period of thesis work.

I am thankful to my seniors Mr. Abhinav R. Dehadrai and Mr. Venugopala S. Punati. They helped me a lot to sort out various technical/non-technical issues, I have faced in this venture. Finally, I would like to thank all my friends at IIT Kanpur.

Dipayan Mukherjee

Contents

1	Introduction	1
1.1	Motivation	1
1.2	Vibrations and stability of lengthening/shortening linear elastic cables	2
1.3	Vibrations and stability of lengthening/shortening geometrically exact cables	4
2	Linear String Model of Lengthening/Shortening Cables	7
2.1	Introduction	7
2.2	Equations of motion	7
2.3	Non-dimensionalization	12
2.4	Summary	13
3	Slowly Lengthening/Shortening Cables: Asymptotic Approximations	14
3.1	Introduction	14
3.2	Reduced order model	14
3.3	Asymptotic Analysis	15
3.4	Energy associated with the first mode	18
3.5	Comparison with full finite element solution	19
3.6	Summary	23
4	Stability Analysis and Forced Vibrations	24
4.1	Introduction	24
4.2	Stability analysis	24
4.2.1	Stability analysis of cables lengthening at a constant rate	25
4.2.2	Instability in shortening cables	27
4.3	Forced Vibration	28
4.3.1	Aerodynamic forces	28
4.3.2	Simulations	30
4.4	Case studies	32
4.5	Summary	35
5	Geometrically Exact Modeling of Lengthening/Shortening Cables	37
5.1	Introduction	37
5.2	Kinematics	37
5.3	Equations of motion	39
5.4	Strain measures	44
5.5	Mapped coordinate system	46

5.6	Non-dimensionalization	48
5.7	Modeling the aerostat	49
5.8	Summary	51
6	Computation and Validation	52
6.1	Introduction	52
6.2	Weak form	52
6.3	Linearisation	55
6.4	Spatial discretization	56
6.5	Time marching	57
6.6	Validation of the computation routine	59
6.6.1	Pure bending of a cantilever beam	59
6.6.2	Damped vibration of a cantilever beam	60
6.6.3	Free vibrations of lengthening/shortening beams	60
6.7	Summary	64
7	Stability Analysis of Lengthening/Shortening GE Cables	65
7.1	Introduction	65
7.2	Stability analysis	65
7.3	Stability of lengthening cables	66
7.4	Comparison with linear string model	68
7.5	Effect of air flow on lengthening cables	71
7.6	Summary	73
8	Base excitation of Lengthening/Shortening GE Cables	74
8.1	Introduction	74
8.2	Modified of equations of motion	74
8.3	Frequency domain response of lengthening cables	76
8.4	Reduced-order models	77
8.4.1	Cable of constant length	77
8.4.2	Lengthening/shortening at constant rate	81
8.5	Summary	84
9	Concluding Remarks	85
A	FE Computation and Validation for Lengthening/Shortening Linear Cables	87
B	Computations of Element Matrices for GE Beams	90
C	MATLAB Code for Lengthening/Shortening GE Cables	93
	Bibliography	103

List of Figures

1.1	Schematic diagram of the aerostat system	2
2.1	(a) Schematic diagram of the system of our interest, (b) schematic diagram of the cable along with various forces acting on it, (c) free body diagram of a cable element, (d) free body diagram of the aerostat.	8
3.1	(a) Lengthening and (b) shortening cable with constant rate $\tilde{v} = 0.001$, (c) lengthening and (d) shortening cable with constant acceleration $\tilde{a} = 0.00001$. Time series response of the FE solution is shown along with approximate solution $A_0(\tau)$	20
3.2	(a) Lengthening with constant rate $\tilde{v} = 0.001$, (b) shortening with constant rate $\tilde{v} = 0.001$, (c) lengthening with constant acceleration $\tilde{a} = 0.00001$, (d) shortening with constant acceleration $\tilde{a} = 0.00001$. Computational results for evolution of first natural frequency in time is shown along with that of the natural frequency of the reduced-order model.	21
3.3	Comparison of first eigenmode shape of a cable of constant length from computation with the single-mode approximation (3.1).	21
3.4	Energies associated with the first eigenmode (from FE computation) and the assumed mode (3.1) $\tilde{E}(\tau)$. (a) Lengthening and (b) shortening with constant rate $\tilde{v} = 0.001$, (c) lengthening and (d) shortening with constant acceleration $\tilde{a} = 0.00001$	22
4.1	(color online) Variation of real and imaginary parts of the eigenvalues of the first three modes. shown at different time instants.	26
4.2	(color online) Deployment charts: (a) evolution of critical velocity in time, (b) maximum achievable elevation when the cable extends at constant rate.	27
4.3	(color online) Variation of real and imaginary parts of the eigenvalues of the first three modes, shown at different time instants.	28
4.4	(color online) (a) Steady velocity profile of air, (b) end-tip displacement of cable. The cable is lengthening from initial length $L_0 = 1\text{m}$ with a constant velocity $v = 1\text{ms}^{-1}$	30
4.5	(color online) (a) Variation of first three natural frequencies of the system in time, (b) time series response of end-tip displacement and velocity of the cable, (c) variation of total energy in time, (d) frequency domain response of the system. The cable is taken to be lengthening from an initial length $L_0 = 1\text{m}$ with a constant velocity $v = 1\text{ms}^{-1}$. The spatially uniform air flow is taken as $u = 10 \sin(\omega t)\text{ms}^{-1}$	31

4.6	(color online) (a) Variation of first three natural frequencies of the system in time, (b) time series response of end-tip displacement and velocity of the cable, (c) variation of total energy in time, (d) frequency domain response of the system. The cable is taken to be shortening from an initial length $L_0 = 100\text{m}$ with a constant velocity $v = 1\text{ms}^{-1}$. The spatially uniform air flow is taken as $u = 10 \sin(\omega t)\text{ms}^{-1}$.	32
4.7	(color online) (a) Steady air flow profile, (b) time series response for the end-tip displacement, (c) velocity profile, (d) evolution of first three eigenvalues in time. The cable is taken to be lengthening from an initial length of $L_0 = 1\text{m}$.	33
4.8	(color online) (a) Time series response for the end-tip displacement, (b) velocity profile. The cable is taken to be lengthening from an initial length of $L_0 = 1\text{m}$.	34
4.9	(color online) (a) Time series response for the end displacement, (b) evolution of first three eigenvalues in time. The cable is taken to be lengthening from an initial length of $L_0 = 1\text{m}$.	34
5.1	Reference and current configurations of a lengthening/shortening GE cable.	38
5.2	Material domains in reference and current configurations of a sliding geometrically exact beam.	39
5.3	Small strain superimposed upon a large rotation. Reference and current configurations along with the shadow beam are shown.	44
5.4	(a) The system of our interest, (b) schematic diagram of the model of the aerostat, (c) schematic diagram of the cable, showing forces, acting on its end, (d) free body diagram of the rigid sphere (model of the aerostat).	50
6.1	Flowchart of computation scheme using Newmark time marching algorithm.	58
6.2	(a) An uniform cantilever beam of $EI = 2$, subjected to a constant end-moment $M = 4\pi$, (b) the same beam, subjected to constant end-moment $M = 8\pi$.	59
6.3	(a) Profile of the transverse force, applied at the free end of the cantilever, (b) time series of damped oscillations of the cantilever.	60
6.4	Initial configuration of the cantilever beam.	61
6.5	(a) End-tip trajectory, (b) time series of the end-tip displacement, (c) evolution of the total energy in time, (d) angular momentum balance of a cantilever beam, lengthening at a rate of 0.2 ms^{-1} from an initial length $L_0 = 10 \text{ m}$.	62
6.6	(a) End-tip trajectory, (b) time series of the end-tip displacement, (c) evolution of the total energy in time, (d) angular momentum balance of a cantilever beam, shortening at a rate of 0.2 ms^{-1} from an initial length $L_0 = 10 \text{ m}$.	63
7.1	(color online)(a) Time series of end-tip deflection, (b) evolutions of first three eigenvalues in time of a cable, lengthening at $v = 12 \text{ ms}^{-1}$. (c) Time series of end-tip deflection, (d) evolutions of first three eigenvalues in time of a cable, lengthening at $v = 24 \text{ ms}^{-1}$.	68
7.2	Deployment charts: (a) variation of maximum rate of deployment v with time, (b) maximum achievable elevation with v .	69
7.3	(color online)Deployment charts (a) t^* vs. v plot for GE cables of various E^* along with the t^* vs. v plot for the linear cable model, (b) v vs. h^* plot for GE cables of various E^* and that for linear cable model.	69

7.4	(color online)(a) Modified deployment chart for inextensible GE cables, subjected to initial perturbations F_0 , (b) perturbed profile of the cable after applying F_0 at the end, (b)(inset) variation of perturbation with time.	70
7.5	(a) Atmospheric air flow data obtained from along with the curve fitted to it, (b) End trajectory of a lengthening cable, subjected to aerodynamic loading.	71
7.6	Modified deployment chart for cables, subjected to steady air flow Fig 7.5(a)	72
7.7	(color online)(a) Unperturbed air flow profile along with the perturbed profile (7.4), (b) modified deployment chart for various A_0	72
8.1	Schematic of a lengthening/shortening cable, subjected to base excitation in the transverse direction.	75
8.2	(color online)Frequency domain response of lengthening cables for different rates of lengthening \tilde{v}	76
8.3	Variation of natural frequencies of (8.8) with ϵ , (a) real parts of natural frequencies, (b) imaginary parts of natural frequencies.	79
8.4	(color online) Comparison of computationally obtained frequency domain response of the system with that of the reduced order model.	80
8.5	(color online) Comparison of computed second resonant frequency of the system with the second natural frequency of the reduced order model for $\epsilon = 0$, with stiffness ratio E^*	80
8.6	(a) Evolution of $\omega_{GE}^{(1)}$ and $\omega_{GE}^{(2)}$ with time, (b) computed frequency domain response of a cable, lengthening at a rate of $\tilde{v} = 0.005$ upto $\bar{t} = 100$. (c) Evolution of $\omega_{GE}^{(1)}$ and $\omega_{GE}^{(2)}$ with time, (d) computed frequency domain response of a cable, lengthening at a rate of $\tilde{v} = 0.05$ upto $\bar{t} = 100$	82
8.7	(a) Evolution of $\omega_{GE}^{(1)}$ and $\omega_{GE}^{(2)}$ with time, (b) computed frequency domain response of a cable, shortening at a rate of $\tilde{v} = 0.005$ upto $\bar{t} = 100$. (c) Evolution of $\omega_{GE}^{(1)}$ and $\omega_{GE}^{(2)}$ with time, (d) computed frequency domain response of a cable, shortening at a rate of $\tilde{v} = 0.0075$ upto $\bar{t} = 100$	83

List of Tables

4.1	Perturbed motions	25
7.1	Physical data, used in computation	67
A1	Physical data, used in computation and approximation	89
A2	Validation of the FE solution and convergence check. The number of elements, taken in the computations is denoted by n	89

উৎসর্গ
আমার স্বর্গীয় দাদু-ঠাম্মাকে...

To my late grandparents...

Chapter 1

Introduction

1.1 Motivation

Axially translating continua with varying length give rise to rich dynamics ([Chung et al., 2001](#); [Parker, 1999](#); [Wickert and Mote, 1990](#); [Gosselin et al., 2007](#)). Vertically lengthening and shortening heavy cables are important examples, as they find application in a wide range of engineering problems, for example, as tethers of high-altitude balloons (aerostats), elevator ropes ([Terumichi et al., 1997](#); [Zhu and Ni, 2000](#)), etc. In this thesis, we investigate vibrations and stability of lengthening/shortening heavy cables with specific application to the deployment/retraction of aerostats; see [Fig. 1.1\(a\)](#). Experiments on deployment of aerostats were conducted at IIT Kanpur by Defence Research and Development Organization (DRDO) in 2012. These experiments revealed that the aerostat system goes unstable while deployment and thus, unable to achieve the desirable elevation. This motivates us to investigate dynamics and stability of deployment/retraction of the aerostat system.

We accomplish this by considering two different models of the cable. First, we consider small vibrations of a linear elastic vertical cable in the presence of gravity, having a roller-guided lower end and attached to the aerostat at the upper end. The aerostat itself is taken to be a small rigid sphere, attached to the upper end of the cable. We also consider the effect of air flow.

Next, we model the cable as a geometrically exact (GE) beam ([Simo and Vu-Quoc, 1986a,b, 1988](#); [Simo, 1985](#); [Simo and Vu-Quoc, 1986c](#)). This enables us to investigate the effect of large perturbations. Here boundary conditions of the cable remain the same and the aerostat is modeled as a rigid sphere, attached to the top.

The thesis is organised under two main parts. Part 1 addresses vibrations and stability of lengthening/shortening linear elastic cables. This is followed by Part 2, which consists of vibrations and stability of lengthening/shortening GE cables.

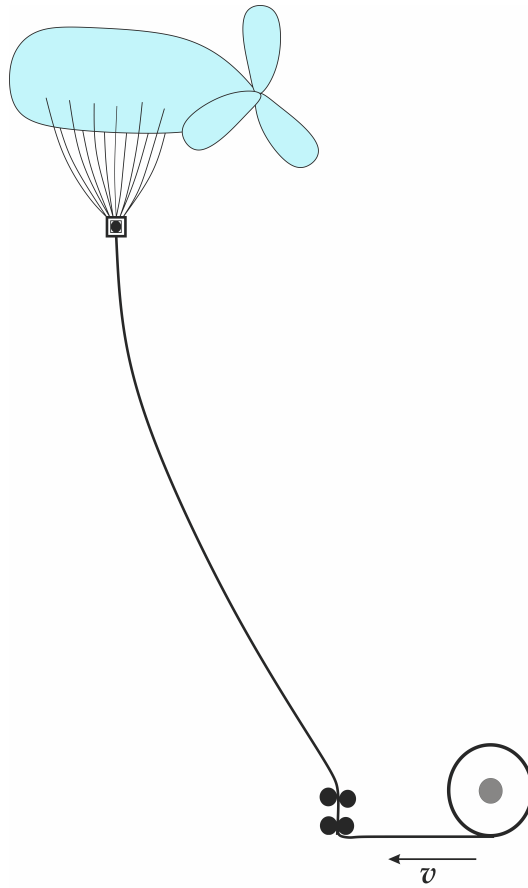


Fig. 1.1: Schematic diagram of the aerostat system

1.2 Vibrations and stability of lengthening/shortening linear elastic cables

The part is organized as follows. In [Chapter 2](#), we derive the equations of motion for linear elastic lengthening/shortening cables, from variational principle. Equations of motion for lengthening/shortening beams and cables are also derived by [Zhu and Ni \(2000\)](#).

Asymptotic approximations to single degree-of-freedom models of continuous systems often provide adequate approximations ([Roy and Chatterjee, 2009](#)). Asymptotic approximations to lengthening/shortening cables are still left unexplored. We investigate the vibrations of a slowly lengthening/shortening cable, that is amenable to asymptotics in [Chapter 3](#). We incorporate the notion of multiple time scales by considering its length to change slowly in time. The system is non-autonomous as the length of the cable changes with time. Regular multiple scales perturbation method fails for such non-autonomous systems ([Bender and Orszag, 1999](#), p. 556-559). This limitation of multiple scales method may be overcome by using WKB method ([Bender and Orszag, 1999](#), p. 556-559); ([Hinch, 1991](#), p. 127-129).

Axially translating continua are susceptible to instabilities ([Chung et al., 2001](#); [Parker, 1999](#);

Wickert and Mote, 1990; Gosselin et al., 2007). We also expect the cable may become unstable while lengthening/shortening. We employ Lyapunov's method (LaSalle and Lefschetz, 1961) to investigate the stability of lengthening/shortening cables. This method is widely used in stability analysis of axially translating continua (Wickert and Mote, 1990); (Hagedorn and Dasgupta, 2007, p. 57-61) and also employed by Gosselin et al. (2007) to analyse stability of extruding beams in highly viscous fluids and by Nawrotzki and Eller (2000) to analyse stability of nonlinear structures.

We also make some critical remarks on *inherent instability* of shortening cables. Instability of shortening cables is explained in light of temporal evolution of its total energy by Zhu and Ni (2000). Total energy of such non-Hamiltonian system does not remain constant. Thus, investigation of total energy and its evolution in time is not a common practice to investigate stability. Therefore, the *inherent instability* of shortening cables is worth of investigation by Lyapunov's direct method.

Aerodynamic forces on the aerostat play a crucial role in the dynamics of the cable. We investigate forced vibration of lengthening/shortening cables in Chapter 4. We approximate the aerostat to be a small rigid sphere, in an inviscid, non-uniform and unsteady flow. We rely on some existing mathematical models of dynamics of rigid sphere, submerged completely into a fluid. First mathematical model of this is proposed in (Tchen, 1947). This model incorporates several effects on the sphere — comprising of the effects of pressure gradient, Stokes drag and added mass. Later, some correction terms for the viscous drag on the sphere is introduced in (Corrsin and Lumley, 1956; Maxey and Riley, 1983). We consider the model by Tchen (1947) and perform further simplification by assuming air as an inviscid fluid.

Finally, we conclude by investigating some cases of non-constant deployment rates. Here we also consider the effect of air flow on the system.

We now mention some existing literatures on dynamics of axially translating continua. Equations of motion for sliding geometrically-exact beams are derived from first principles in (Vu-Quoc and Li, 1995). Finite element analysis and energy estimation for continua with arbitrarily changing length in time is done in (Zhu and Ni, 2000). Stability analysis of extending and retracting beams and cables on the basis of variation in total energy is presented by Zhu and Ni (2000). Studies on instability of axially moving strings, based on the change in eigenvalues with translational velocity are presented in (Chung et al., 2001; Parker, 1999; Wickert and Mote, 1990). Distortion in the mode shapes and existence of complex eigenmodes for axially moving continua are reported in (Wickert and Mote, 1990, 1991). Nonlinear analysis of strings with changing length and parametric excitation is done in (Kumaniecka and Nizioł, 1994; Terumichi et al., 1997). Dynamics of a beam with variable length is studied and some analytical approximations are presented in (Cooper, 1993; Tabarrok et al., 1974). Energy estimates of an axially moving continua is given by Wickert and Mote Jr (1989). The notion of vibration control of an axially translating beam is introduced in (Tadikonda and Baruh, 1992; Zhu et al., 2001). Vibrations of a cantilever beam of variable length, contacting with a flat surface is considered in

(Roy and Chatterjee, 2009).

1.3 Vibrations and stability of lengthening/shortening geometrically exact cables

Engineering structures often undergo large deflections. Such flexible structures cannot be modelled by the linear Euler-Bernoulli (EB) beam theory due to its fundamental assumption of small deflection. This failure of linear beam theory necessitates an alternative model to investigate the dynamics of highly flexible structures (Simo and Vu-Quoc, 1986a,b, 1988; Simo, 1985; Simo and Vu-Quoc, 1986c). In Part 2, we investigate stability and vibrations of the aerostat system by modeling the cable to be a geometrically exact beam.

Geometrically exact beams are widely used to model such flexible structures (Simo and Vu-Quoc, 1986a,b, 1988; Simo, 1985; Simo and Vu-Quoc, 1986c). In Chapter 5 we derive equations of motion for lengthening/shortening GE beams following (Vu-Quoc and Li, 1995). This formulation assumes large rotation, followed by small deformation of a beam element. The formulation is typically done in the inertial frame so that the inertia operator becomes uncoupled and linear; see (Simo and Vu-Quoc, 1986a). The non-linearity in the formulation comes in the stiffness operator, because the potential energy functional is highly non-linear. The strain measure, adopted in (Simo and Vu-Quoc, 1986a) is invariant under superposed rigid body motions. This property of the strain measure is the key behind the success of GEBT. This strain measure is proposed in some classical works on non-linear theories of rod (Antman, 1973; Reissner, 1973; Simo, 1985). The highly non-linear equations of motion of GE cables are solved by computation. Full computational algorithm for GE beams is developed in Chapter 6 following (Simo and Vu-Quoc, 1986b; Vu-Quoc and Li, 1995). Some alternative computation algorithms of non-linear elastic rods are presented in (Brand and Rubin, 2007; Cao et al., 2006; Jung et al., 2011; Betsch and Steinmann, 2002). Numerical investigation of forced vibration of GE cantilever beams is presented in (Cao and Tucker, 2008). Objective of the current work is to investigate stability, followed by frequency domain response of lengthening/shortening GE cables. We use computation as a tool to investigate this physical problem and to compare the computed responses with that of the reduced order model.

We investigate stability of lengthening/shortening GE cables in Chapter 7. Stability of nonlinear structures are typically analysed through linear stability analysis about a particular configuration (Nawrotzki and Eller, 2000). Stability of lengthening/shortening GE cables are not investigated in any existing work. Thus, adequate attention is given in stability analysis of lengthening/shortening GE cables in this thesis.

We conclude by investigating frequency domain response of lengthening/shortening GE cables, subjected to base excitations in Chapter 8. Base excitation of flexible structures are investigated

both experimentally and through computations by [González-Cruz et al. \(2016\)](#). However, base excitation of lengthening/shortening cables are not investigated in any of the existing literatures as per best of our knowledge. We first depict the computed results for frequency domain response of lengthening GE cables. This is followed by a reduced-order modeling of GE cables in the limit of *small* rotations of the section. This reduced-order model helps us to investigate the key features of the frequency domain responses.

Part 1

Chapter 2

Linear String Model of Lengthening/Shortening Cables

2.1 Introduction

In this chapter, we derive the equation of motion of axially lengthening/shortening heavy cables, by modeling it to be a linear string. Linear string model is the simplest model, which may be employed to model the heavy cables, attached to the aerostat. We proceed as follows: first, we derive the equation of motion of lengthening/shortening cables through variational formulation. In this derivation, we consider the cable to be roller-guided at the bottom and to be free at the top end. Next, we model the aerostat as a rigid sphere, whose centre is connected to the end of the cable. Presence of the aerostat modify the force boundary condition at the free end of the cable. We derive the modified boundary condition at the free end of the cable by balancing linear momentum of the aerostat in transverse direction. Finally, we conclude by non-dimensionalizing the equation of motion and the boundary conditions.

2.2 Equations of motion

We derive the equations of motion for lengthening/shortening cables. [Fig. 2.1\(a\)](#) shows the system of our interest — an aerostat of mass m that is attached to an uniform cable of density ρ and cross sectional area A . We consider the rollers to be small and smooth. The length of the cable changes at a rate of $v(t) = \dot{L}(t)$, where $(\dot{})$ denotes differentiation with respect to time t . We suppress time dependence of $L(t)$ and write it as L . We model the aerostat as a rigid sphere, attached at the free end of the cable. The free body diagram of the cable is displayed in [Fig. 2.1\(b\)](#). The tension in the cable is $P(x, t)$. We present the free body diagram of a cable

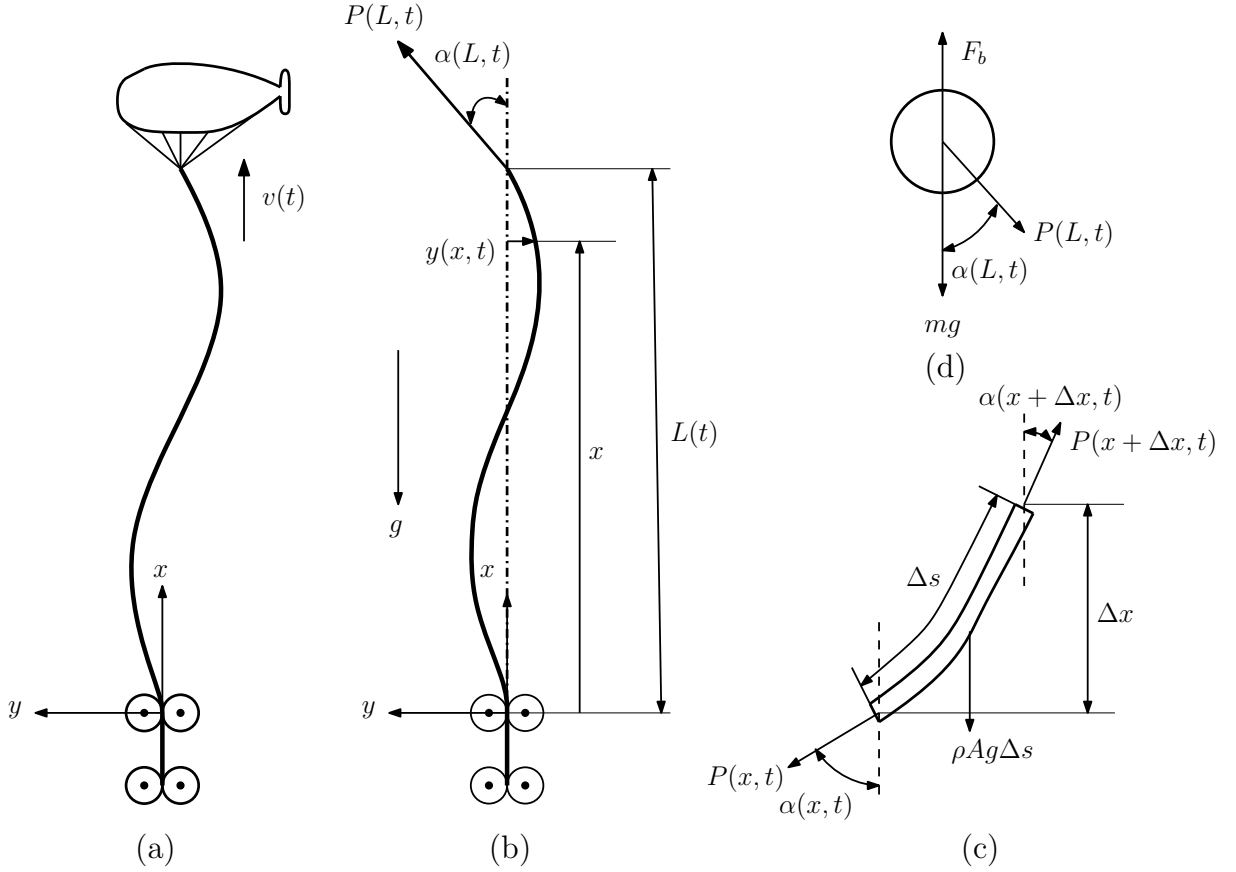


Fig. 2.1: (a) Schematic diagram of the system of our interest, (b) schematic diagram of the cable along with various forces acting on it, (c) free body diagram of a cable element, (d) free body diagram of the aerostat.

element of length Δs in Fig. 2.1(c).

To obtain the distribution of tension in the cable, we balance the axial forces for the element:

$$\rho A \Delta s \ddot{L}(t) = P(x + \Delta x, t) \cos(\alpha(x + \Delta x, t)) - P(x, t) \cos(\alpha(x, t)) - \rho A \Delta s g,$$

where $\alpha(x, t)$ is the slope of the cable. Dividing both sides of the above equation by Δx and taking the limit $\Delta x \rightarrow 0$ yields

$$\frac{\partial}{\partial x} [P(x, t) \cos(\alpha(x, t))] = \rho A (g + \ddot{L}) \frac{ds}{dx}. \quad (2.1)$$

From geometry, after imposition of small slope condition, i.e., $y(x, t)_{,x} \ll 1$, the above simplifies to

$$\frac{\partial}{\partial x} P(x, t) = \rho A (g + \ddot{L}).$$

Thus, the distribution of tension in the heavy cable is obtained by integrating the above:

$$P(x, t) = F_c(t) - \rho A (g + \ddot{L})(L - x), \quad (2.2)$$

where $F_c(t) = P(L(t), t)$ is the net upward pull on the cable acting on the upper end of the cable.

We now employ variational principles to derive the governing equation for transverse vibration of a lengthening/shortening cables. To derive equations of motion from variational principle, first we estimate kinetic and potential energies associated with the cable. Expressions for kinetic and potential energies, associated with lengthening/shortening cables are, respectively:

$$T = \frac{1}{2} \int_0^L \rho A [(y_{,t} + \dot{L} y_{,x})^2 + \dot{L}^2] dx$$

and,
$$V = \frac{1}{2} \int_0^L P(x, t) (y_{,x})^2 dx,$$

where subscripts denote partial derivative, $y(x, t)$ is the deflection, ρ and A are the density and cross sectional area of it, respectively and $P(x, t)$ is the tension in the cable. We now express the action integral as

$$\int_{t_1}^{t_2} (\delta T - \delta V) dt = 0,$$

where, $\delta(\cdot)$ is the variational operator. We note that the spatial domain of integration is changing with time. Direct attempt to derive equations of motion from this may invite additional complexity. To eschew this problem, we perform a change of variable (Roy and Chatterjee, 2009; Vu-Quoc and Li, 1995). We take $\zeta = x/L$ such that $0 \leq \zeta \leq 1$. The transverse displacement becomes $\tilde{y}(\zeta, t) = y(x, t)$. Derivatives transforms as

$$y_{,x} = \tilde{y}_{,\zeta} \frac{\partial \zeta}{\partial x} = \frac{\tilde{y}_{,\zeta}}{L}, \quad \text{and} \quad y_{,t} = \tilde{y}_{,t} + \tilde{y}_{,\zeta} \frac{\partial \zeta}{\partial t} = \tilde{y}_{,t} - \tilde{y}_{,\zeta} \frac{\zeta \dot{L}}{L}.$$

The modified expressions for kinetic and potential energies are then

$$T = \frac{1}{2} \int_0^1 \rho A L \left[\left\{ \tilde{y}_{,t} + (1 - \zeta) \tilde{y}_{,\zeta} \frac{\dot{L}}{L} \right\}^2 + \dot{L}^2 \right] d\zeta \quad (2.3)$$

and
$$V = \frac{1}{2} \int_0^1 \left[\frac{F_c(t)}{L} - \rho A (g + \ddot{L})(1 - \zeta) \right] \tilde{y}_{,\zeta}^2 d\zeta, \quad (2.4)$$

where, $F_c(t) = P(L(t), t)$ is tension in the free end of the cable. Now, the action integral becomes:

$$\begin{aligned} \frac{1}{2} \int_{t_1}^{t_2} \int_0^1 \delta \left[\rho A L \left\{ \tilde{y}_{,t} + (1 - \zeta) \tilde{y}_{,\zeta} \frac{\dot{L}}{L} \right\}^2 + \rho A L \dot{L}^2 - \left\{ \frac{F_c(t)}{L} \right. \right. \\ \left. \left. - \rho A (g + \ddot{L})(1 - \zeta) \right\} \tilde{y}_{,\zeta}^2 \right] d\zeta dt = 0. \end{aligned} \quad (2.5)$$

After some manipulations we obtain:

$$\begin{aligned}
 & \int_{t_1}^{t_2} \left[\rho AL \left\{ \tilde{y}_{,t} + (1-\zeta) \tilde{y}_{,\zeta} \frac{\dot{L}}{L} \right\} (1-\zeta) \frac{\dot{L}}{L} \delta \tilde{y} \right]_0^1 dt + \int_0^1 \left[\rho AL \left\{ \tilde{y}_{,t} + (1-\zeta) \tilde{y}_{,\zeta} \frac{\dot{L}}{L} \right\} \delta \tilde{y} \right]_{t_1}^{t_2} d\zeta \\
 & - \int_{t_1}^{t_2} \int_0^1 \left[\frac{\partial}{\partial t} \left\{ \rho AL \left(\tilde{y}_{,t} + (1-\zeta) \tilde{y}_{,\zeta} \frac{\dot{L}}{L} \right) \right\} + \frac{\partial}{\partial \zeta} \left\{ \rho A (1-\zeta) \dot{L} \left(\tilde{y}_{,t} + (1-\zeta) \tilde{y}_{,\zeta} \frac{\dot{L}}{L} \right) \right\} \right] \delta \tilde{y} d\zeta dt \\
 & \quad - \int_{t_1}^{t_2} \left[\left\{ \frac{F_c(t)}{L} - \rho A (g + \ddot{L}) (1-\zeta) \right\} \tilde{y}_{,\zeta} \delta \tilde{y} \right]_0^1 dt \\
 & \quad + \int_{t_1}^{t_2} \int_0^1 \frac{\partial}{\partial \zeta} \left[\left\{ \frac{F_c(t)}{L} - \rho A (g + \ddot{L}) (1-\zeta) \right\} \tilde{y}_{,\zeta} \right] \delta \tilde{y} d\zeta dt = 0. \tag{2.6}
 \end{aligned}$$

We see that the second term of the above equation vanishes as the initial and final configurations of the cable at $t = t_1$ and $t = t_2$, respectively, are fixed. Thus, $\delta \tilde{y}|_{t=t_1} = 0$ and $\delta \tilde{y}|_{t=t_2} = 0$. The first and fourth terms of (2.6) are defined at the boundaries. As the boundaries can be kept fixed, while the other points of the cable may vary, the summation of the integrands of the third and last terms of (2.6) must vanish. Thus,

$$\begin{aligned}
 & \frac{\partial}{\partial t} \left[L \left\{ \tilde{y}_{,t} + (1-\zeta) \tilde{y}_{,\zeta} \frac{\dot{L}}{L} \right\} \right] + \frac{\partial}{\partial \zeta} \left[(1-\zeta) \dot{L} \left\{ \tilde{y}_{,t} + (1-\zeta) \tilde{y}_{,\zeta} \frac{\dot{L}}{L} \right\} \right] \\
 & \quad - \frac{\partial}{\partial \zeta} \left[\left\{ \frac{F_c(t)}{\rho AL} - (g + \ddot{L}) (1-\zeta) \right\} \tilde{y}_{,\zeta} \right] = 0, \tag{2.7}
 \end{aligned}$$

which is the equation of motion of the system. The above equation is expanded and expressed as the following:

$$\begin{aligned}
 & \rho AL \tilde{y}_{,tt} + 2\rho A (1-\zeta) \dot{L} \tilde{y}_{,\zeta t} + \rho A (1-\zeta) \ddot{L} \tilde{y}_{,\zeta} + \rho A (1-\zeta)^2 \frac{\dot{L}^2}{L} \tilde{y}_{,\zeta \zeta} - 2\rho A (1-\zeta) \frac{\dot{L}^2}{L} \tilde{y}_{,\zeta} \\
 & \quad - \left\{ \frac{F_c(t)}{L} - \rho A (g + \ddot{L}) (1-\zeta) \right\} \tilde{y}_{,\zeta \zeta} - \rho A (g + \ddot{L}) \tilde{y}_{,\zeta} = 0.
 \end{aligned}$$

The above equation can be expressed in convenient form as

$$\begin{aligned}
 & \rho AL \tilde{y}_{,tt} + 2\rho A (1-\zeta) \dot{L} \tilde{y}_{,\zeta t} + \rho A (1-\zeta) \ddot{L} \tilde{y}_{,\zeta} + \rho A \left[(1-\zeta)^2 \frac{\dot{L}^2}{L} \tilde{y}_{,\zeta} \right]_{,\zeta} \\
 & \quad = \left[\left\{ \frac{F_c(t)}{L} - \rho A (g + \ddot{L}) (1-\zeta) \right\} \tilde{y}_{,\zeta} \right]_{,\zeta}. \tag{2.8}
 \end{aligned}$$

The left-hand side of (2.8) is same as that obtained by [Vu-Quoc and Li \(1995\)](#) for lengthening/shortening geometrically-exact rods. Geometrically-exact model of rods incorporates large rotation, followed by a small deformation of the rod. The effect of large rotation is taken care of by a nonlinear stiffness operator, which we don't obtain here. Instead, we obtain a linear stiffness operator as shown in the right hand side of (2.8). Apart from this, the equations of motion, shown in [Vu-Quoc and Li \(1995\)](#) is same as (2.8). This comparison ensures our derivation to be correct.

Boundary conditions are obtained from the boundary integrals of (2.6). The sum of the boundary integrals vanishes if:

$$\left[\rho AL \left\{ \tilde{y}_{,t} + (1 - \zeta) \tilde{y}_{,\zeta} \frac{\dot{L}}{L} \right\} (1 - \zeta) \frac{\dot{L}}{L} + \left\{ \frac{F_c(t)}{L} - \rho A (g + \ddot{L}(t)) (1 - \zeta) \right\} \tilde{y}_{,\zeta} \right]_{\zeta=0} = 0,$$

or,
$$\delta \tilde{y}|_{\zeta=0} = 0,$$

and,
$$\left[\rho AL \left\{ \tilde{y}_{,t} + (1 - \zeta) \tilde{y}_{,\zeta} \frac{\dot{L}}{L} \right\} (1 - \zeta) \frac{\dot{L}}{L} + \left\{ \frac{F_c(t)}{L} - \rho A (g + \ddot{L}) (1 - \zeta) \right\} \tilde{y}_{,\zeta} \right]_{\zeta=1} = 0,$$

or,
$$\delta \tilde{y}|_{\zeta=1} = 0.$$

Since the bottom of the cable is guided by rollers (see Fig. 2.1(b)), the variation of \tilde{y} at $\zeta = 0$ is zero. Thus, we obtain the boundary condition at $\zeta = 0$ as

$$\tilde{y} = 0. \quad (2.9)$$

In the other hand, there is no geometric constraint at the upper end of the cable. Since at $\zeta = 1$, $\delta \tilde{y} \neq 0$, the coefficient of $\delta \tilde{y}$ must vanish. Thus we obtain the boundary condition the cable at $\zeta = 1$ as

$$\frac{F_c(t)}{L} \tilde{y}_{,\zeta} = 0. \quad (2.10)$$

The presence of the aerostat at the upper end of the cable will modify the natural boundary condition at $\zeta = 1$.

To modify the boundary condition at $\zeta = 1$ and obtain the expression for the upward pull on the cable $F_c(t)$, we will balance forces on the aerostat separately; see Fig. 2.1(d). The force balances in axial and transverse directions are, respectively,

$$m\ddot{L} = F_b - mg - F_c(t) \cos(\alpha(x, t)) \quad \text{at } x = L,$$

and

$$m\tilde{y}_{,tt} = -F_c(t) \sin(\alpha(x, t)) \quad \text{at } x = L,$$

where F_b is the buoyancy force, exerted by the aerostat on the cable. We obtain net buoyancy force F_c from F_b after subtracting the weight of the aerostat $m(g + \ddot{L})$ from F_b . We now assume

$|\alpha| \ll 1$ and follow (Hagedorn and Dasgupta, 2007, p. 1-3) to obtain

$$F_c(t) = F_b - m(g + \ddot{L}) = F - m\ddot{L}, \quad (2.11)$$

and

$$my_{,tt} + F_c(t)y_{,x} = 0 \quad \text{at } x = L.$$

Combining the preceding two equations yields

$$my_{,tt} + Fy_{,x} - m\ddot{L}y_{,x} = 0 \quad \text{at } x = L, \quad (2.12)$$

where F is defined as $F = F_b - mg$. We now express (2.12) in terms of ζ as

$$m\tilde{y}_{,tt} + \frac{F}{L}\tilde{y}_{,\zeta} - m\frac{\ddot{L}}{L}\tilde{y}_{,\zeta} = 0 \quad \text{at } \zeta = 1. \quad (2.13)$$

The above equation represents the natural boundary condition for the system at $\zeta = 1$. We now have the partial differential equation (2.8), governing the system along with the boundary conditions (2.9) and (2.13).

We substitute (2.11) into (2.8) to obtain

$$\begin{aligned} & \rho AL\tilde{y}_{,tt} + 2\rho A(1-\zeta)\dot{L}\tilde{y}_{,\zeta t} + \rho A(1-\zeta)\ddot{L}\tilde{y}_{,\zeta} + \rho A\frac{\partial}{\partial\zeta}\left[(1-\zeta)^2\frac{\ddot{L}^2}{L}\tilde{y}_{,\zeta}\right] \\ & = \frac{\partial}{\partial\zeta}\left[\left\{\frac{F}{L} - m\frac{\ddot{L}}{L} - \rho A(g + \ddot{L})(1-\zeta)\right\}\tilde{y}_{,\zeta}\right]. \end{aligned} \quad (2.14)$$

We now non-dimensionalize the above equation along with the boundary conditions (2.9) and (2.13) in the next section.

2.3 Non-dimensionalization

We non-dimensionalize the (2.14) and express it as

$$l\eta_{,\bar{t}\bar{t}} + 2(1-\zeta)\dot{l}\eta_{,\zeta\bar{t}} + (1-\zeta)\ddot{l}\eta_{,\zeta} + \frac{\partial}{\partial\zeta}\left[(1-\zeta)^2\frac{\dot{l}^2}{l}\eta_{,\zeta}\right] = \frac{\partial}{\partial\zeta}\left[\left\{\frac{1}{l} - \tilde{m}\frac{\ddot{l}}{l} - \left(\frac{1}{\bar{F}} + \ddot{l}\right)(1-\zeta)\right\}\eta_{,\zeta}\right], \quad (2.15)$$

where the non-dimensional deflection is:

$$\eta(\zeta, \bar{t}) = \tilde{y}(\zeta, t)/L_0,$$

in terms of initial length of the cable L_0 , the non-dimensional time is

$$\bar{t} = t\frac{1}{L_0}\sqrt{\frac{F}{\rho A}},$$

total derivatives with respect to \bar{t} are again denoted by $(\dot{})$, the non-dimensional length of the cable is $l(\bar{t}) = L/L_0$, the non-dimensional net buoyancy force is $\tilde{F} = F/\rho AgL_0$, and the non-dimensional mass of the aerostat is $\tilde{m} = m/\rho AL_0$. We define the non-dimensional velocity

$$\tilde{v} = \dot{l} = \dot{L} \sqrt{\frac{\rho A}{F}},$$

where $\sqrt{F/\rho A}$ is the speed of travelling waves in a cable, kept at a constant tension F . Finally, we define a non-dimensional acceleration

$$\tilde{a} = \ddot{l} = \ddot{L} \frac{\rho A}{F}.$$

Similarly, the boundary conditions (2.9) and (2.13) are non-dimensionalized as

$$\eta = 0 \quad \text{at } \zeta = 0 \tag{2.16}$$

and
$$\tilde{m}\eta_{,\bar{t}\bar{t}} + \frac{1}{l}\eta_{,\zeta} - \tilde{m}\frac{\dot{l}}{l}\eta_{,\zeta} = 0 \quad \text{at } \zeta = 1. \tag{2.17}$$

Thus we obtain non-dimensionalized equation of motion (2.15) along with non-dimensionalized boundary conditions (2.16) and (2.17) at $\zeta = 0$ and $\zeta = 1$, respectively.

2.4 Summary

In this chapter, equation of transverse vibrations of lengthening/shortening cables, is derived, along with boundary conditions. We will now proceed as follows. First, we will analyse a reduced-order model of the system which is amenable to asymptotics in the limit of a slowly lengthening or shortening cable. We will then investigate the full system computationally, while also considering forced vibrations due to aerodynamic forces on the balloon, We will conclude with a case study.

Chapter 3

Slowly Lengthening/Shortening Cables: Asymptotic Approximations

3.1 Introduction

In this chapter, we do asymptotic approximations to free vibrations of slowly lengthening/shortening cables. We first obtain a single degree-of-freedom model of the continua by Galerkin projection. This is followed by asymptotic approximations to the system, considering the cable to be lengthening/shortening slowly in time. Finally, we compare the approximate results with finite element (FE) computations. The FE computation procedure and validation of the computation routine is discussed in [App. A](#).

3.2 Reduced order model

It is possible to make significant progress through the analysis of a reduced-order model when the cable's lengthening/shortening rate is small. To develop a reduced order model of the system we express $\eta(\zeta, \bar{t})$ as

$$\eta(\zeta, \bar{t}) = \sum_{i=0}^n W_i(\zeta) q_i(\bar{t}),$$

where $W_i(\zeta)$ is the i^{th} mode of vibration that satisfies the geometric boundary condition (2.14), and $q_i(\bar{t})$ is the temporal evolution of the mode. We now write (2.13) along with the natural boundary condition (2.15) in weighted residual form (see ([Hagedorn and Dasgupta, 2007](#), p. 47))

as

$$\begin{aligned} & \int_0^1 W_j(\zeta) \left[lW_i(\zeta)\ddot{q}_i(\bar{t}) + 2(1-\zeta)lW_i'(\zeta)\dot{q}_i(\bar{t}) + (1-\zeta)l\ddot{W}_i'(\zeta)q_i(\bar{t}) \right. \\ & \left. + \frac{\partial}{\partial \zeta} \left\{ (1-\zeta)^2 \frac{l^2}{l} W_i'(\zeta) \right\} q(\bar{t}) - \frac{\partial}{\partial \zeta} \left\{ \left(\frac{1}{l} - \tilde{m} \frac{\ddot{l}}{l} - \left(\frac{1}{\bar{F}} + \ddot{l} \right) (1-\zeta) \right) W_i' \right\} q_i(\bar{t}) \right] d\zeta \\ & + \left[W_j(\zeta) \left\{ \tilde{m} W_i(\zeta) \ddot{q}_i(\bar{t}) + \left(\frac{1}{l} - \tilde{m} \frac{\ddot{l}}{l} \right) W_i'(\zeta) q_i(\bar{t}) \right\} \right]_{\zeta=1} = 0, \end{aligned}$$

where (') denotes total derivative with respect to ζ . A reduced-order model is obtained by considering only the first mode as

$$W(\zeta) = \sin(\pi\zeta/2). \quad (3.1)$$

We replace this in the above and do a Galerkin projection; see (Hagedorn and Dasgupta, 2007, p. 47-49). This leads to a single degree-of-freedom approximation of (2.13), viz.,

$$\frac{1}{2}(2\tilde{m} + l)\ddot{q}(\bar{t}) + \frac{1}{2}l\dot{q}(\bar{t}) + \frac{1}{2} \left\{ \frac{1}{2}\ddot{l} + \frac{\pi^2}{4l} - \frac{\pi^2}{4}\tilde{m}\frac{\ddot{l}}{l} - \left(\frac{1}{2} + \frac{\pi^2}{12} \right) \frac{l^2}{l} - \left(\frac{\pi^2}{8} + \frac{1}{2} \right) \left(\frac{1}{\bar{F}} + \ddot{l} \right) \right\} q(\bar{t}) = 0. \quad (3.2)$$

To express the above in a convenient form, we introduce the following parameters:

$$\alpha = \frac{\pi^2}{4}, \quad \beta = -\left(\frac{1}{2} + \frac{\pi^2}{12} \right), \quad \gamma = -\frac{1}{\bar{F}} \left(\frac{\pi^2}{8} + \frac{1}{2} \right), \quad \kappa = -\frac{\pi^2}{4}\tilde{m} \quad \text{and} \quad \chi = \left(\frac{1}{2} - \frac{\pi^2}{8} \right),$$

with which (3.2) becomes

$$(2\tilde{m} + l\ddot{q}(\bar{t}) + l)\dot{q}(\bar{t}) + \left\{ \chi\ddot{l} + \kappa\frac{\ddot{l}}{l} + \frac{\alpha}{l} + \beta\frac{l^2}{l} + \gamma \right\} q(\bar{t}) = 0. \quad (3.3)$$

The above equation is a single degree-of-freedom approximation of a lengthening/shortening cable. We will now investigate this reduced-order model through asymptotics.

3.3 Asymptotic Analysis

Aerostats are typically deployed slowly in practice. Because the axial velocity of the cable is small as compared to its rate of transverse vibration, we expect the system to display multiple time scales in its dynamics. Therefore, we express time in terms of multiple time scales as

$$\bar{t} = T + \tau + O(\epsilon^2),$$

where $\tau = \epsilon \bar{t}$ is the slow time scale and $0 < \epsilon \ll 1$ is a small parameter. By our assumption, $l(T, \tau) = l(\tau)$. We proceed as a typical multiple scale analysis (Bender and Orszag, 1999, p. 556-559); (Hinch, 1991, p. 127-129) to evaluate temporal derivatives in (3.3) upto $O(\epsilon^2)$

$$\begin{aligned} (2\tilde{m} + l(\tau)) \left(\frac{\partial^2}{\partial T^2} + 2\epsilon \frac{\partial^2}{\partial T \partial \tau} + \epsilon^2 \frac{\partial^2}{\partial \tau^2} \right) q(T, \tau) + \epsilon \frac{\partial l(\tau)}{\partial \tau} \left(\frac{\partial}{\partial T} + \epsilon \frac{\partial}{\partial \tau} \right) q(T, \tau) \\ + \left\{ \epsilon^2 \left(\chi + \kappa \frac{1}{l(\tau)} \right) \frac{\partial^2 l(\tau)}{\partial \tau^2} + \frac{\alpha}{l(\tau)} + \epsilon^2 \beta \frac{1}{l(\tau)} \left(\frac{\partial l(\tau)}{\partial \tau} \right)^2 + \gamma \right\} q(T, \tau) = 0. \end{aligned} \quad (3.4)$$

We now expand $q(T, \tau)$ as

$$q(t, \tau) = q_0(T, \tau) + \epsilon q_1(T, \tau) + \epsilon^2 q_2(T, \tau) + O(\epsilon^3). \quad (3.5)$$

Substituting the above in (3.4) and collecting $O(1)$ terms, we obtain:

$$\frac{\partial^2 q_0(T, \tau)}{\partial T^2} + \left\{ \frac{\alpha}{l(\tau)(2\tilde{m} + l(\tau))} + \frac{\gamma}{(2\tilde{m} + l(\tau))} \right\} q_0(T, \tau) = 0,$$

or,
$$\frac{\partial^2 q_0(T, \tau)}{\partial T^2} + \psi(\tau)^2 q_0(T, \tau) = 0, \quad (3.6)$$

where we define
$$\psi(\tau) = \left\{ \frac{\alpha}{l(\tau)(2\tilde{m} + l(\tau))} + \frac{\gamma}{(2\tilde{m} + l(\tau))} \right\}^{(1/2)}.$$

The solution of the (3.6) is $q_0(T, \tau) = B_0(\tau)e^{i\psi(\tau)T} + \bar{B}_0(\tau)e^{-i\psi(\tau)T}$.

We now collect $O(\epsilon)$ terms in (3.4):

$$\frac{\partial^2 q_1(T, \tau)}{\partial T^2} + \psi(\tau)^2 q_1(T, \tau) = -2 \frac{\partial^2 q_0(T, \tau)}{\partial T \partial \tau} - \frac{1}{(2\tilde{m} + l(\tau))} \frac{dl(\tau)}{d\tau} \frac{\partial q_0(T, \tau)}{\partial T}.$$

Substituting $q_0(T, \tau)$ in the above equation leads to

$$\begin{aligned} \frac{\partial^2 q_1(T, \tau)}{\partial T^2} + \psi(\tau)^2 q_1(T, \tau) = -2ie^{i\psi(\tau)T} \left[\frac{d}{d\tau} (B_0(\tau)\psi(\tau)) + iB_0(\tau)\psi(\tau)T \frac{d\psi(\tau)}{d\tau} \right. \\ \left. + \frac{1}{2(2\tilde{m} + l(\tau))} \frac{dl(\tau)}{d\tau} B_0(\tau)\psi(\tau) \right] - 2ie^{-i\psi(\tau)T} \left[\frac{d}{d\tau} (\bar{B}_0(\tau)\psi(\tau)) - i\bar{B}_0(\tau)\psi(\tau)T \frac{d\psi(\tau)}{d\tau} \right. \\ \left. - \frac{1}{2(2\tilde{m} + l(\tau))} \frac{dl(\tau)}{d\tau} \bar{B}_0(\tau)\psi(\tau) \right]. \end{aligned} \quad (3.7)$$

We cannot eliminate the secular term from the right hand side of (3.7) without setting $B_0 = 0$, due to presence of T in the secular term. In order to eliminate the secular term of (3.7), we should equate its real and imaginary components to zero. Equating the imaginary part of the

secular term of (3.7) yields

$$B_0(\tau)\psi(\tau)T\frac{d\psi(\tau)}{d\tau} = 0.$$

We note that, $\psi(\tau)$ and its derivative with respect to τ cannot be zero for all τ . Thus, the only possible solution to the above equation is $B_0(\tau) = 0$, which is trivial. This failure of multiple scale perturbation method necessitates a suitable transformation of T so that the frequency of the unperturbed oscillator is independent of the primary variables T and τ . This is accomplished through the WKB method; see (Bender and Orszag, 1999, p. 556-559) or (Hinch, 1991, p. 127-129). In the WKB method, we assume q to be of the form

$$q = q(T^*, \tau, \epsilon), \quad \text{where } T^* = \frac{1}{\epsilon}\phi(\tau).$$

and the function $\phi(\tau)$ is defined as per our convenience as the analysis continues. Here, we look for a periodic solution of q in the fast time T^* such that $q(T^*, \tau, \epsilon) = q(2\pi + T^*, \tau, \epsilon)$. By chain rule, we have

$$\begin{aligned} \frac{d(\cdot)}{dt} &= \frac{\partial\phi(\tau)}{\partial\tau} \frac{\partial(\cdot)}{\partial T^*} + \epsilon \frac{\partial(\cdot)}{\partial\tau} \\ \text{and } \frac{d^2(\cdot)}{dt^2} &= \left(\frac{\partial\phi(\tau)}{\partial\tau}\right)^2 \frac{\partial^2(\cdot)}{\partial T^{*2}} + \epsilon \left[2 \frac{\partial\phi(\tau)}{\partial\tau} \frac{\partial^2(\cdot)}{\partial T^* \partial\tau} + \frac{\partial^2\phi(\tau)}{\partial\tau^2} \frac{\partial(\cdot)}{\partial T^*} \right] + \epsilon^2 \frac{\partial^2(\cdot)}{\partial\tau^2}. \end{aligned}$$

Equation (3.4) is modified and expressed in terms of $q(T^*, \tau, \epsilon)$:

$$\begin{aligned} (2\tilde{m} + l(\tau)) &\left[\left(\frac{\partial\phi(\tau)}{\partial\tau}\right)^2 \frac{\partial^2}{\partial T^{*2}} + \epsilon \left\{ 2 \frac{\partial\phi(\tau)}{\partial\tau} \frac{\partial^2}{\partial T^* \partial\tau} + \frac{\partial^2\phi(\tau)}{\partial\tau^2} \frac{\partial}{\partial T^*} \right\} + \epsilon^2 \frac{\partial^2}{\partial\tau^2} \right] q(T^*, \tau, \epsilon) + \\ &\epsilon \frac{dl(\tau)}{d\tau} \left[\frac{\partial\phi(\tau)}{\partial\tau} \frac{\partial}{\partial T^*} + \epsilon \frac{\partial}{\partial\tau} \right] q(T^*, \tau, \epsilon) + \left[\epsilon^2 \left(\chi + \kappa \frac{1}{l(\tau)} \right) \frac{d^2 l(\tau)}{d\tau^2} + \frac{\alpha}{l(\tau)} \right. \\ &\left. + \epsilon^2 \beta \frac{1}{l(\tau)} \left(\frac{dl(\tau)}{d\tau} \right)^2 + \gamma \right] q(T^*, \tau, \epsilon) = 0. \end{aligned} \quad (3.8)$$

We collect the $O(1)$ terms from the above:

$$\left(\frac{\partial\phi(\tau)}{\partial\tau}\right)^2 \frac{\partial^2 q_0(T^*, \tau)}{\partial T^{*2}} + \psi(\tau)^2 q_0(T^*, \tau) = 0, \quad (3.9)$$

we now define $\phi(\tau)$ as

$$\phi(\tau) = \int_0^\tau \psi(\tau) d\tau, \quad \text{so that, } \frac{\partial\phi(\tau)}{\partial\tau} = \psi(\tau),$$

and this simplifies (3.9).

With this, the general solution of (3.9) is obtained as $q_0(T^*, \tau) = A_0(\tau)e^{iT^*} + \bar{A}_0(\tau)e^{-iT^*}$. To obtain $A_0(\tau)$ we collect $O(\epsilon)$ terms in (3.8):

$$\begin{aligned} \frac{\partial^2 q_1(T^*, \tau)}{\partial T^{*2}} + q_1(T^*, \tau) + \frac{2}{\psi(\tau)} \frac{\partial^2 q_0(T^*, \tau)}{\partial T^* \partial \tau} + \frac{1}{\psi(\tau)^2} \frac{\partial \psi(\tau)}{\partial \tau} \frac{\partial q_0(T^*, \tau)}{\partial T^*} \\ + \frac{1}{\psi(\tau)(2\tilde{m} + l(\tau))} \frac{dl(\tau)}{d\tau} \frac{\partial q_0(T^*, \tau)}{\partial T^*} = 0. \end{aligned} \quad (3.10)$$

In order to get periodic solutions, we collect secular terms in (3.9), i.e, coefficients of e^{iT^*} , and equate them to zero. This yields the equation

$$\frac{dA_0(\tau)}{d\tau} + \frac{1}{2\psi(\tau)} \frac{d\psi(\tau)}{d\tau} A_0(\tau) + \frac{1}{2(2\tilde{m} + l(\tau))} \frac{dl(\tau)}{d\tau} A_0(\tau) = 0, \quad (3.11)$$

for $A_0(\tau)$, whose solution is

$$A_0(\tau) = \frac{a_0}{\sqrt{\psi(\tau)(2\tilde{m} + l(\tau))}} = \frac{a_0}{\sqrt{[\alpha/l(\tau) + \gamma](2\tilde{m} + l(\tau))}}, \quad (3.12)$$

where the constant a_0 is fixed by initial conditions. This is the leading order approximation to the amplitude as a function of slow time τ . We now approximate the energy associated with the assumed mode (3.1).

3.4 Energy associated with the first mode

Total energy of lengthening/shortening cables do not remain constant in time as we are constantly adding or subtracting mass from the system. We also expect the energy, associated with the first mode (3.1) to vary with time. We have the expression of energy, associated with the cable from (2.3) and (2.4) of Chapter 2 as

$$\begin{aligned} E = \frac{1}{2} \int_0^1 \{ \rho AL + m\delta(1 - \zeta) \} \left[\left\{ \tilde{y}_{,t} + (1 - \zeta)\tilde{y}_{,\zeta} \frac{\dot{L}}{L} \right\}^2 + \dot{L}^2 \right] d\zeta \\ + \frac{1}{2} \int_0^1 \left[\frac{F - m(g + \ddot{L})}{L} - \rho A(g + \ddot{L})(1 - \zeta) \right] \tilde{y}_{,\zeta}^2 d\zeta, \end{aligned} \quad (3.13)$$

where $\delta(1 - \zeta)$ is the Dirac delta function, defined to be 1 at $\zeta = 1$ and zero otherwise. We now non-dimensionalise the above and express it as

$$\tilde{E} = \frac{1}{2} \int_0^1 \{ l + \tilde{m}\delta(1 - \zeta) \} \left[\left\{ \eta_{,t} + (1 - \zeta)\eta_{,\zeta} \frac{\dot{l}}{l} \right\}^2 + \dot{l}^2 \right] d\zeta + \frac{1}{2} \int_0^1 \left[\frac{1}{l} - \tilde{m} \frac{\dot{l}}{l} - \left(\frac{1}{\tilde{F}} + \ddot{l} \right) (1 - \zeta) \right] \eta_{,\zeta}^2 d\zeta, \quad (3.14)$$

where non-dimensional energy is defined as

$$\tilde{E} = E \frac{1}{FL_0}$$

and other non-dimensional parameters are same as defined in [Chapter 2](#). We substitute $\eta = W(\zeta)q(\bar{t})$ to the above and integrate it. We take $W(\zeta)$ to be the shape function, corresponding to the first mode as defined in [\(3.1\)](#). Thus, [\(3.14\)](#) yields upon integration

$$\tilde{E} = \frac{1}{2} \left\{ \frac{1}{2}(2\tilde{m} + l) \right\} \dot{q}^2 + \frac{1}{2} \left[\frac{1}{2} \left\{ \chi \ddot{l} + \kappa \frac{\ddot{l}}{l} + \frac{\alpha}{l} + \beta \frac{\dot{l}^2}{l} + \gamma \right\} \right] q^2 + \frac{1}{2}(l + \tilde{m})\dot{l}^2, \quad (3.15)$$

where α , β , γ , κ and χ are constants, defined earlier in this section. We take l to be varying slowly in time, i.e $l = l(\tau)$ and expand the temporal derivatives of [\(3.15\)](#) in terms of multiple time scales to obtain

$$\begin{aligned} \tilde{E} = \frac{1}{2} \left\{ \frac{1}{2}(2\tilde{m} + l(\tau)) \right\} & \left[\left(\frac{\partial}{\partial T} + \epsilon \frac{\partial}{\partial \tau} \right) q(T, \tau) \right]^2 + \frac{1}{2} \left[\frac{1}{2} \left\{ \epsilon^2 \left(\chi + \kappa \frac{1}{l(\tau)} \right) \frac{d^2 l(\tau)}{d\tau^2} + \frac{\alpha}{l(\tau)} \right. \right. \\ & \left. \left. + \epsilon^2 \beta \frac{1}{l(\tau)} \left(\frac{dl(\tau)}{d\tau} \right)^2 + \gamma \right\} \right] q(T, \tau)^2 + \frac{1}{2}(l + \tilde{m})\epsilon^2 \left(\frac{dl(\tau)}{d\tau} \right)^2. \end{aligned}$$

We now express q as $q = A_0(\tau) \cos(\psi(\tau)T)$, where $A_0(\tau)$ is the amplitude and $\psi(\tau)$ is the frequency of oscillation. Substituting q in the above we obtain

$$\tilde{E}(\tau) = \frac{1}{2}(2\tilde{m} + l(\tau)) \left[\frac{1}{2} \psi(\tau)^2 A_0^2(\tau) \sin^2(\psi(\tau)T) + \frac{1}{2} \psi^2(\tau) A_0^2(\tau) \cos^2(\psi(\tau)T) \right] + O(\epsilon)$$

or,
$$\tilde{E}(\tau) = \frac{1}{4} \left[\frac{\alpha}{l(\tau)} + \gamma g \right] A_0^2(\tau) + O(\epsilon). \quad (3.16)$$

The above expression is the leading order approximation of the total non-dimensional energy, associated with the first mode. We now compare our approximations $A_0(\tau)$, $\psi(\tau)$ and $\tilde{E}(\tau)$ with the computed solutions.

3.5 Comparison with full finite element solution

We now compare our reduced-order analysis with solutions found using finite-element (FE) analysis, which is discussed in [App. A](#). We will consider the temporal evolutions of amplitude and natural frequency corresponding to the first approximated mode $\psi(\tau)$ and the energy $\tilde{E}(\tau)$ associated with this mode.

First, we consider the envelope of oscillation $A_0(\tau)$. We perform two case studies here. First, we consider a cable that lengthens and shortens at a constant velocity $\tilde{v} = 0.001$. The results

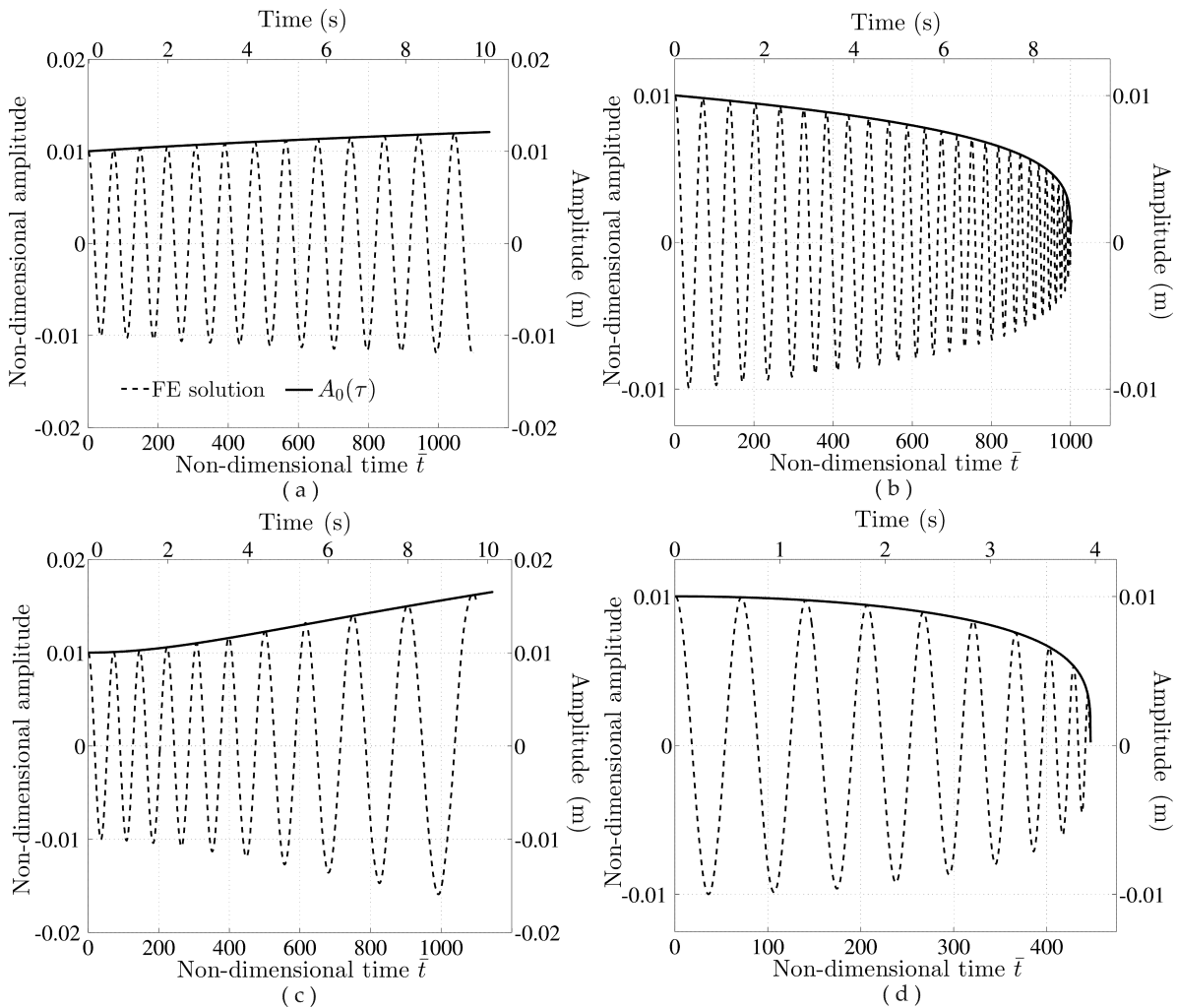


Fig. 3.1: (a) Lengthening and (b) shortening cable with constant rate $\tilde{v} = 0.001$, (c) lengthening and (d) shortening cable with constant acceleration $\tilde{a} = 0.00001$. Time series response of the FE solution is shown along with approximate solution $A_0(\tau)$.

are shown in Figs. 3.1(a) and (b), respectively. Next in Figs. 3.1(c) and (d) we consider, respectively a cable that lengthens and shortens from rest at a constant acceleration of $\tilde{a} = 0.00001$. Our results qualitatively match with that of (Zhu and Ni, 2000), whose boundary conditions, however, were different. The multiple scale analysis fails at higher velocities, as our fundamental assumption of a slowly moving cable does not hold anymore.

Evolutions of the first natural frequency obtained from FE computation and from the asymptotic analysis of the reduced-order model $\psi(\tau)$ are presented in Fig. 3.2. We note that the single-mode approximation matches the FE solution qualitatively. The deviations are due to the fact that first mode shape of the system, as obtained from FE computations is not the same as our assumed mode shape; see Fig. 3.3.

We see in Fig. 3.4 that total energy of oscillations decreases for a lengthening cable and blows up to infinity as the length tends to zero for a shortening cable. A stability analysis of axially

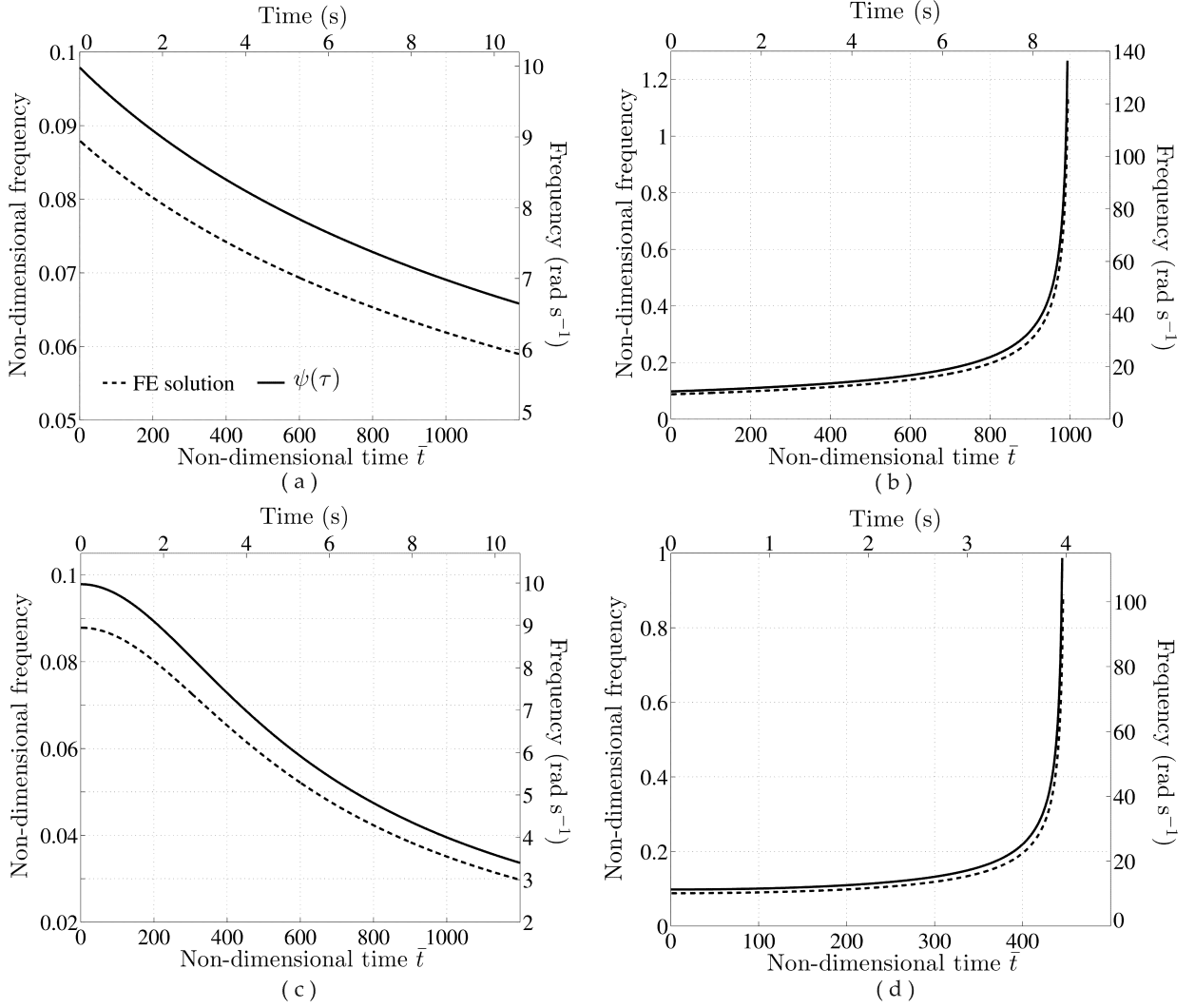


Fig. 3.2: (a) Lengthening with constant rate $\tilde{v} = 0.001$, (b) shortening with constant rate $\tilde{v} = 0.001$, (c) lengthening with constant acceleration $\tilde{a} = 0.00001$, (d) shortening with constant acceleration $\tilde{a} = 0.00001$. Computational results for evolution of first natural frequency in time is shown along with that of the natural frequency of the reduced-order model.

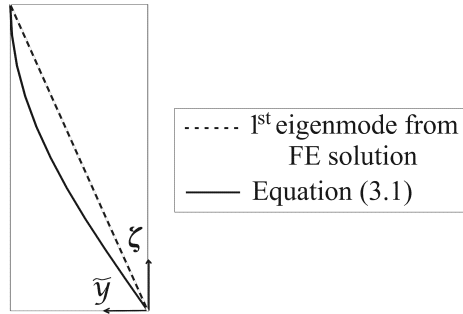


Fig. 3.3: Comparison of first eigenmode shape of a cable of constant length from computation with the single-mode approximation (3.1).

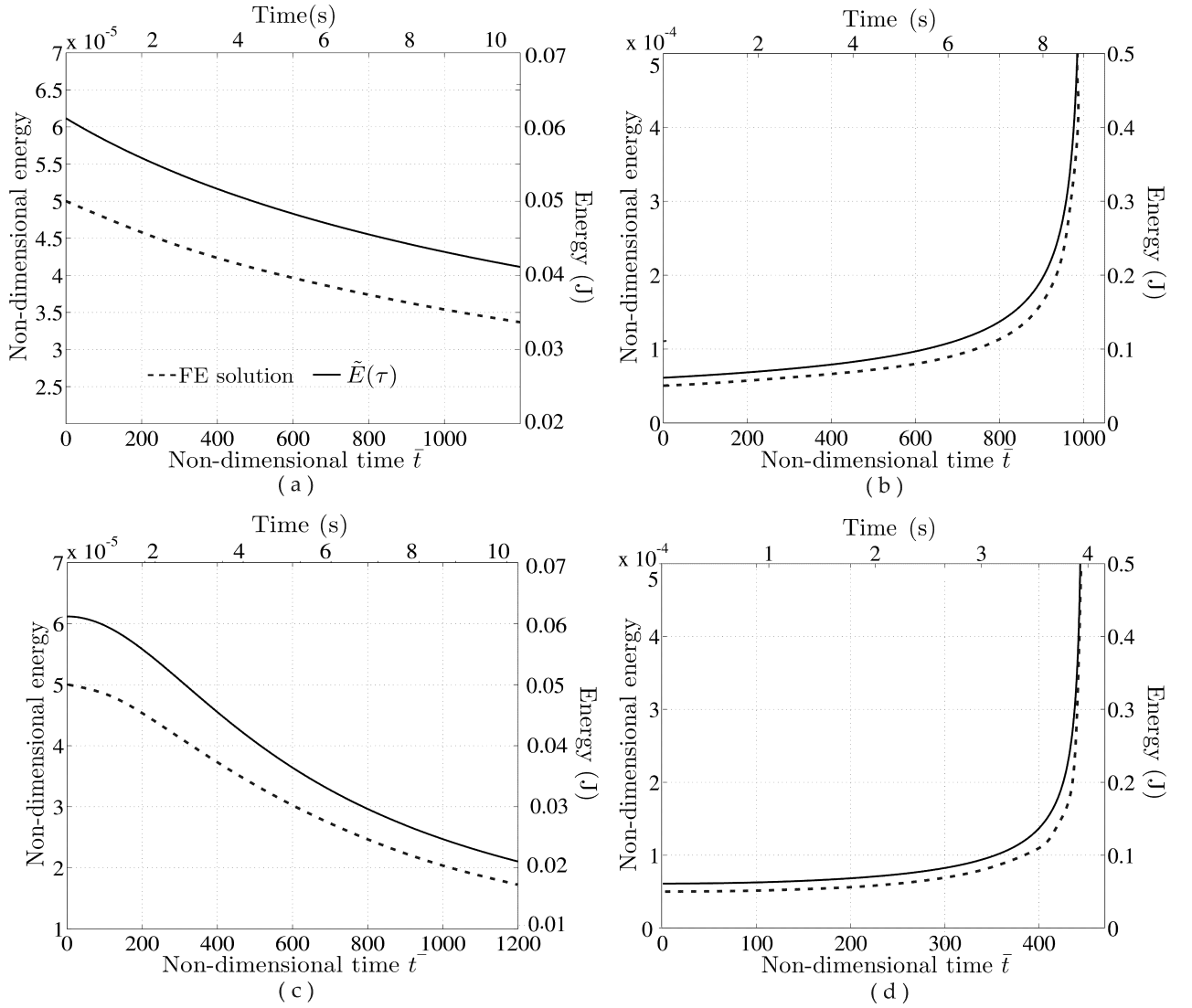


Fig. 3.4: Energies associated with the first eigenmode (from FE computation) and the assumed mode (3.1) $\tilde{E}(\tau)$. (a) Lengthening and (b) shortening with constant rate $\tilde{v} = 0.001$, (c) lengthening and (d) shortening with constant acceleration $\tilde{a} = 0.00001$.

lengthening and shortening cables, based on the evolution of total energy in time is presented in (Zhu and Ni, 2000). These authors assume that, if the total energy associated with the perturbed cable increases in time. Thus, axially shortening cables are inherently unstable. However, there is no obvious reason for an energetic stability criterion to indicate Lyapunov stability in the current non-Hamiltonian system. In the next section, we will therefore investigate stability through a spectral analysis.

3.6 Summary

In this chapter, asymptotic approximations to the single degree-of-freedom model of slowly lengthening/shortening cables are obtained. We see good match of the approximated amplitude with the computed results. Temporal evolutions of approximated first natural frequency and energy in the first mode are also matching qualitatively with the computed ones. We now proceed to investigate the stability of lengthening/shortening cables by eigenvalue analysis, in the next chapter.

Chapter 4

Stability Analysis and Forced Vibrations

4.1 Introduction

Experiments show that fast deployment of an aerostat is prone to high amplitude oscillations, especially at high elevations. Therefore, a stability analysis is of direct practical interest. We investigate stability through the linearized dynamics of the perturbed system, which is taken to be of fixed length $l^* = l(\bar{t})$ at a given instant of time \bar{t} . This *quasi static* stability analysis of continuous systems gives adequate approximation of stability limits; see (Gosselin et al., 2007; Nawrotzki and Eller, 2000). In contrast to (Zhu and Ni, 2000) this relates directly to Lyapunov's notion of linear stability (LaSalle and Lefschetz, 1961). Thus the system is perturbed from its equilibrium position $\eta(\zeta, t) = 0$. If the system oscillates about the equilibrium then it is stable, while if its deflection grows in time, then the system is unstable.

4.2 Stability analysis

To analyse the stability of the system about its equilibrium position $\eta(\zeta, t) = 0$, we proceed as follows. For FE computations, we discretize the equations in the spatial domain; see App. A. This set of linear ordinary differential equations may be represented as

$$\mathbf{M}\ddot{\mathbf{q}}(\bar{t}) + \mathbf{C}\dot{\mathbf{q}}(\bar{t}) + \mathbf{K}\mathbf{q}(\bar{t}) = 0, \quad (4.1)$$

where \mathbf{M} , \mathbf{C} and \mathbf{K} are the global mass, damping and stiffness matrices, respectively at $l = l^*$ and $\mathbf{q}(\bar{t})$ is the nodal displacements of the cable.

We now guess a solution to (4.1) as $\mathbf{q}(\bar{t}) = \mathbf{q}_0 \exp(\lambda \bar{t})$, which on substituting into (4.1) leads to

$$\lambda^2 \mathbf{M} \mathbf{q}_0 \exp(\lambda \bar{t}) + \lambda \mathbf{C} \mathbf{q}_0 \exp(\lambda \bar{t}) + \mathbf{K} \mathbf{q}_0 \exp(\lambda \bar{t}) = 0,$$

where λ is the (possibly complex) eigenvalue. As $\mathbf{q}_0 \exp(\lambda \bar{t}) \neq 0$, we obtain a polynomial eigenvalue problem as

$$\lambda^2 \mathbf{M} + \lambda \mathbf{C} + \mathbf{K} = 0 \quad (4.2)$$

We define the system to be stable whenever $\text{Re}(\lambda) \leq 0$ for all λ . The various kinds of notions that result from λ being complex are summarized in table 4.1. We will now investigate the stability

Table 4.1: Perturbed motions

$\text{Re}(\lambda) = 0, \text{Im}(\lambda) \neq 0$	Purely oscillatory solutions	Stable
$\text{Re}(\lambda) < 0, \text{Im}(\lambda) \neq 0$	Oscillatory solutions with decay	Stable
$\text{Re}(\lambda) > 0, \text{Im}(\lambda) \neq 0$	Oscillatory solutions with temporal growth	Unstable
$\text{Re}(\lambda) > 0, \text{Im}(\lambda) = 0$	Growth without oscillations	Unstable

of lengthening and shortening cables in light of this notion.

4.2.1 Stability analysis of cables lengthening at a constant rate

In this section, we consider the stability lengthening cables with constant rate. We non-dimensionalise the rate of lengthening with respect to the velocity of travelling transverse waves in the cable, that is kept at a constant tension F (as shown in Chapter 2). We plot the eigenvalues λ against the non-dimensional velocity \tilde{v} at various time instants in Fig. 4.1. We note from Fig. 4.1(a) that lengthening with a rate $\tilde{v} \geq 1$ leads immediately to instability at $\bar{t} = 0$. When $\tilde{v} \geq 1$, the rate of lengthening exceeds the velocity of travelling waves in the cable of an initial length L_0 . In this condition, the material points of the cable travel at a greater speed than that of travelling wave in it. This implies that the travelling waves cannot be reflected from any of the boundaries. Hence, the standing waves, which are formed by superposition of two travelling waves, cannot form in a cable moving at $\tilde{v} \geq 1$. Consequently, the natural frequencies of steady vibrations of the cable become zero, leading to instability (Hagedorn and Dasgupta, 2007, p. 57-61), (Wickert and Mote, 1990). It is shown in Fig. 4.1 that for a greater \bar{t} , the system becomes unstable at a lower deployment rate \tilde{v} . As the cable keeps on lengthening, the tension in it decreases at the roller end (bottom end). This is due to continuous addition of mass to the system, which increases the weight of the cable and reduces the tension at the bottom; see (2.2). The reduction in tension causes the velocity of travelling waves $\sqrt{P(0, t)/\rho A}$ at the bottom to reduce. This explains why instability initiates at a lower \tilde{v} .

The second and third eigenmodes are observed to go unstable at slightly higher \tilde{v} ; see Fig. 4.1.

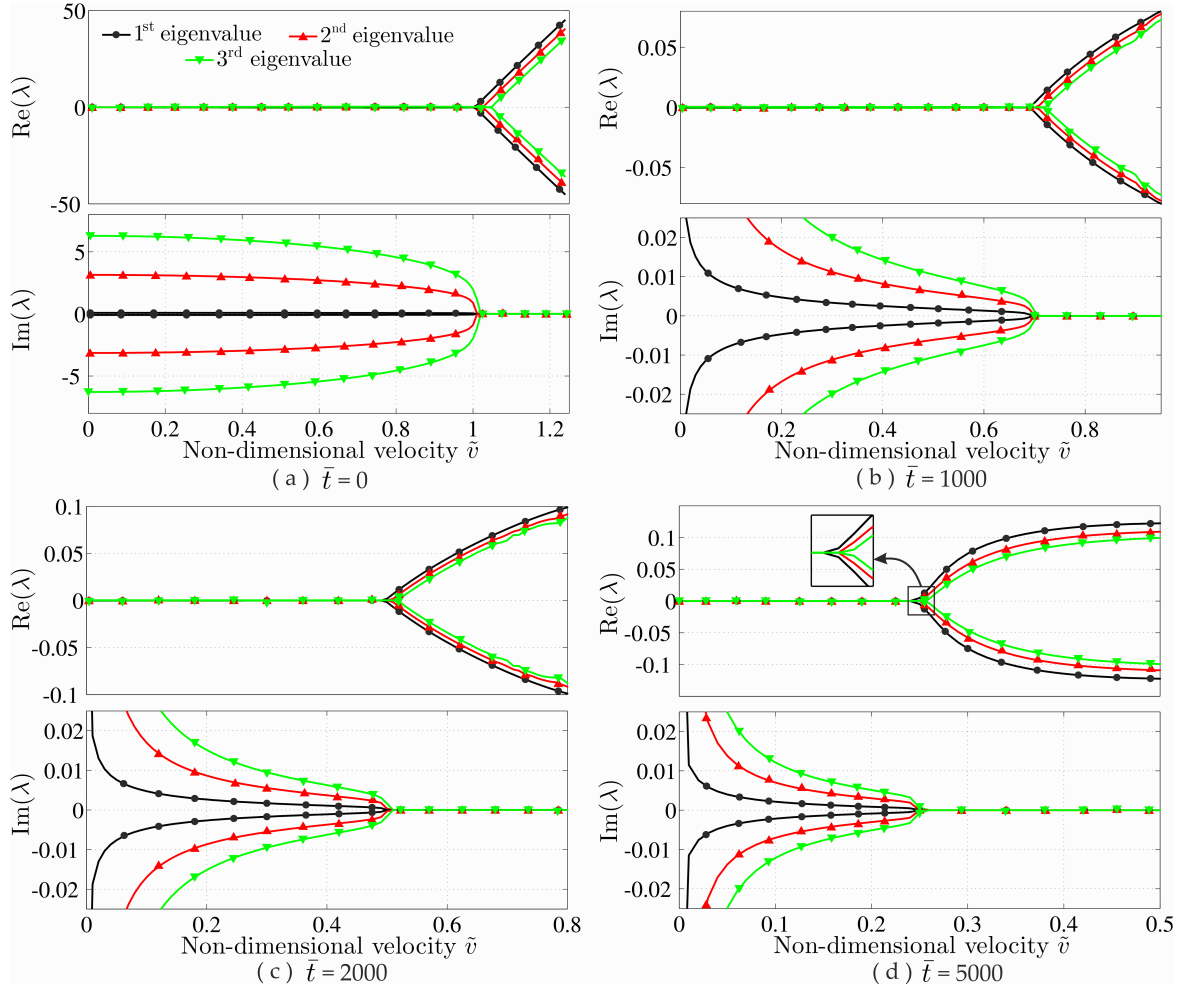


Fig. 4.1: (color online) Variation of real and imaginary parts of the eigenvalues of the first three modes. shown at different time instants.

Ideally, all the eigenmodes must go unstable simultaneously, as seen in a travelling cable of constant length (Hagedorn and Dasgupta, 2007, p. 57-61). This shift in the initiation of instability is due to discretization error in FE computation. We see in table A2 of App. A that the absolute error in the estimation of eigenfrequencies increases when computing for higher eigenmodes. This error eventually leads to the higher eigenmodes to go unstable at slightly higher \tilde{v} .

This eigenvalue analysis motivates us to develop a deployment chart for a lengthening cable in terms of a rate \tilde{v}_t , which is defined to be the minimum rate, for which instability will initiate at time \tilde{t}^* ; see Fig. 4.2(a). We also define \tilde{t}^* as the critical time at which instability sets in when the cable is deployed for a given rate \tilde{v}_t ; see Fig. 4.2(a). We note from Fig. 4.2(a) that the rate deployment of aerostats cannot be chosen arbitrarily. Rather, a particular rate of deployment (say \tilde{v}_d) should be chosen. This enables us to find out the critical time \tilde{t}_d^* corresponding to \tilde{v}_d from Fig. 4.2(a). Our analysis reveals that deployment at a rate of \tilde{v}_d is stable upto $\tilde{t} < \tilde{t}_d^*$.

We develop another deployment chart for the maximum achievable elevation (h_d^*) given a constant rate of deployment \tilde{v}_d . This h_d^* corresponds to the length of the cable at which the wave

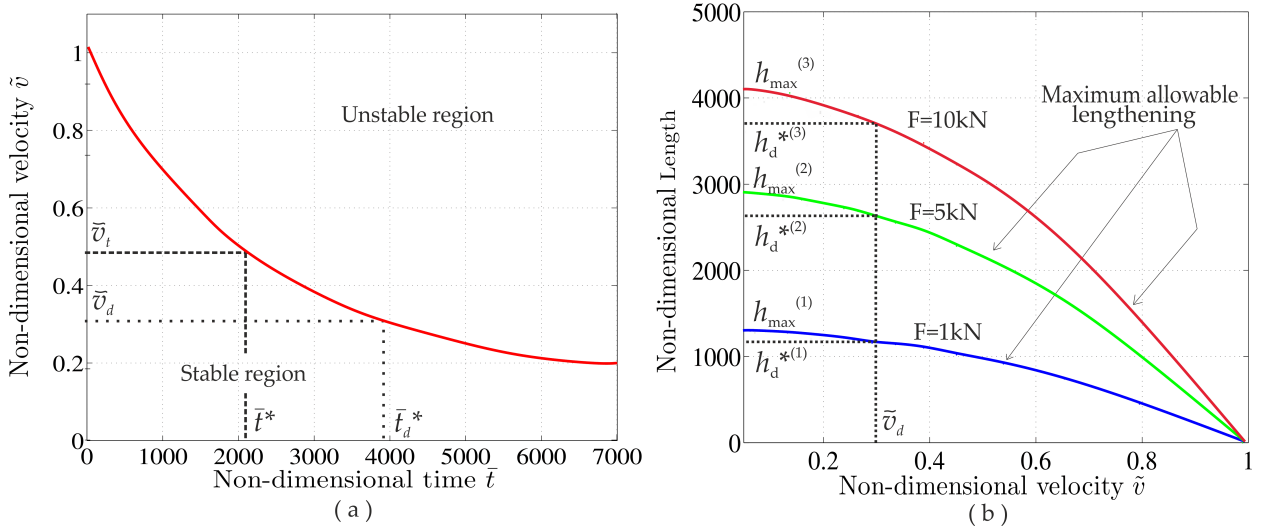


Fig. 4.2: (color online) Deployment charts: (a) evolution of critical velocity in time, (b) maximum achievable elevation when the cable extends at constant rate.

speed at the roller end becomes equal to \tilde{v}_d . The wave speed becomes zero whenever the tension at the bottom of the cable $P(0, t)$ becomes zero. In this condition, the upward buoyancy force F_b on the aerostat just balances the combined weight of itself and the cable. From Fig. 4.2(b), we see that to achieve maximum elevation, the cable should be deployed quasi-statically, i.e. with $|\tilde{v}_d| \ll 1$. However, this is not practical. As shown in Fig. 4.2(b), the maximum allowable elevation of the aerostat increases with the increasing buoyancy force, which may be attained by expanding the volume of the aerostat. If the rate of deployment and the desired elevation is given, we then may select a suitable buoyancy force as indicated in Fig. 4.2(b). For this the volume of the aerostat and its geometry may need to be optimized.

Finally, the rate of deployment of aerostats may not be constant during deployment. In Sec. 4.4, we explore the case of non-constant deployment rates.

4.2.2 Instability in shortening cables

For shortening cables, Fig. 4.3 shows that the eigenvalues always have a positive real part in all time instants. This illustrates the *inherent instability* of shortening cables. However, imaginary parts of the eigenvalues are not zero. This indicates oscillations along with growth. We also observe that the positive real part of the eigenvalues increase as length of the cable shortens, and ultimately blows up when $L \rightarrow 0$; see Fig. 4.3(d). However, we do not see any growth in amplitude of shortening cables (see Figs. 2.1(b)) and (d) as the continuum itself is shortening. The only trace of instability we find from Figs. 2.1(b)) and (d) is that the frequency of oscillation increases with shortening and eventually goes to infinity as $L \rightarrow 0$. This blowing up of frequency while shortening is also observed in Fig. 4.3, where imaginary parts of λ goes to infinity as $L \rightarrow 0$. We now move on to investigate the effect of air flow in the dynamics of the cable.

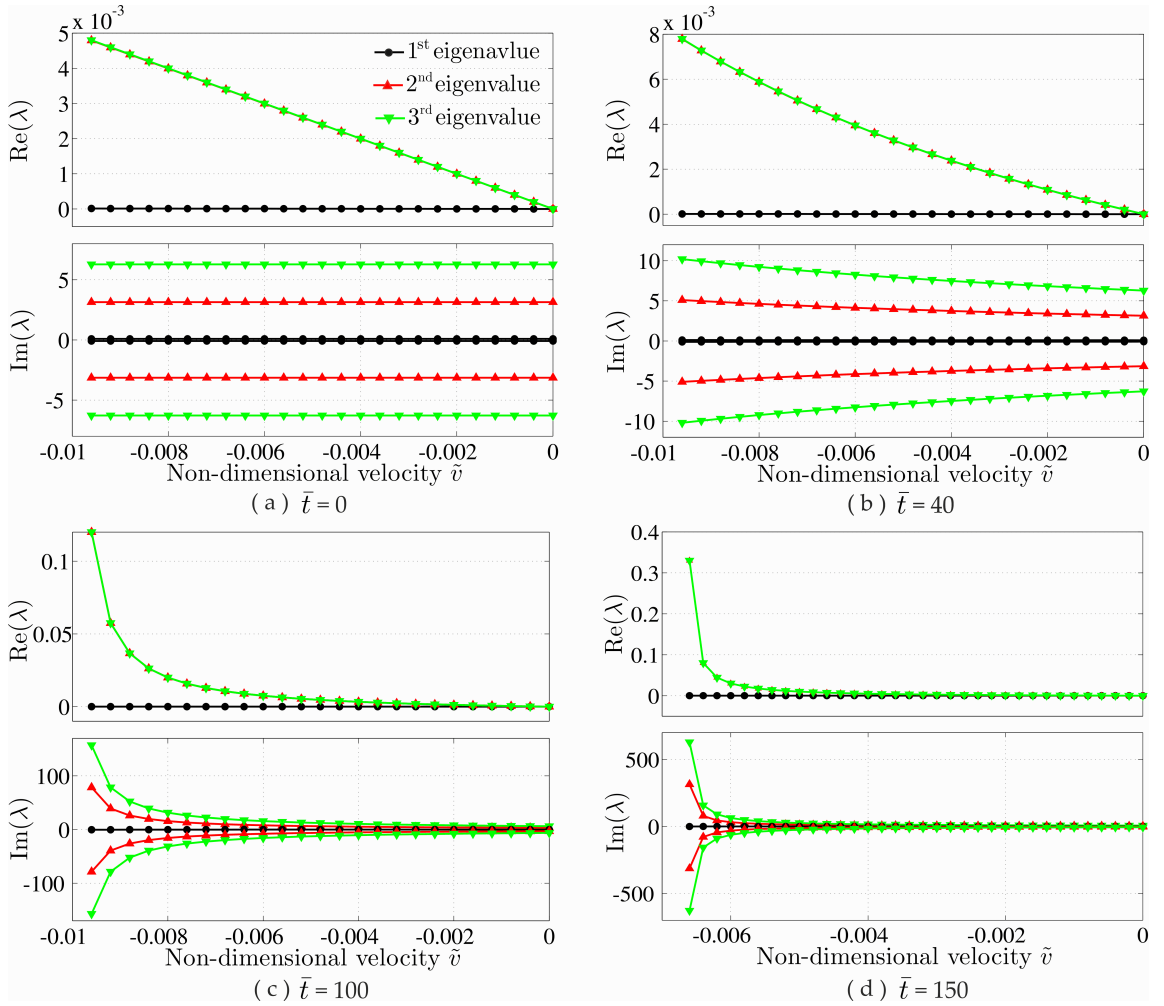


Fig. 4.3: (color online) Variation of real and imaginary parts of the eigenvalues of the first three modes, shown at different time instants.

4.3 Forced Vibration

In the previous section, we investigated instabilities during deployment/retraction of an aerostat, without incorporating external forces. We now investigate the forced response of the aerostat system. It is possible that an aerostat becomes unstable due to resonant interactions with aerodynamic forces. We first introduce a model for aerodynamic forces.

4.3.1 Aerodynamic forces

Consider a lengthening/shortening cable that is attached to an aerostat, which is modeled as a rigid sphere. For simplicity we consider air drag only on the aerostat. This is acceptable as a first approximation, because we expect the wind load on the cable to be much smaller compared to that on the aerostat. A model for the dynamics of a rigid sphere (aerostat) submerged completely

in a Newtonian fluid (air) is (Corrsin and Lumley, 1956; Maxey and Riley, 1983; Tchen, 1947):

$$m \frac{dV_i}{dt} = m_f \left[\frac{Du_i}{Dt} - \nu \Delta^2 u_i \right]_{Y(t)} - \frac{1}{2} m_f \frac{d}{dt} [V_i(t) - u_i(Y(t), t)] - 6\pi a \mu [V_i(t) - u_i(Y(t), t)] + (m - m_f) g_i + F_i^{(e)}, \quad (4.3)$$

where the subscript i represents the i^{th} component of the respective vector quantity, m_f is the mass of air displaced by the aerostat, ν and μ are kinematic and dynamic viscosities of air, respectively, \mathbf{V} is the velocity of the aerostat and \mathbf{u} is the velocity of air. The term $m_f [Du_i/Dt - \nu \Delta^2 u_i]$ on the right hand side of (4.3) is due to the pressure gradient in the air. The second term, $0.5 m_f d/dt [V_i(t) - u_i(Y(t), t)]$, is the added mass on the aerostat. The next three terms are, respectively, viscous Stokes drag, buoyancy and (non-aerodynamic) external force. The viscous drag term is first introduced by Stokes and modified afterwards.

We consider only horizontal air flow whose speed may vary vertically and with time. As μ_{air} is about $10^{-5} \text{Kg m}^{-1} \text{s}^{-1}$, we assume air to be inviscid. Because aerodynamic forces act only on the aerostat, the only change in the equations of motion will be in the boundary condition at $\zeta = 1$, i.e., (2.17). This boundary condition is now modified as

$$m \tilde{y}_{,tt} = m_f \left(u_{,t} + \frac{u}{L} u_{,\zeta} \right) - \frac{1}{2} m_f (\tilde{y}_{,tt} - u_{,t}) - \frac{F}{L} \tilde{y}_{,\zeta} + m \frac{\ddot{L}}{L} \tilde{y}_{,\zeta} \quad (4.4)$$

Non-dimensionalizing the above equation with respect to the reference length and time scales (as in Chapter 2) leads to

$$\tilde{m} \eta_{,\bar{t}\bar{t}} + \frac{1}{l} \eta_{,\zeta} - \tilde{m} \frac{\ddot{l}}{l} \eta_{,\zeta} = \tilde{m} \tilde{\rho} \left(\tilde{u}_{,\bar{t}} + \frac{\tilde{u}}{l} \tilde{u}_{,\zeta} \right) + \frac{1}{2} \tilde{m} \tilde{\rho} (\eta_{,\bar{t}\bar{t}} - \tilde{u}_{,\bar{t}}), \quad (4.5)$$

where \tilde{u} is the non-dimensional velocity of air, viz.,

$$\tilde{u} = u \sqrt{\frac{\rho A}{F}},$$

and $\tilde{\rho}$ is the ratio of density of air to that of the gas inside the aerostat:

$$\tilde{\rho} = \frac{\rho_{\text{air}}}{\rho_{\text{gas}}}.$$

This ratio originates from the ratio of the mass m_f of the air — displaced by the aerostat — to the mass m of the aerostat. We will perform computations to investigate the effect of aerodynamic forces on the aerostat. The computation scheme is the same as discussed in App. A, but now with the modified boundary condition (4.5).

4.3.2 Simulations

In all computations to follow, we take the radius of the aerostat $r = 0.5$ m and set the density of air $\rho_{\text{air}} = 1.205$ Kg m^{-3} . Instead of presenting by non-dimensional numbers, from here onwards, we present the computed results in terms of physical units to investigate the dynamics of the system.

We first consider a parabolic velocity profile of air $u(z) = \sqrt{z}\text{ms}^{-1}$, which remains constant

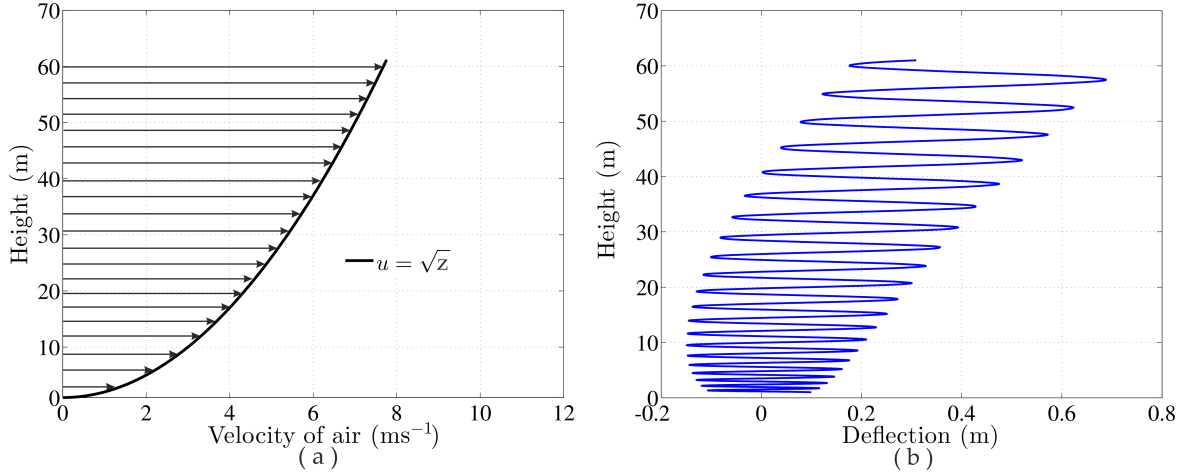


Fig. 4.4: (color online) (a) Steady velocity profile of air, (b) end-tip displacement of cable. The cable is lengthening from initial length $L_0 = 1\text{m}$ with a constant velocity $v = 1\text{ms}^{-1}$.

with time; see Fig. 4.5(a). This air flow exerts drag on the aerostat. The temporal response for a lengthening cable is shown in Fig. 4.5(b). The response is similar to that observed during free vibration, except that the mean position of the cable shifts in the direction of air flow.

We now consider an air flow, that is uniform in space but whose amplitude changes with time as $u(t) = 10 \sin(\omega_{\text{air}}t) \text{ms}^{-1}$. Again, aerodynamic effects are considered only on the aerostat. The cable extends from an initial length $L_0 = 1$ m at a constant rate $v = 1 \text{ms}^{-1}$. As the cable lengthens, natural frequencies of the system decrease with time. The temporal variations of the first three natural frequencies ω_1, ω_2 and ω_3 of the system are depicted in Fig. 4.6(a). We note from Fig. 4.6(a) that there will always be a time t^* after which one of the natural frequencies of the system will match ω_{air} . We now take $\omega_{\text{air}} = 2 \text{rad s}^{-1}$ and note the corresponding t^* from Fig. 4.6(a). As shown in Fig. 4.6(b), the system resonates when $t = t^*$. There is a sudden change in the total energy of the system at $t = t^*$ in Fig. 4.6(c). However, the amplitude of cable's end (aerostat) deflection cannot grow continuously, as the natural frequency of the system shifts from ω_{air} as time goes beyond t^* . Finally, the frequency domain response of the system is in Fig. 4.6(d). The surface shown in this figure is the envelope of the end displacements of the cable for various excitation frequencies ω_{air} . We note that large amplitude vibrations occur in the range of $0 < \omega_{\text{air}} < 4$. Our computations predict that for $\omega_{\text{air}} \geq 4 \text{rad s}^{-1}$, vibration amplitudes are not very large as they are driven by resonant interactions with the second or higher modes of

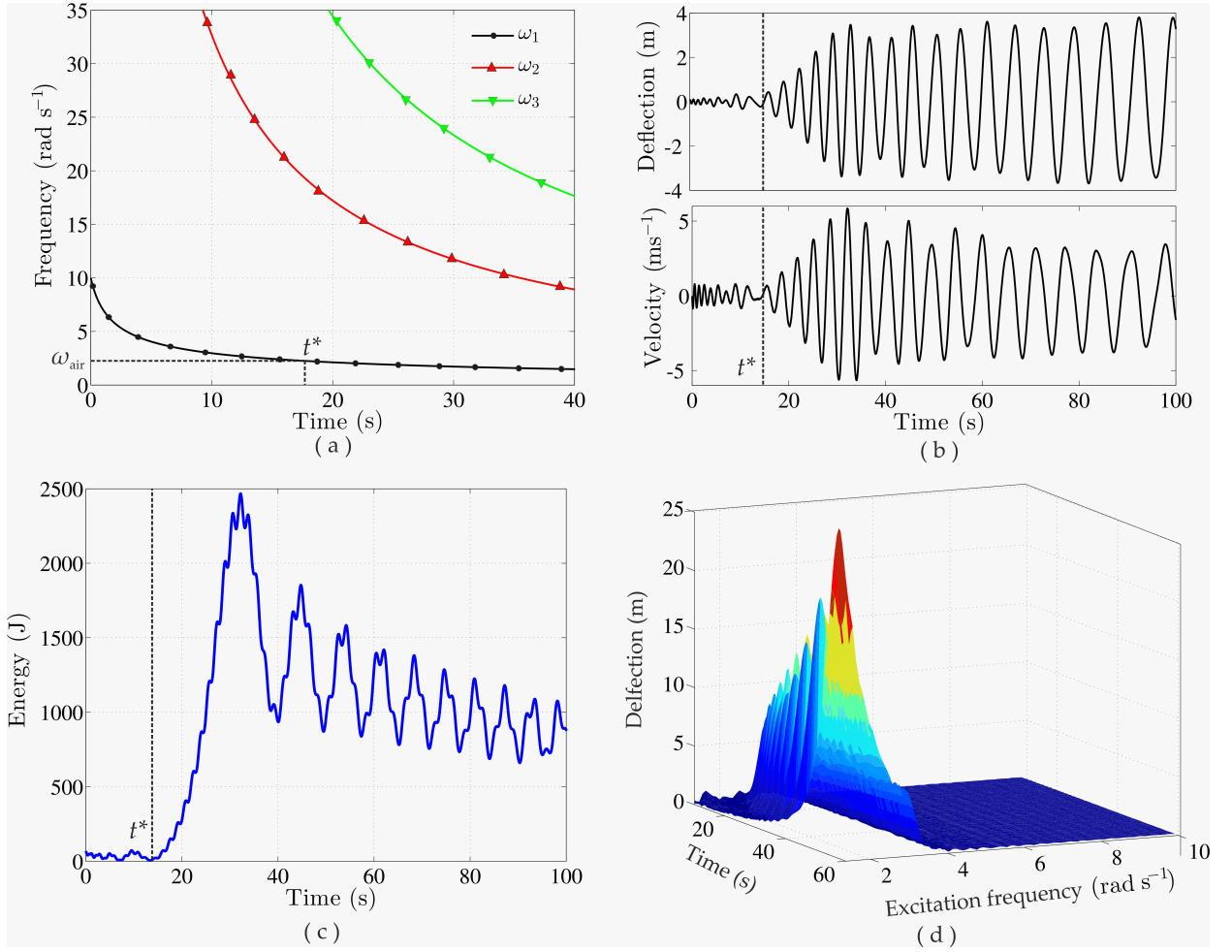


Fig. 4.5: (color online) (a) Variation of first three natural frequencies of the system in time, (b) time series response of end-tip displacement and velocity of the cable, (c) variation of total energy in time, (d) frequency domain response of the system. The cable is taken to be lengthening from an initial length $L_0 = 1\text{ m}$ with a constant velocity $v = 1\text{ ms}^{-1}$. The spatially uniform air flow is taken as $u = 10 \sin(\omega t)\text{ ms}^{-1}$.

the system.

Next, we investigate retracting cables. We take the cable to be shortening from an initial length $L_0 = 100\text{ m}$ with constant rate $v = 1\text{ ms}^{-1}$. We note from Fig. 4.7(a) that the first natural frequency for a 100 m long cable slowly grows from $\omega_1 = 1\text{ rad s}^{-1}$. Therefore, we expect resonance when $\omega_{\text{air}} \approx 1\text{ rad s}^{-1}$. We again define time t^* in Fig. 4.7(a) as the time at which $\omega_1 = \omega_{\text{air}}$. We set $\omega_{\text{air}} = 1\text{ rad s}^{-1}$ and obtain the time domain response for end deflection and velocity; see Fig. 4.7(b). We observe from Fig. 4.7(b) that the amplitude begins to grow at $t = t^*$. However, as before, the amplitude cannot grow continuously as the first natural frequency of the system shifts from ω_{air} . The total energy of a shortening cable is seen to increase with time; see Fig. 3.4(b) and Fig. 3.4(d). We find from Fig. 4.7(c) that energy now grows even more rapidly due to resonance. Finally, the frequency domain response of the system is depicted in Fig. 4.7(d). We note that amplitudes do not grow for excitation frequencies beyond 3 rad s^{-1} .

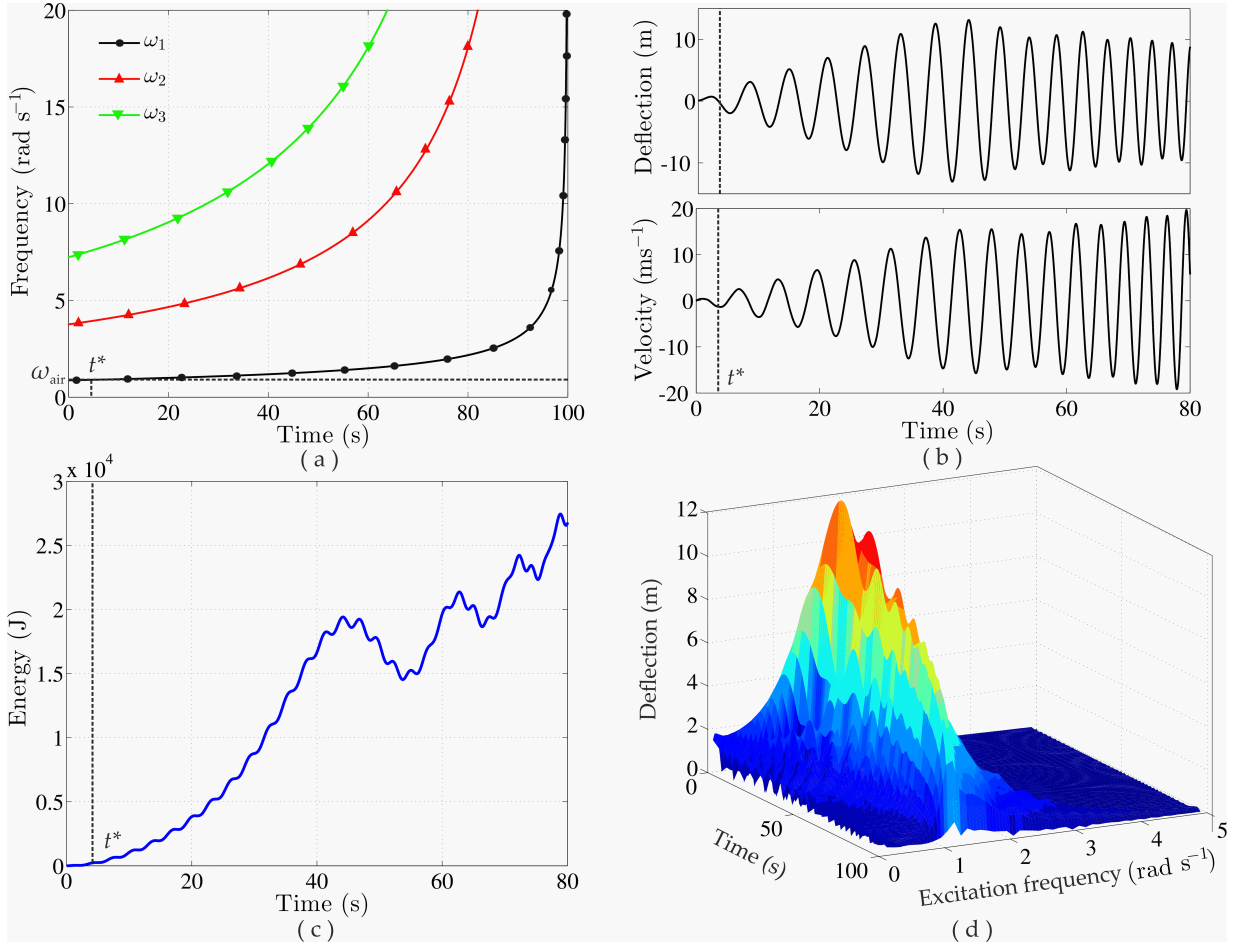


Fig. 4.6: (color online) (a) Variation of first three natural frequencies of the system in time, (b) time series response of end-tip displacement and velocity of the cable, (c) variation of total energy in time, (d) frequency domain response of the system. The cable is taken to be shortening from an initial length $L_0 = 100\text{m}$ with a constant velocity $v = 1\text{ms}^{-1}$. The spatially uniform air flow is taken as $u = 10 \sin(\omega t)\text{ms}^{-1}$.

It suggests that resonance in a shortening cable is significant only for ω_{air} near its first natural frequency ω_1 .

We end this section with two comments. The waviness in the energy plots of Figs. 4.6(c) and 4.7(c) are due to the periodic nature of the aerodynamic forcing. The waviness in the surface plots Figs. 4.6(d) and 4.7(d) are due to the waviness in the envelope of the amplitudes, as extracted directly from the simulations.

4.4 Case studies

We end this chapter by demonstrating our results through some case studies. We now present two case studies of deployment of an aerostat from an initial length $L_0 = 1\text{m}$. We note from Fig. 4.2(b) that for a constant buoyancy $F = 1\text{ kN}$, an elevation of 1.4 km could be safely

achieved at a constant deployment rate of $v = 10 \text{ ms}^{-1}$, which will correspond to $\tilde{v} \approx 0.1$. We do computations in presence of a steady air flow of $u = 0.1\sqrt[3]{z} \text{ ms}^{-1}$. The velocity profile of air is shown in Fig. 4.8(a). In the first case, the aerostat is set to deploy upto an elevation

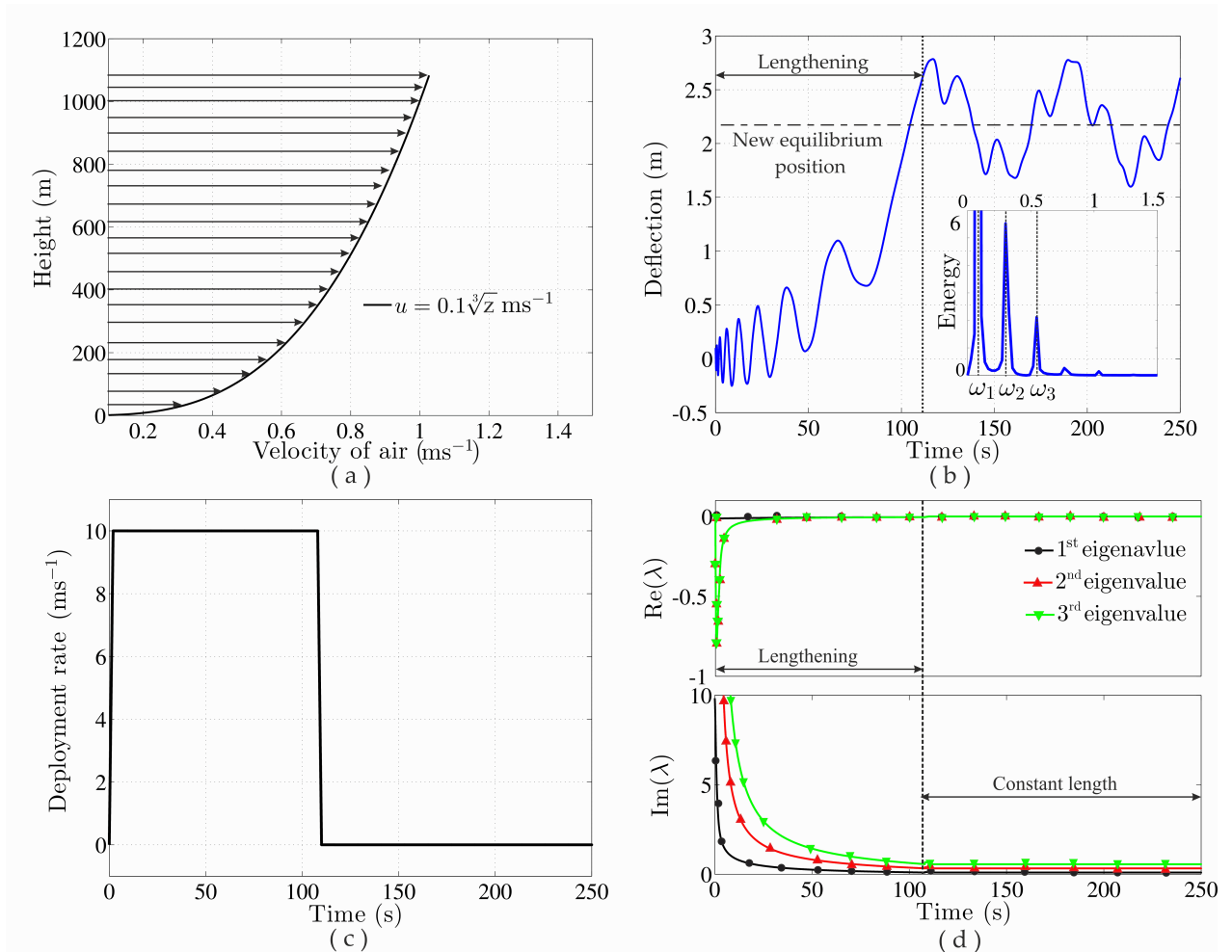


Fig. 4.7: (color online) (a) Steady air flow profile, (b) time series response for the end-tip displacement, (c) velocity profile, (d) evolution of first three eigenvalues in time. The cable is taken to be lengthening from an initial length of $L_0 = 1m$

of 1.1Km, which is less than the safe elevation limit. The deployment rate is shown in Fig. 4.8(c). We plot the time series of the oscillation of the aerostat in Fig. 4.8(b). We note that the aerostat oscillates about a shifted equilibrium while lengthening, behaving similarly to the case of Sec. 4.3.2. When deployment is stopped, the cable keeps on oscillating about a new, shifted equilibrium, as shown in Fig. 4.8(b). We see from Fig. 4.8(b) that, some higher modes appear to be dominating the vibration of the cable after the cable stops lengthening; see energy spectrum (inscribed in Fig. 4.8(b)) of the post-lengthening oscillations. This is due to the sudden change of the deployment rate from $v = 10 \text{ ms}^{-1}$, after the desired elevation is achieved. Such a sudden change in the cable's lengthening excites higher modes that subsequently dominate. The rate of deployment is taken to change sharply at the starting and ending of the deployment. The

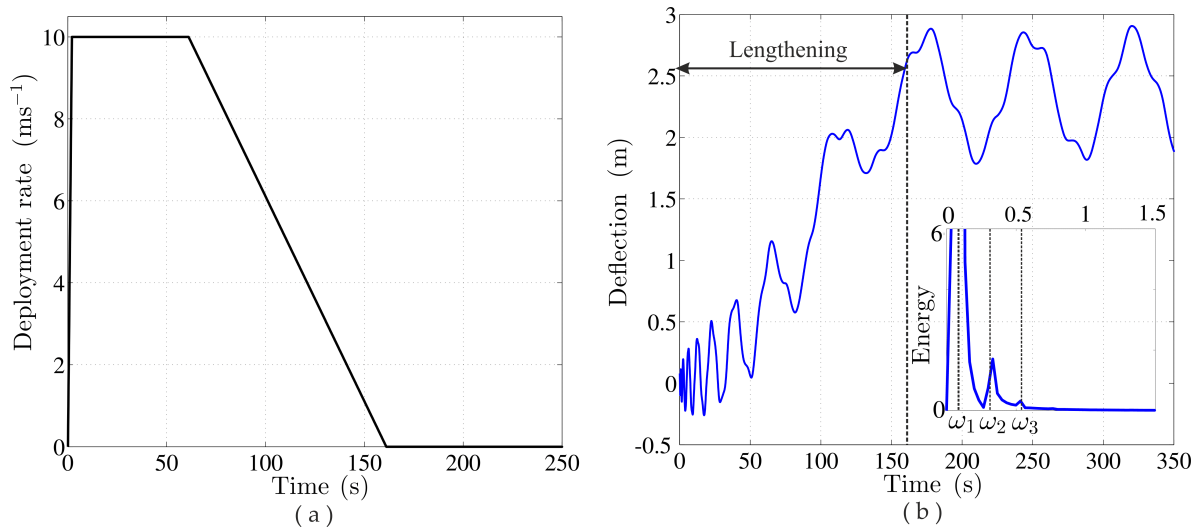


Fig. 4.8: (color online) (a) Time series response for the end-tip displacement, (b) velocity profile. The cable is taken to be lengthening from an initial length of $L_0 = 1m$

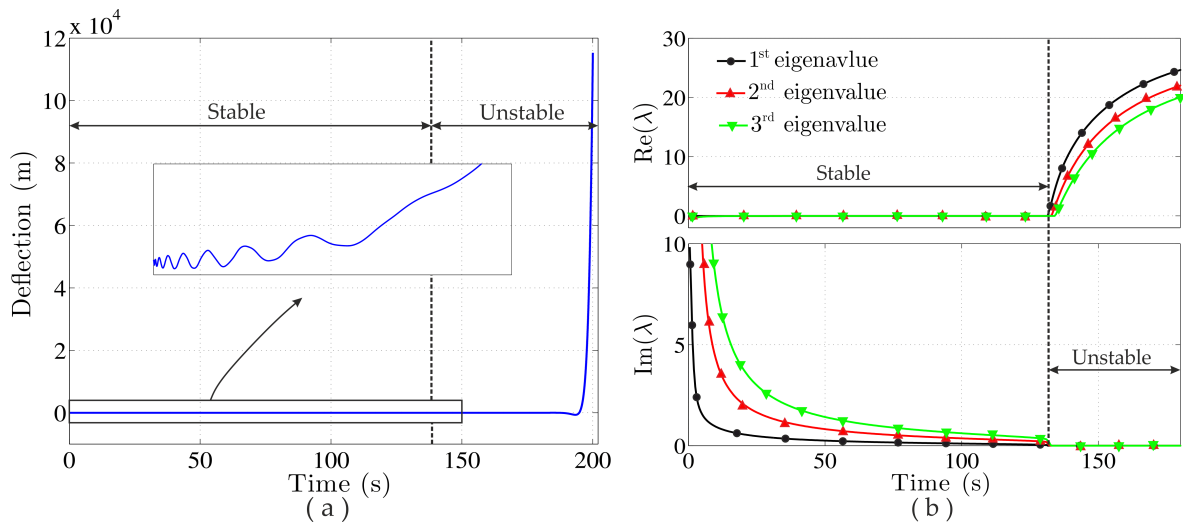


Fig. 4.9: (color online) (a) Time series response for the end displacement, (b) evolution of first three eigenvalues in time. The cable is taken to be lengthening from an initial length of $L_0 = 1m$.

stability of the system is confirmed by its eigenvalues shown in Fig. 4.8(d), in which, the real parts of the eigenvalues always remain negative or zero throughout deployment. We note the high negative real parts of the second and third eigenvalues near $t = 0$ in Fig. 4.8(d) that rapidly go to zero. This indicates fast decay of energies in the second and third eigenmodes, cf. Figs. 3.4(a) and Figs. 3.4(c).

Next, we investigate the dynamics of the system when the deployment rate from that shown in Fig. 4.8(c) to Fig. 4.9(a). The desired elevation is kept constant. We now see in Fig. 4.9(b) that unlike Fig. 4.8(b), higher modes are less dominating; see energy spectrum of post-lengthening oscillations, inscribed in Fig. 4.9(b). Thus, we conclude that higher modes may not get excited if the changes in deployment rates are more gradual.

Finally, we investigate the deployment of the aerostat with the same rate of $v = 10 \text{ ms}^{-1}$, but now upto an elevation of 2 km. We note from Fig. 4.2(b) that deployment upto this elevation may lead to instability. The velocity profile of air is the same as in Fig. 4.8(a). The deployment rate is the same as Fig. 4.8(c), except deploying for a longer period of time. Time series of the oscillations of the aerostat is shown in Fig. 4.10(a). We see that the aerostat oscillates about an equilibrium position — shifted by air flow — upto $t < 140$ s. Subsequently, we note a sudden change in the dynamics of the cable when $t \geq 140$ s, at which time the eigenvalues of the system acquire a positive real part; see Fig. 4.10(b). The amplitude starts growing exponentially. One way to safely deploy the aerostat upto an elevation of 2 km is to increase the buoyancy force as discussed in Sec. 4.2.1.

4.5 Summary

In this chapter, we investigated stability of cables, lengthening/shortening with a constant rate. We obtained stability limits in terms of time duration of deployment, given a constant rate of lengthening. Next, the *inherent* instability of shortening cables are investigated in detail. Then, we taken the effect of air flow into account and obtained frequency domain response of lengthening/shortening cables. Finally, we investigated some cases of non-constant rates of deployment.

Part 2

Chapter 5

Geometrically Exact Modeling of Lengthening/Shortening Cables

5.1 Introduction

Geometrically exact (GE) modeling of beams (cable in our case) is employed to take care of large deflections of flexible structures (Simo and Vu-Quoc, 1986a,b, 1988; Simo, 1985; Simo and Vu-Quoc, 1986c; Cao et al., 2006; Betsch and Steinmann, 2002). In this theory, large deflections in the beam are interpreted as large rotation, followed by deformations. This feature enables geometrically exact beam theory (GEBT) to capture large deflections. We first derive the equations of motion for an axially lengthening/shortening GE cable, having one end guided by a fixed channel and other end free. A Lagrangian approach is employed to derive equations of motion (Vu-Quoc and Li, 1995). In Lagrangian formulation, we consider material points and derive equations of motion for each point of the continua. We first describe the geometry of the cable and identify various kinematic variables. This is followed by derivation of the equations of motion by balancing linear and angular momentums of a representative cable element. Then we incorporate the effect of attached aerostat at the free end and finally, end this chapter by introducing a suitable non-dimensionalization.

5.2 Kinematics

We now formulate the kinematics of the lengthening/shortening GE cable in a Lagrangian framework. We restrict its motion to be in-plane. Thus, a two dimensional description of the geometry is obtained. This was first introduced by Vu-Quoc and Li (1995). The lengthening/shortening cable is taken to be of constant length and the guide is moving; see Fig. 5.1. Our interest lies

entirely in the dynamics of the part of the cable, which remains out of the guide. Thus, we consider the cable inside the guide to be undeformed. Cross section of the cable is considered to be plane, however, they don't remain normal to the neutral axis of the cable; see Fig. 5.1. We express all kinematic variables in terms of a fixed reference configuration $\hat{\mathbf{E}}$; see Fig. 5.1. The coordinate system, attached to the current configuration is denoted by $\hat{\mathbf{t}}$; see Fig. 5.1. These

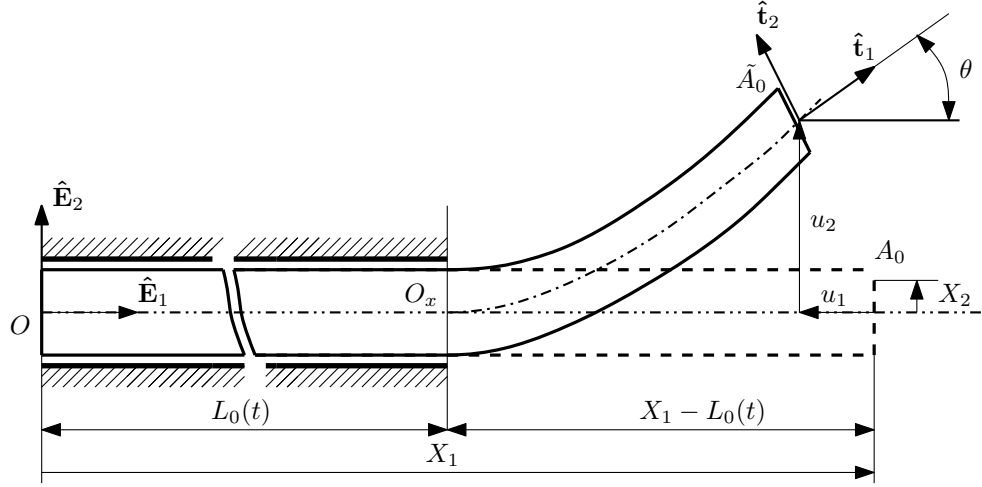


Fig. 5.1: Reference and current configurations of a lengthening/shortening GE cable.

two coordinate frames are mapped onto another by a rotation tensor $\mathbf{\Lambda}(\theta(X_1, t))$ as $\hat{\mathbf{t}} = \mathbf{\Lambda} \cdot \hat{\mathbf{E}}$, where $\theta(X_1, t)$ is the angle of cross section of the cable with its axis; see Fig. 5.1. We express $\mathbf{\Lambda}$ in terms of $\theta(X_1, t)$ as

$$[\mathbf{\Lambda}]_{\hat{\mathbf{E}}} = \begin{bmatrix} \cos \theta & -\sin \theta \\ \sin \theta & \cos \theta \end{bmatrix}.$$

We now express the position of a material point in the deformed configuration with respect to the point O_x , from which the cable comes out from the guide (see Fig. 5.1) as

$$\mathbf{r}(\mathbf{X}, t) = [\{X_1 - L_0(t)\} + u_1(X_1, t)]\hat{\mathbf{E}}_1 + u_2(X_1, t)\hat{\mathbf{E}}_2 + X_2\hat{\mathbf{t}}_2(X_1, t), \quad L_0(t) \leq X_1 \leq L, \quad (5.1)$$

where L is the undeformed length of the cable, $L_0(t)$ is the length of the cable, remaining inside the guide, X_1 and X_2 are the coordinates of a material point in the reference configuration. The position vector of a material point on the deformed neutral axis of the cable is expressed as

$$\mathbf{r}_0(X_1, t) = [\{X_1 - L_0(t)\} + u_1(X_1, t)]\hat{\mathbf{E}}_1 + u_2(X_1, t)\hat{\mathbf{E}}_2, \quad L_0(t) \leq X_1 \leq L. \quad (5.2)$$

Here, all kinematic variables are expressed in terms of a single spatial coordinate X_1 . The number of unknown kinematic parameters are axial displacement u_1 , transverse displacement u_2 and the rotation θ of any cross section. We now proceed to derive the equations of motion by employing fundamental balance laws of mechanics.

5.3 Equations of motion

We derive the equations of motion of lengthening/shortening GE cables by balancing linear and angular momentums of a representative element Ω_0 , which is represented by Ω_t in the deformed configuration; see Fig. 5.2. We now balance linear and angular momentums of Ω_t :

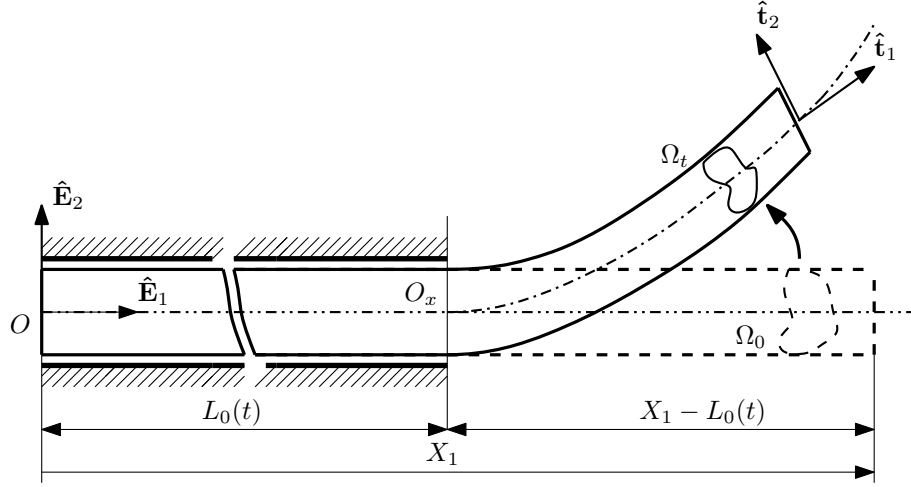


Fig. 5.2: Material domains in reference and current configurations of a sliding geometrically exact beam.

$$\frac{d}{dt} \int_{\Omega_t} \rho \mathbf{v} d\Omega_t = \int_{\partial\Omega_t} \boldsymbol{\sigma} \cdot \hat{\mathbf{n}} d(\partial\Omega_t) + \int_{\Omega_t} \rho \mathbf{b} d\Omega_t, \quad (5.3)$$

and

$$\frac{d}{dt} \int_{\Omega_t} \mathbf{r} \times \rho \mathbf{v} d\Omega_t = \int_{\partial\Omega_t} \mathbf{r} \times \boldsymbol{\sigma} \cdot \hat{\mathbf{n}} d(\partial\Omega_t) + \int_{\Omega_t} \mathbf{r} \times \rho \mathbf{b} d\Omega_t, \quad (5.4)$$

respectively, where ρ is the density of the current configuration Ω_t , $\mathbf{v} = \dot{\mathbf{r}}$ is the velocity of the material points, $\boldsymbol{\sigma}$ is the Cauchy stress tensor, $\hat{\mathbf{n}}$ is normal on the boundary of the domain Ω_t and \mathbf{b} is the body force per unit volume. All these quantities are expressed in current configuration Ω_t in terms of spatial variable \mathbf{x} . The domain Ω_t can be mapped onto the reference configuration Ω_0 through a deformation map ξ , such that $\mathbf{x} = \xi(\mathbf{X}, t)$. This allows us to rewrite the balance laws in the reference configuration as

$$\frac{d}{dt} \int_{\Omega_0} \rho_0 \mathbf{V} d\Omega_0 = \int_{\partial\Omega_0} \mathbf{P} \cdot \hat{\mathbf{N}} d(\partial\Omega_0) + \int_{\Omega_0} \rho_0 \mathbf{B} d\Omega_0, \quad (5.5)$$

and

$$\frac{d}{dt} \int_{\Omega_0} \mathbf{r} \times \rho_0 \mathbf{V} d\Omega_0 = \int_{\partial\Omega_0} \mathbf{r} \times \mathbf{P} \cdot \hat{\mathbf{N}} d(\partial\Omega_0) + \int_{\Omega_0} \mathbf{r} \times \rho_0 \mathbf{B} d\Omega_0, \quad (5.6)$$

where $\rho_0(\mathbf{X}) = \rho(\mathbf{x}, t)J(\mathbf{X}, t)$ the density in the reference configuration, $J(\mathbf{X}, t)$ is the Jacobian determinant corresponding to the deformation map $\xi(\mathbf{X}, t)$, $\mathbf{V}(\mathbf{X}, t) = \mathbf{v}(\mathbf{x}, t)$ is the material velocity $\mathbf{B}(\mathbf{X}, t) = \mathbf{b}(\mathbf{x}, t)$ is the body force, $\mathbf{P}(\mathbf{X}, t)$ is the first Piola-Kirchhoff stress tensor and $\hat{\mathbf{N}} = N_i \hat{\mathbf{E}}_i$ is the unit normal on the boundary $\partial\Omega_0$. We define \mathbf{S} as the traction force

perpendicular to the face normal to $\hat{\mathbf{E}}_i$ as $\mathbf{S} = \mathbf{P} \cdot \hat{\mathbf{E}}_i$. We now express \mathbf{P} as

$$\mathbf{P}(\mathbf{X}, t) = \mathbf{S}_1(\mathbf{X}, t) \otimes \hat{\mathbf{E}}_1 + \mathbf{S}_2(\mathbf{X}, t) \otimes \hat{\mathbf{E}}_2 + \mathbf{S}_3(\mathbf{X}, t) \otimes \hat{\mathbf{E}}_3, \quad (5.7)$$

where \otimes is tensor product of two vectors. We now use divergence theorem and the fact that domain Ω_0 is independent of time to modify the balance laws:

$$\int_{\Omega_0} \rho_0 \ddot{\mathbf{r}} d\Omega_0 = \int_{\Omega_0} \nabla_{X_1} \cdot \mathbf{P} d\Omega_0 + \int_{\Omega_0} \rho_0 \mathbf{B} d\Omega_0 \quad (5.8)$$

and

$$\int_{\Omega_0} \mathbf{r} \times \rho_0 \ddot{\mathbf{r}} d\Omega_0 = \int_{\Omega_0} [\mathbf{r} \times \mathbf{S}_i]_{,i} d\Omega_0 + \int_{\Omega_0} \mathbf{r} \times \rho_0 \mathbf{B} d\Omega_0. \quad (5.9)$$

We now consider the element Ω_0 to be a small section of the cable, having width ΔX_1 and cross section \bar{A} . With this assumption (5.8) may be written as

$$\int_{\Delta X_1} \int_{\bar{A}} \rho_0 \ddot{\mathbf{r}} d\bar{A} dX_1 = \int_{\Delta X_1} \int_{\bar{A}} \nabla_{X_1} \cdot \mathbf{P} d\bar{A} dX_1 + \int_{\Delta X_1} \int_{\bar{A}} \rho_0 \mathbf{B} d\bar{A} dX_1. \quad (5.10)$$

We now employ (5.1) and (5.2) to express $\ddot{\mathbf{r}}(\mathbf{X}, t)$ as

$$\ddot{\mathbf{r}}(\mathbf{X}, t) = \ddot{\mathbf{r}}_0(X_1, t) + X_2 \ddot{\mathbf{t}}_2(X_1, t).$$

We assume symmetry in the cable section to obtain

$$\int_{\bar{A}} \rho_0 X_2 d\bar{A} = 0.$$

Let consider A_ρ be the mass per unit length of the cable in the reference configuration:

$$A_\rho = \int_{\bar{A}} \rho_0 d\bar{A}.$$

Employing the above three equations, the inner integral in the inertia term in (5.10) becomes

$$\int_{\bar{A}} \rho_0 \ddot{\mathbf{r}} d\bar{A} = A_\rho \ddot{\mathbf{r}}_0(X_1, t). \quad (5.11)$$

We now express the inner integral in the first term of the right hand side of (5.10) as

$$\int_{\bar{A}} \nabla_{X_1} \cdot \mathbf{P} d\bar{A} = \int_{\bar{A}} \left[\frac{\partial \mathbf{S}_1}{\partial X_1} + \frac{\partial \mathbf{S}_2}{\partial X_2} + \frac{\partial \mathbf{S}_3}{\partial X_3} \right] d\bar{A}, \quad (5.12)$$

where we have utilized (5.7). Only the traction vector on the $\hat{\mathbf{E}}_1$ plane is a result of internal stresses. Other surfaces of the cable element Ω_0 are either free or subjected to external loading.

Thus, we express (5.12) as

$$\int_{\bar{A}} \nabla_{X_1} \cdot \mathbf{P} d\bar{A} = \frac{\partial}{\partial X_1} \mathbf{f}(X_1, t) + \mathbf{f}_e(X_1, t), \quad (5.13)$$

where $\mathbf{f}_e(X_1, t)$ is the resultant of external forces per unit length, defined as

$$\mathbf{f}_e(X_1, t) = \int_{\bar{A}} \left[\frac{\partial \mathbf{S}_2}{\partial X_2} + \frac{\partial \mathbf{S}_3}{\partial X_3} \right] d\bar{A}$$

and $\mathbf{f}(X_1, t)$ is the force resultant on the cross section, defined as

$$\mathbf{f}(X_1, t) = \int_{\bar{A}} \mathbf{S}_1 d\bar{A}.$$

From (5.11) and (5.13) we may now express (5.10) as

$$\int_{\Delta X_1} A_\rho \ddot{\mathbf{r}}_0(X_1, t) dX_1 = \int_{\Delta X_1} \left[\frac{\partial}{\partial X_1} \mathbf{f}(X_1, t) + \mathbf{f}_e(X_1, t) \right] dX_1 + \int_{\Delta X_1} \mathbf{f}_b(X_1, t) dX_1, \quad L_0(t) \leq X_1 \leq L, \quad (5.14)$$

where $\mathbf{f}_b(X_1, t)$ is the body force per unit reference length, defined as

$$\mathbf{f}_b(X_1, t) = \int_{\bar{A}} \rho_0 \mathbf{B} d\bar{A}.$$

We now combine two external forces $\mathbf{f}_e(X_1, t)$ and $\mathbf{f}_b(X_1, t)$ as $\mathbf{F}(X_1, t)$, which is the resultant of all external forces per unit length. Now, because ΔX_1 is arbitrary, (5.14) can only hold if

$$A_\rho \ddot{\mathbf{r}}_0 - \frac{\partial \mathbf{f}}{\partial X_1} - \mathbf{F} = 0, \quad L_0(t) \leq X_1 \leq L. \quad (5.15)$$

We are restricting the cable's motion in two dimensions. Thus, the above equation represents balance of linear momentum in $\hat{\mathbf{E}}_1$ and $\hat{\mathbf{E}}_2$ directions. We now consider (5.9) to derive the third governing equation. We define the (internal) stress couple \mathbf{m} on any cross-section as

$$\mathbf{m}(X_1, t) = \int_{\bar{A}} (\mathbf{r} - \mathbf{r}_0) \times \mathbf{S}_1 d\bar{A}. \quad (5.16)$$

Equation (5.9) may be expressed in a familiar form as follows. As in the case of (5.10), we first rewrite (5.9) as

$$\int_{\Delta X_1} \int_{\bar{A}} \mathbf{r} \times \rho_0 \ddot{\mathbf{r}} d\bar{A} dX_1 = \int_{\Delta X_1} \int_{\bar{A}} [\mathbf{r} \times \mathbf{S}_i]_i d\bar{A} dX_1 + \int_{\Delta X_1} \int_{\bar{A}} \mathbf{r} \times \rho_0 \mathbf{B} d\bar{A} dX_1.$$

Adding and subtracting \mathbf{r}_0 in the integrals on the right-hand side yields

$$\begin{aligned} \int_{\Delta X_1} \int_{\bar{A}} \mathbf{r} \times \rho_0 \ddot{\mathbf{r}} d\bar{A} dX_1 &= \int_{\Delta X_1} \int_{\bar{A}} \left\{ [(\mathbf{r} - \mathbf{r}_0) \times \mathbf{S}_i]_{,i} + \frac{\partial \mathbf{r}_0}{\partial X_i} \times \mathbf{S}_i + \mathbf{r}_0 \times \frac{\partial \mathbf{S}_i}{\partial X_i} \right\} d\bar{A} dX_1 \\ &+ \int_{\Delta X_1} \int_{\bar{A}} \left\{ (\mathbf{r} - \mathbf{r}_0) \times \rho_0 \mathbf{B} + \mathbf{r}_0 \times \rho_0 \mathbf{B} \right\} d\bar{A} dX_1. \end{aligned}$$

Redistributing terms:

$$\begin{aligned} \int_{\Delta X_1} \int_{\bar{A}} \mathbf{r} \times \rho_0 \ddot{\mathbf{r}} d\bar{A} dX_1 &= \int_{\Delta X_1} \int_{\bar{A}} \left\{ [(\mathbf{r} - \mathbf{r}_0) \times \mathbf{S}_i]_{,i} + \frac{\partial \mathbf{r}_0}{\partial X_i} \times \mathbf{S}_i \right\} d\bar{A} dX_1 \\ &+ \int_{\Delta X_1} \int_{\bar{A}} \left\{ (\mathbf{r} - \mathbf{r}_0) \times \rho_0 \mathbf{B} \right\} d\bar{A} dX_1 + \int_{\Delta X_1} \int_{\bar{A}} \left\{ \mathbf{r}_0 \times \left(\frac{\partial \mathbf{S}_i}{\partial X_i} + \rho_0 \mathbf{B} \right) \right\} d\bar{A} dX_1. \end{aligned} \quad (5.17)$$

Employing definitions of $\mathbf{r}_0(X_1, t)$, $\mathbf{f}(X_1, t)$ and $\mathbf{m}(X_1, t)$ and equations (5.10) and (5.12) we express the above as

$$\begin{aligned} \int_{\Delta X_1} \int_{\bar{A}} \mathbf{r} \times \rho_0 \ddot{\mathbf{r}} d\bar{A} dX_1 &= \int_{\Delta X_1} \left\{ \frac{\partial}{\partial X_1} \mathbf{m}(X_1, t) + \frac{\partial \mathbf{r}_0}{\partial X_1} \times \mathbf{f}(X_1, t) + \mathbf{M}(X_1, t) \right\} dX_1 \\ &+ \int_{\Delta X_1} \int_{\bar{A}} \mathbf{r}_0 \times \rho_0 \ddot{\mathbf{r}}_0 d\bar{A} dX_1 \end{aligned} \quad (5.18)$$

where

$$\mathbf{M} = \int_{\bar{A}} \left\{ \sum_{\alpha=2}^3 [(\mathbf{r} - \mathbf{r}_0) \times \mathbf{S}_\alpha]_{,\alpha} + (\mathbf{r} - \mathbf{r}_0) \times \rho_0 \mathbf{B} \right\} d\bar{A}$$

is the external moment per unit length of the beam. Rearranging (5.18) we obtain:

$$\begin{aligned} \int_{\Delta X_1} \int_{\bar{A}} \rho_0 (\mathbf{r} \times \ddot{\mathbf{r}} - \mathbf{r}_0 \times \ddot{\mathbf{r}}_0) d\bar{A} dX_1 &= \int_{\Delta X_1} \left\{ \frac{\partial}{\partial X_1} \mathbf{m}(X_1, t) \right. \\ &\left. + \frac{\partial \mathbf{r}_0}{\partial X_1} \times \mathbf{f}(X_1, t) + \mathbf{M}(X_1, t) \right\} dX_1, \end{aligned} \quad (5.19)$$

Employing (5.1) and (5.2) the inertia term on the left hand side of (5.19) may be expressed as

$$\begin{aligned} \int_{\Delta X_1} \int_{\bar{A}} \rho_0 (\mathbf{r} \times \ddot{\mathbf{r}} - \mathbf{r}_0 \times \ddot{\mathbf{r}}_0) d\bar{A} dX_1 &= \int_{\Delta X_1} \int_{\bar{A}} \rho_0 [(\mathbf{r}_0 + X_2 \hat{\mathbf{t}}_2) \times (\ddot{\mathbf{r}}_0 + X_2 \ddot{\hat{\mathbf{t}}}_2) - \mathbf{r}_0 \times \ddot{\mathbf{r}}_0] d\bar{A} dX_1 \\ &= \int_{\Delta X_1} \int_{\bar{A}} \rho_0 [X_2 (\mathbf{r}_0 \times \ddot{\hat{\mathbf{t}}}_2 + \hat{\mathbf{t}}_2 \times \ddot{\mathbf{r}}_0) + X_2^2 (\hat{\mathbf{t}}_2 \times \ddot{\hat{\mathbf{t}}}_2)] d\bar{A} dX_1 \\ &= \int_{\Delta X_1} I_\rho (\hat{\mathbf{t}}_2 \times \ddot{\hat{\mathbf{t}}}_2) dX_1, \end{aligned}$$

where I_ρ is the mass moment of inertia of a cross section:

$$I_\rho = \int_{\bar{A}} \rho_0 X_2^2 d\bar{A}.$$

We now compute $\ddot{\mathbf{t}}_2$ in two dimensions as follows

$$\hat{\mathbf{t}}_2 = \cos \theta \hat{\mathbf{E}}_2 - \sin \theta \hat{\mathbf{E}}_1,$$

so that

$$\dot{\hat{\mathbf{t}}}_2 = -\dot{\theta} \sin \theta \hat{\mathbf{E}}_2 - \dot{\theta} \cos \theta \hat{\mathbf{E}}_1,$$

and

$$\ddot{\hat{\mathbf{t}}}_2 = -\ddot{\theta} \sin \theta \hat{\mathbf{E}}_2 - \ddot{\theta} \cos \theta \hat{\mathbf{E}}_1 - \dot{\theta}^2 \cos \theta \hat{\mathbf{E}}_2 + \dot{\theta}^2 \sin \theta \hat{\mathbf{E}}_1 = -\ddot{\theta} \hat{\mathbf{t}}_1 - \dot{\theta}^2 \hat{\mathbf{t}}_2.$$

Thus,

$$\hat{\mathbf{t}}_2 \times \ddot{\hat{\mathbf{t}}}_2 = \hat{\mathbf{t}}_2 \times (-\ddot{\theta} \hat{\mathbf{t}}_1 - \dot{\theta}^2 \hat{\mathbf{t}}_2) = \ddot{\theta} \hat{\mathbf{t}}_3 = \ddot{\theta} \hat{\mathbf{E}}_3.$$

Since we are considering a two-dimensional problem, the stress couple \mathbf{m} and the externally applied couple \mathbf{M} always remain along $\hat{\mathbf{E}}_3$. Thus, we may write $\mathbf{m} = m \hat{\mathbf{E}}_3$ and $\mathbf{M} = M \hat{\mathbf{E}}_3$. Taking the projection along $\hat{\mathbf{E}}_3$ of (5.19), the angular momentum balance is now reduced to a scalar equation:

$$\int_{\Delta X_1} I_\rho \ddot{\theta} dX_1 = \int_{\Delta X_1} \left[\frac{\partial}{\partial X_1} m(X_1, t) + \left\{ \frac{\partial}{\partial X_1} \mathbf{r}_0(X_1, t) \times \mathbf{f}(X_1, t) \right\} \cdot \hat{\mathbf{E}}_3 + M(X_1, t) \right] dX_1,$$

where $L_0(t) \leq X_1 \leq L$. As before, because ΔX_1 the above will hold only if

$$I_\rho \ddot{\theta} = \frac{\partial m}{\partial X_1} + \left\{ \frac{\partial \mathbf{r}_0}{\partial X_1} \times \mathbf{f} \right\} \cdot \hat{\mathbf{E}}_3 + M, \quad L_0(t) \leq X_1 \leq L. \quad (5.20)$$

From (5.15) and (5.20) we now write the three simultaneous partial differential equations, that govern the dynamics of GE cables in terms of X_1 and t as follows

$$\begin{aligned} A_\rho [\ddot{\mathbf{r}}_0]_1 &= \frac{\partial f_1}{\partial X_1} + F_1, \\ A_\rho [\ddot{\mathbf{r}}_0]_2 &= \frac{\partial f_2}{\partial X_1} + F_2, \\ I_\rho \ddot{\theta} &= \frac{\partial m}{\partial X_1} + \left\{ \frac{\partial \mathbf{r}_0}{\partial X_1} \times \mathbf{f} \right\} \cdot \hat{\mathbf{E}}_3 + M \end{aligned} \quad (5.21)$$

with $L_0(t) \leq X_1 \leq L$. At $X_1 = L_0(t)$ we have kinematic boundary condition:

$$u_1(X_1, t) = 0, \quad u_2(X_1, t) = 0, \quad \text{and} \quad \theta(X_1, t) = 0. \quad (5.22)$$

At the free end of the cable, the resultant force on the cross section is zero. Thus, at $X_1 = L$ boundary conditions are:

$$f_1(X_1, t) = 0, \quad f_2(X_1, t) = 0, \quad \text{and} \quad m(X_1, t) = 0. \quad (5.23)$$

In (5.23) we ignored the aerostat, whose presence will change the force boundary conditions at $X_1 = L$. Modeling of the aerostat and modification of the force boundary conditions are discussed later in this chapter. We also have to express the internal force \mathbf{f} and moment m in terms of kinematic variables. This is done by defining suitable strain measures and considering the continuum to be linear elastic.

5.4 Strain measures

Geometrically exact beam theory (GEBT) admits finite rotation followed by a small deformation. This assumption will simplify the relation between displacements and internal forces. We consider a hypothetical intermediate configuration of the beam, called the *shadow beam*; see Fig. 5.3. This shadow beam is the configuration, that undergoes rigid body rotation from the

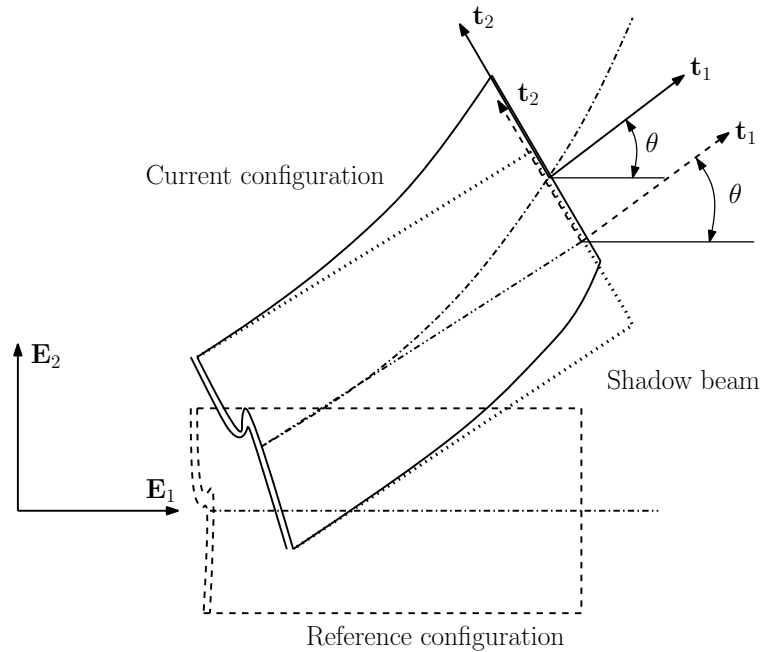


Fig. 5.3: Small strain superimposed upon a large rotation. Reference and current configurations along with the shadow beam are shown.

reference configuration. Elastic deformation from the shadow beam configuration takes place

after it. We now express deformation per unit length as

$$\mathbf{\Gamma} = \mathbf{\Phi}_{0,X_1} - \mathbf{t}_1,$$

or,

$$\mathbf{\Gamma} = (1 + u_{1,X_1} - \cos \theta)\mathbf{E}_1 + (u_{2,X_1} - \sin \theta)\mathbf{E}_2, \quad (5.24)$$

where, $\mathbf{\Gamma}$ is defined as the difference between the slope of the neutral axis and unit normal on any cable section. This strain field $\mathbf{\Gamma}$ was introduced by [Simo and Vu-Quoc \(1986a\)](#), inspired by the fundamental papers on rod theory by [Antman \(1973\)](#); [Reissner \(1973\)](#). It is shown in [Simo and Vu-Quoc \(1986a\)](#) that this strain measure $\mathbf{\Gamma}$ remains invariant under superposed rotations. This property of $\mathbf{\Gamma}$ plays a pivotal role in success of GEBT. Because the deformation is taking place from the shadow beam configuration to the current configuration, we map $\mathbf{\Gamma}$ onto the shadow beam configuration to obtain

$$\boldsymbol{\gamma} = \boldsymbol{\Lambda}^T \cdot \mathbf{\Gamma}. \quad (5.25)$$

We now assume the beam to be a linear elastic continuum. Thus, we express axial and shear stresses in a cable section in the current configuration as

$$\mathbf{n} = \mathbf{C} \cdot \boldsymbol{\gamma} = \mathbf{C} \cdot \boldsymbol{\Lambda}^T \cdot \mathbf{\Gamma}, \quad (5.26)$$

where

$$[\mathbf{C}]_{\mathbf{E}} = \begin{bmatrix} EA & 0 \\ 0 & GA_s \end{bmatrix}.$$

We now express (5.26) in matrix notation in the following form:

$$\{\mathbf{n}\} = [\mathbf{C}][\boldsymbol{\Lambda}]^T \{\mathbf{\Gamma}\},$$

where $[\cdot]$ denotes tensors, expressed in reference frame \mathbf{E} and $\{\cdot\}$ denotes vectors, expressed in \mathbf{E} . We now express the stress resultant \mathbf{n} in the reference configuration as

$$\{\mathbf{f}\} = [\boldsymbol{\Lambda}][\mathbf{C}][\boldsymbol{\Lambda}]^T \{\mathbf{\Gamma}\}.$$

We will use this expression for \mathbf{f} in (5.21) in our computations. Expression for bending stress m is now obtained as

$$m = EI\theta_{,X_1}.$$

Because m is in the \mathbf{E}_3 direction, which coincides with \mathbf{t}_3 in a two-dimensional system, a mapping from the current to the reference configuration is not needed. Substituting \mathbf{f} and m in (5.21), we obtain a complete boundary value problem, having three unknowns u_1 , u_2 and θ .

We note that our domain of interest is changing with time as $L_0(t) \leq X_1 \leq L$. This time-varying

domain may invite additional complexity in computations. This is circumvented by introducing a suitable mapping of X_1 to an equivalent integration domain that remains constant in time.

5.5 Mapped coordinate system

It is customary to map the changing domain onto an equivalent fixed domain (Vu-Quoc and Li, 1995; Roy and Chatterjee, 2009). Let $\zeta(t)$ be the image of a material point corresponding to X_1 defined at time t by

$$\zeta(t) = 1 + \frac{X_1 - L}{L_1(t)}, \quad (5.27)$$

so that $0 \leq \zeta(t) \leq 1$, where $L_1(t) = L - L_0(t)$ is the length of the cable. We identify variables with argument ζ by $(\tilde{\cdot})$. Thus, kinematic variables become $\tilde{u}_1(\zeta, t) = u_1(X_1, t)$, $\tilde{u}_2(\zeta, t) = u_2(X_1, t)$ and $\tilde{\theta}(\zeta, t) = \theta(X_1, t)$. The first equation of (5.21) is then modified to

$$A_\rho \left[\frac{\partial^2 \tilde{u}_1}{\partial \zeta^2} \left(\frac{\partial \zeta}{\partial t} \right)^2 + 2 \frac{\partial^2 \tilde{u}_1}{\partial \zeta \partial t} \frac{\partial \zeta}{\partial t} + \frac{\partial \tilde{u}_1}{\partial \zeta} \frac{\partial^2 \zeta}{\partial t^2} + \frac{\partial^2 \tilde{u}_1}{\partial t^2} + \ddot{L}_1 \right] = \frac{\partial \tilde{f}_1}{\partial \zeta} \frac{\partial \zeta}{\partial X_1} + \tilde{F}_1, \quad (5.28)$$

where we have employed the chain rule

$$\frac{\partial^2 u_1}{\partial t^2} = \frac{\partial^2 \tilde{u}_1}{\partial \zeta^2} \left(\frac{\partial \zeta}{\partial t} \right)^2 + 2 \frac{\partial^2 \tilde{u}_1}{\partial \zeta \partial t} \frac{\partial \zeta}{\partial t} + \frac{\partial \tilde{u}_1}{\partial \zeta} \frac{\partial^2 \zeta}{\partial t^2} + \frac{\partial^2 \tilde{u}_1}{\partial t^2}.$$

Evaluating temporal derivatives of ζ from (5.27) as

$$\frac{\partial \zeta}{\partial t} = (1 - \zeta) \frac{\dot{L}_1}{L_1},$$

and

$$\frac{\partial^2 \zeta}{\partial t^2} = \frac{(1 - \zeta) \ddot{L}_1}{L_1} - 2 \frac{(1 - \zeta) \dot{L}_1^2}{L_1^2}$$

and substituting them to (5.28) yields

$$\begin{aligned} A_\rho \left[\frac{\partial^2 \tilde{u}_1}{\partial \zeta^2} \frac{(1 - \zeta)^2 \dot{L}_1^2}{L_1^2} + 2 \frac{\partial^2 \tilde{u}_1}{\partial \zeta \partial t} \frac{(1 - \zeta) \dot{L}_1}{L_1} + \frac{\partial \tilde{u}_1}{\partial \zeta} \left\{ \frac{(1 - \zeta) \ddot{L}_1}{L_1} - 2 \frac{(1 - \zeta) \dot{L}_1^2}{L_1^2} \right\} + \frac{\partial^2 \tilde{u}_1}{\partial t^2} + \ddot{L}_1 \right] \\ = \frac{\partial \tilde{f}_1}{\partial \zeta} \frac{1}{L_1} + \tilde{F}_1. \end{aligned}$$

Rearranging the above we obtain:

$$A_\rho \left[\frac{\partial}{\partial \zeta} \left\{ \frac{(1 - \zeta)^2 \dot{L}_1^2}{L_1^2} \frac{\partial \tilde{u}_1}{\partial \zeta} \right\} + 2 \frac{\partial^2 \tilde{u}_1}{\partial \zeta \partial t} \frac{(1 - \zeta) \dot{L}_1}{L_1} + \frac{\partial \tilde{u}_1}{\partial \zeta} \frac{(1 - \zeta) \ddot{L}_1}{L_1} + \frac{\partial^2 \tilde{u}_1}{\partial t^2} + \ddot{L}_1 \right] = \frac{\partial \tilde{f}_1}{\partial \zeta} \frac{1}{L_1} + \tilde{F}_1.$$

The above equation is finally expressed as

$$A_\rho \left[\frac{\partial}{\partial \zeta} \left\{ (1 - \zeta)^2 \dot{L}_1^2 \frac{\partial \tilde{u}_1}{\partial \zeta} \right\} + 2 \frac{\partial^2 \tilde{u}_1}{\partial \zeta \partial t} (1 - \zeta) \dot{L}_1 L_1 + \frac{\partial \tilde{u}_1}{\partial \zeta} (1 - \zeta) \ddot{L}_1 L_1 + \frac{\partial^2 \tilde{u}_1}{\partial t^2} L_1^2 + \ddot{L}_1 L_1^2 \right] \\ = \frac{\partial \tilde{f}_1}{\partial \zeta} L_1 + \tilde{F}_1 L_1^2.$$

Which is over a constant spatial domain. We now repeat this process for the remaining two equations in (5.21). The equations of motion in terms of the fixed coordinate ζ are

$$A_\rho \left[\frac{\partial}{\partial \zeta} \left\{ (1 - \zeta)^2 \dot{L}_1^2 \frac{\partial \tilde{u}_1}{\partial \zeta} \right\} + 2 \frac{\partial^2 \tilde{u}_1}{\partial \zeta \partial t} (1 - \zeta) \dot{L}_1 L_1 + \frac{\partial \tilde{u}_1}{\partial \zeta} (1 - \zeta) \ddot{L}_1 L_1 \right. \\ \left. + \frac{\partial^2 \tilde{u}_1}{\partial t^2} L_1^2 + \ddot{L}_1 L_1^2 \right] = \frac{\partial \tilde{f}_1}{\partial \zeta} L_1 + \tilde{F}_1 L_1^2, \\ A_\rho \left[\frac{\partial}{\partial \zeta} \left\{ (1 - \zeta)^2 \dot{L}_1^2 \frac{\partial \tilde{u}_2}{\partial \zeta} \right\} + 2 \frac{\partial^2 \tilde{u}_2}{\partial \zeta \partial t} (1 - \zeta) \dot{L}_1 L_1 + \frac{\partial \tilde{u}_2}{\partial \zeta} (1 - \zeta) \ddot{L}_1 L_1 \right. \\ \left. + \frac{\partial^2 \tilde{u}_2}{\partial t^2} L_1^2 \right] = \frac{\partial \tilde{f}_2}{\partial \zeta} L_1 + \tilde{F}_2 L_1^2 \quad (5.29)$$

and

$$I_\rho \left[\frac{\partial}{\partial \zeta} \left\{ (1 - \zeta)^2 \dot{L}_1^2 \frac{\partial \tilde{\theta}}{\partial \zeta} \right\} + 2 \frac{\partial^2 \tilde{\theta}}{\partial \zeta \partial t} (1 - \zeta) \dot{L}_1 L_1 + \frac{\partial \tilde{\theta}}{\partial \zeta} (1 - \zeta) \ddot{L}_1 L_1 \right. \\ \left. + \frac{\partial^2 \tilde{\theta}}{\partial t^2} L_1^2 \right] = \frac{\partial \tilde{m}}{\partial \zeta} L_1 + L_1 \left\{ \frac{\partial \tilde{\mathbf{r}}_0}{\partial \zeta} \times \tilde{\mathbf{f}} \right\} \cdot \mathbf{E}_3 + \tilde{M} L_1^2.$$

The above equations are more convenient for computation, as the spatial domain remains fixed. The boundary conditions at $X_1 = L_0(t)$ are now modified as

$$\tilde{u}_1(\zeta, t) = 0, \quad \tilde{u}_2(\zeta, t) = 0 \quad \text{and} \quad \tilde{\theta}(\zeta, t) = 0, \quad \text{at} \quad \zeta = 0, \quad (5.30)$$

while the force boundary conditions at $X_1 = L$ are now expressed in terms of ζ as

$$\tilde{f}_1(\zeta, t) = 0, \quad \tilde{f}_2(\zeta, t) = 0, \quad \text{and} \quad \tilde{m}(\zeta, t) = 0 \quad \text{at} \quad \zeta = 1. \quad (5.31)$$

A full finite element scheme for computation is adopted to solve (5.29) along with the boundary conditions (5.30) and (5.31). The computation procedure will be discussed in the next chapter. Prior to going to the computations, it is customary to non-dimensionalize (5.29) along with (5.30) and (5.31). The non-dimensionalization scheme is discussed in the next section.

5.6 Non-dimensionalization

We now non-dimensionalise (5.29) and express it as

$$\begin{aligned} & \tilde{\gamma} \left[\frac{\partial}{\partial \zeta} \left\{ (1 - \zeta)^2 \frac{\partial \tilde{u}_1^*}{\partial \zeta} \right\} i^2 + 2 \frac{\partial^2 \tilde{u}_1^*}{\partial \zeta \partial \bar{t}} (1 - \zeta) \dot{l} + \frac{\partial \tilde{u}_1^*}{\partial \zeta} (1 - \zeta) \ddot{l} + \frac{\partial^2 \tilde{u}_1^*}{\partial \bar{t}^2} l^2 + \ddot{l}^2 \right] \\ & \quad = \frac{\partial \tilde{f}_1^*}{\partial \zeta} l + \tilde{F}_1^* l^2, \\ & \tilde{\gamma} \left[\frac{\partial}{\partial \zeta} \left\{ (1 - \zeta)^2 \frac{\partial \tilde{u}_2^*}{\partial \zeta} \right\} i^2 + 2 \frac{\partial^2 \tilde{u}_2^*}{\partial \zeta \partial \bar{t}} (1 - \zeta) \dot{l} + \frac{\partial \tilde{u}_2^*}{\partial \zeta} (1 - \zeta) \ddot{l} + \frac{\partial^2 \tilde{u}_2^*}{\partial \bar{t}^2} l^2 \right] = \frac{\partial \tilde{f}_2^*}{\partial \zeta} l + \tilde{F}_2^* l^2, \quad (5.32) \\ \text{and} \quad & \frac{\partial}{\partial \zeta} \left\{ (1 - \zeta)^2 \frac{\partial \tilde{\theta}^*}{\partial \zeta} \right\} i^2 + 2 \frac{\partial^2 \tilde{\theta}^*}{\partial \zeta \partial \bar{t}} (1 - \zeta) \dot{l} + \frac{\partial \tilde{\theta}^*}{\partial \zeta} (1 - \zeta) \ddot{l} + \frac{\partial^2 \tilde{\theta}^*}{\partial \bar{t}^2} l^2 = \frac{\partial \tilde{m}^*}{\partial \zeta} l \\ & \quad + l \left\{ \frac{\partial \tilde{\mathbf{r}}_0^*}{\partial \zeta} \times \tilde{\mathbf{f}}^* \right\} \cdot \mathbf{E}_3 + \tilde{M}^* l^2, \end{aligned}$$

where $l = L_1/L_0(t_0)$ is the non-dimensional length of the cable of initial length $L_0(t_0)$, \tilde{u}_1^* , \tilde{u}_2^* and $\tilde{\theta}^*$ are the non-dimensional displacements and rotation of any beam section, respectively, defined as $\tilde{u}_1^* = \tilde{u}_1/L_0$, $\tilde{u}_2^* = \tilde{u}_2/L_0$, $\tilde{\theta}^* = \tilde{\theta}$, and \bar{t} is the non-dimensional time:

$$\bar{t} = t \frac{1}{L_0} \sqrt{\frac{EI}{I_\rho}}.$$

Henceforth, $(\dot{\cdot})$ denotes differentiation with respect to \bar{t} . Non-dimensional velocity

$$\tilde{v} = \dot{l} = \dot{L}_1 \sqrt{\frac{I_\rho}{EI}},$$

and, $\tilde{\gamma} = A_\rho L_0 / I_\rho$ is the non-dimensional ratio of the mass per unit length and the sectional mass moment of inertia of the beam per unit length. The non-dimensional internal force vector $\tilde{\mathbf{f}}^*$

$$\{\tilde{\mathbf{f}}^*\} = [\mathbf{\Lambda}]^T [\mathbf{C}^*] [\mathbf{\Lambda}] \{\tilde{\mathbf{\Gamma}}\},$$

where

$$[\mathbf{C}^*] = \begin{bmatrix} \frac{EA}{EI} L_0^2 & 0 \\ 0 & \frac{GA_s}{EI} L_0^2 \end{bmatrix} = \begin{bmatrix} E^* & 0 \\ 0 & E^* \end{bmatrix},$$

with E^* being the ratio of axial to bending stiffness of the beam. We consider the axial and shear stiffness of the beam to be same, so that the second diagonal term of \mathbf{C}^* becomes E^* . Non-dimensional internal moment is defined in a similar fashion as $\tilde{m}^* = (L_0/EI)\tilde{m}$. The non-dimensional external force per unit length is defined as $\tilde{\mathbf{F}}^* = (L_0^2/EI)\tilde{\mathbf{F}}$ and the non-dimensional external moment per unit length of the beam is defined as $\tilde{M}^* = (L_0^2/EI)\tilde{M}$. The geometric

boundary conditions at $\zeta = 0$ are non-dimensionalised as

$$u_1^*(\zeta, t) = 0, \quad u_2^*(\zeta, t) = 0, \quad \text{and} \quad \theta^*(\zeta, t) = 0, \quad \text{at} \quad \zeta = 0, \quad (5.33)$$

and the non-dimensional force boundary conditions are:

$$f_1^*(\zeta, t) = 0, \quad f_2^*(\zeta, t) = 0, \quad \text{and} \quad m^*(\zeta, t) = 0, \quad \text{at} \quad \zeta = 1. \quad (5.34)$$

Thus we obtain the non-dimensionalised set of governing partial differential equations along with the boundary conditions at $\zeta = 0$ and $\zeta = 1$. Prior to moving into the computations, we now discuss the modeling of the aerostat, attached to the free end of the cable.

5.7 Modeling the aerostat

We model the aerostat as a rigid body, connected at the free end of the cable. However, computations for dynamics of GE cables, having rigid bodies attached to it requires special treatment. The classical Newmark time marching algorithm fails in this case, thus a symplectic integration scheme is introduced by [Simo and Wong \(1991\)](#). The aim of current work is to investigate the vibrations and stability of the cables, employed in deployment of aerostats. Thus, to avoid the complexity in computations, we model the aerostat as a combination of a rigid link and a rigid sphere mass m_a , whose centre is attached to the end of the link. We take the length of the link to be r_a — the distance between the cable end and centre of gravity of the aerostat; see [Fig. 5.4\(a\)](#). This rigid link is actually taken as a part of the GE cable, having very high stiffness against bending, tension and shear. Model of the aerostat is shown in [Fig. 5.4\(b\)](#), in which we assume the mass of the aerostat to be concentrated at the end of the link. The free body diagram of the sphere (model of the aerostat) is shown in [Fig. 5.4\(c\)](#). We now balance linear momentum of the rigid sphere in $\hat{\mathbf{E}}_1$ and $\hat{\mathbf{E}}_2$ directions to obtain, respectively,

$$m_a \ddot{u}_1(X_1, t) = -f_1(X_1, t) + F_b - m_a g,$$

and

$$m_a \ddot{u}_2(X_1, t) = -f_2(X_1, t),$$

respectively, at $X_1 = L$. We now express the above in terms of the mapped coordinate ζ as

$$\begin{aligned} m_a \left[\frac{\partial}{\partial \zeta} \left\{ \frac{(1-\zeta)^2 \dot{L}_1^2}{L_1^2} \frac{\partial \tilde{u}_1}{\partial \zeta} \right\} + 2 \frac{\partial^2 \tilde{u}_1}{\partial \zeta \partial t} \frac{(1-\zeta) \dot{L}_1}{L_1} + \frac{\partial \tilde{u}_1}{\partial \zeta} \frac{(1-\zeta) \ddot{L}_1}{L_1} + \frac{\partial^2 \tilde{u}_1}{\partial t^2} + \ddot{L}_1 \right] \\ = -f_1(\zeta, t) + F_b - m_a g, \end{aligned}$$

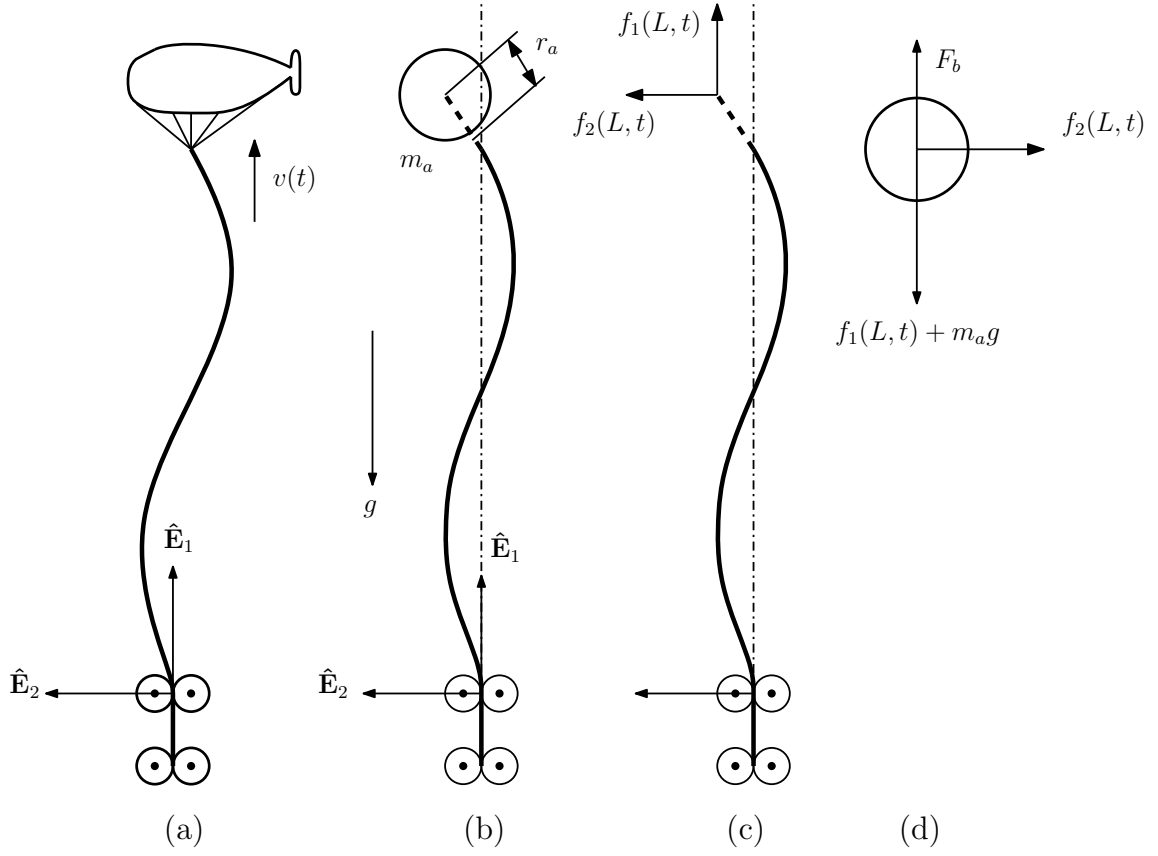


Fig. 5.4: (a) The system of our interest, (b) schematic diagram of the model of the aerostat, (c) schematic diagram of the cable, showing forces, acting on its end, (d) free body diagram of the rigid sphere (model of the aerostat).

$$\text{and} \quad m_a \left[\frac{\partial}{\partial \zeta} \left\{ \frac{(1-\zeta)^2 \dot{L}_1^2}{L_1^2} \frac{\partial \tilde{u}_2}{\partial \zeta} \right\} + 2 \frac{\partial^2 \tilde{u}_2}{\partial \zeta \partial t} \frac{(1-\zeta) \dot{L}_1}{L_1} + \frac{\partial \tilde{u}_2}{\partial \zeta} \frac{(1-\zeta) \ddot{L}_1}{L_1} + \frac{\partial^2 \tilde{u}_2}{\partial t^2} + \ddot{L}_1 \right] = -f_2(\zeta, t),$$

at $\zeta = 1$. The above simplify further to

$$m_a \left[\frac{\partial^2 \tilde{u}_1}{\partial t^2} + \ddot{L}_1 \right] = -f_1(\zeta, t) + F_b - m_a g, \quad (5.35)$$

$$\text{and} \quad m_a \frac{\partial^2 \tilde{u}_2}{\partial t^2} = -f_2(\zeta, t), \quad (5.36)$$

. at $\zeta = 1$. We now non-dimensionalise (5.35) and (5.36):

$$m_a^* \left[\frac{\partial^2 \tilde{u}_1^*}{\partial \bar{t}^2} + \ddot{\bar{t}} \right] = -f_1^*(\zeta, \bar{t}) + F_b^*, \quad (5.37)$$

$$\text{and} \quad m_a^* \frac{\partial^2 \tilde{u}_2^*}{\partial \bar{t}^2} = -f_2^*(\zeta, \bar{t}), \quad (5.38)$$

where $m_a^* = m_a L_0 / I_\rho$ and $F_b^* = (F_b - m_a g) L_0^2 / EI$. Rearranging the above two equations we obtain the modified set of non-dimensional boundary conditions at the upper end:

$$f_1^*(\zeta, \bar{t}) = -m_a^* \left[\frac{\partial^2 \tilde{u}_1^*}{\partial \bar{t}^2} + \ddot{i} \right] + F_b^*, \quad f_2^*(\zeta, \bar{t}) = -m_a^* \frac{\partial^2 \tilde{u}_2^*}{\partial \bar{t}^2}, \quad m^*(\zeta, \bar{t}) = 0, \quad \text{at } \zeta = 1. \quad (5.39)$$

We will take the above equation as the force boundary condition in the next chapter, where we will present computation scheme to solve (5.32).

5.8 Summary

In this chapter, we derived the equations of motion of a lengthening/shortening GE cable from first principles. We mapped the spatial domain into a constant domain by through a suitable mapping from X_1 to ζ . This was followed by non-dimensionalization of the governing partial differential equations and boundary conditions. Finally, we concluded by modifying the force boundary condition at $\zeta = 1$ by modeling the aerostat as a rigid sphere. We will consider (5.32) as the governing equation along with the boundary conditions (5.33) and (5.39) at $\zeta = 0$ and $\zeta = 1$, respectively. These will be solved in the next chapter by a finite element method.

Chapter 6

Computation and Validation

6.1 Introduction

In this chapter we develop a finite element(FE) formulation to solve (5.32) along with boundary conditions (5.33) and (5.39). Computations for GE beams were developed [Simo and Vu-Quoc \(1986b\)](#). This computation algorithm was extended to three dimensional GE beams in [Simo and Vu-Quoc \(1986c\)](#) and [Simo and Vu-Quoc \(1988\)](#). Axially lengthening/shortening GE beams were numerically investigated by [Vu-Quoc and Li \(1995\)](#).

To formulate a FE routine, we develop an weak form of (5.32), followed by linearisation and discretization in space. Next, we validate our computations against some benchmark problems. We also consider the global angular momentum balance for the system to further validate our code.

6.2 Weak form

We derive the weak form of (5.32) in order to obtain a spatially discrete set of equations. We will derive the weak form only for the first equation of the set (5.32) and then express the equations in a generalized matrix form. To this end we introduce a weighting function $w_1(\zeta)$ that satisfies the geometric boundary conditions (5.34) and obtain the weighted residual form:

$$\begin{aligned} \int_0^1 w_1 A_p \left[\frac{\partial}{\partial \zeta} \left\{ (1-\zeta)^2 \dot{l}^2 \frac{\partial u_1}{\partial \zeta} \right\} + 2 \frac{\partial^2 u_1}{\partial \zeta \partial t} (1-\zeta) \dot{l} + \frac{\partial u_1}{\partial \zeta} (1-\zeta) \ddot{l} + \frac{\partial^2 u_1}{\partial t^2} l^2 + \ddot{l}^2 \right] d\zeta \\ = \int_0^1 w_1 \frac{\partial f_1}{\partial \zeta} l d\zeta + \int_0^1 w_1 F_1 l^2 d\zeta, \end{aligned}$$

where we, henceforth, omit $(\bar{\cdot}),(\bar{\cdot})$ and (\cdot^*) from dimensionless variables. Integrating by parts the first and second terms in the left hand side and the first term in the right hand side of the above we obtain:

$$\begin{aligned} & A_\rho l^2 \int_0^1 w_1 \frac{\partial^2 u_1}{\partial t^2} d\zeta + A_\rho \dot{l} l \int_0^1 w_1 \frac{\partial^2 u_1}{\partial \zeta \partial t} (1 - \zeta) d\zeta - A_\rho \dot{l} l \int_0^1 \frac{\partial w_1}{\partial \zeta} (1 - \zeta) \frac{\partial u_1}{\partial t} d\zeta \\ & - A_\rho \dot{l}^2 \int_0^1 \frac{\partial w_1}{\partial \zeta} (1 - \zeta)^2 \frac{\partial u_1}{\partial \zeta} d\zeta + A_\rho \ddot{l} l \int_0^1 w_1 \frac{\partial u_1}{\partial \zeta} (1 - \zeta) d\zeta + l \int_0^1 \frac{\partial w_1}{\partial \zeta} f_1 d\zeta \\ & = l[w_1 f_1]_0^1 - A_\rho \ddot{l} l^2 \int_0^1 w_1 d\zeta + l^2 \int_0^1 w_1 F_1 d\zeta. \end{aligned} \quad (6.1)$$

Similarly, weak forms of the rest two equations of (5.32) are obtained. We now express kinematic variables u_1 , u_2 and θ and weighting functions as

$$\mathbf{U} = u_1 \hat{\mathbf{E}}_1 + u_2 \hat{\mathbf{E}}_2 + \theta \hat{\mathbf{E}}_3, \quad \text{and} \quad \mathbf{W} = w_i \hat{\mathbf{E}}_i.$$

We now express the weak form of (5.32) in operator form as

$$G_M(\mathbf{W}, \mathbf{U}) + G_V(\mathbf{W}, \mathbf{U}) + G_{LS}(\mathbf{W}, \mathbf{U}) + G_{NS}(\mathbf{W}, \mathbf{U}) + G_{IF}(\mathbf{W}) + G_F(\mathbf{W}) = 0, \quad (6.2)$$

where the mass operator is defined as

$$G_M(\mathbf{W}, \mathbf{U}) = l^2 \int_0^1 \mathbf{W} \cdot \mathbf{I} \cdot \frac{\partial^2 \mathbf{U}}{\partial t^2} d\zeta, \quad (6.3)$$

where \mathbf{I} is the inertia tensor, which is defined in \mathbf{E} as

$$[\mathbf{I}]_{\mathbf{E}} = \begin{bmatrix} A_\rho & 0 & 0 \\ 0 & A_\rho & 0 \\ 0 & 0 & I_\rho \end{bmatrix}.$$

From here onwards we will always express vectors and tensors in terms of the inertial coordinate \mathbf{E} . Henceforth, subscripts in vectors and matrices are suppressed. The velocity-convection operator is now defined as

$$G_V(\mathbf{W}, \mathbf{U}) = \dot{l} l \int_0^1 \left[(1 - \zeta) \left\{ \mathbf{W} \cdot \mathbf{I} \cdot \frac{\partial^2 \mathbf{U}}{\partial \zeta \partial t} - \frac{\partial \mathbf{W}}{\partial \zeta} \cdot \mathbf{I} \cdot \frac{\partial \mathbf{U}}{\partial t} \right\} \right] d\zeta, \quad (6.4)$$

and the linear stiffness operator is defined as

$$G_{LS}(\mathbf{W}, \mathbf{U}) = -\dot{l}^2 \int_0^1 (1 - \zeta)^2 \frac{\partial \mathbf{W}}{\partial \zeta} \cdot \mathbf{I} \cdot \frac{\partial \mathbf{U}}{\partial \zeta} d\zeta + \ddot{l} l \int_0^1 (1 - \zeta) \mathbf{W} \cdot \mathbf{I} \cdot \frac{\partial \mathbf{U}}{\partial \zeta} d\zeta. \quad (6.5)$$

The nonlinear stiffness operator is complicated:

$$\begin{aligned} G_{\text{NS}}(\mathbf{W}, \mathbf{U}) &= l \int_0^1 \left[\frac{\partial w_1}{\partial \zeta} f_1 + \frac{\partial w_2}{\partial \zeta} f_2 + \frac{\partial w_3}{\partial \zeta} m - w_3 \left(\frac{\partial \mathbf{r}_0}{\partial \zeta} \times \mathbf{f} \right) \cdot \mathbf{E}_3 \right] d\zeta \\ &= l \int_0^1 \mathcal{D}(\mathbf{U}) \mathbf{W} \cdot \mathbf{p}(\mathbf{U}) d\zeta, \end{aligned} \quad (6.6)$$

where $\mathcal{D}(\mathbf{U})$ is the differential operator, defined as

$$\mathcal{D}(\mathbf{U}) = \begin{bmatrix} \frac{\partial}{\partial \zeta} & 0 & \frac{\partial r_{0,2}}{\partial \zeta} \\ 0 & \frac{\partial}{\partial \zeta} & -\frac{\partial r_{0,1}}{\partial \zeta} \\ 0 & 0 & \frac{\partial}{\partial \zeta} \end{bmatrix},$$

in terms of

$$\frac{\partial r_{0,1}}{\partial \zeta} = l + \frac{\partial u_1}{\partial \zeta} \quad \text{and} \quad \frac{\partial r_{0,2}}{\partial \zeta} = \frac{\partial u_2}{\partial \zeta},$$

and $\mathbf{p}(\mathbf{U})$ is the resultant internal force vector

$$\mathbf{p}(\mathbf{U}) = f_1 \hat{\mathbf{E}}_1 + f_2 \hat{\mathbf{E}}_2 + m \hat{\mathbf{E}}_3,$$

where

$$\begin{bmatrix} f_1 \\ f_2 \\ m \end{bmatrix} = [\mathbf{\Lambda}]^T [\mathbf{C}] [\mathbf{\Lambda}] \begin{bmatrix} L + u_{1,\zeta} - l \cos \theta \\ u_{2,\zeta} - l \sin \theta \\ \theta_{,\zeta} \end{bmatrix}.$$

Finally, the sliding inertia force operator is

$$G_{\text{IF}}(\mathbf{W}) = l^2 \ddot{i} \int_0^1 \mathbf{W} \cdot A_\rho \mathbf{E}_1 d\zeta, \quad (6.7)$$

and the body force operator is

$$G_{\text{F}}(\mathbf{W}) = -l^2 \int_0^1 \mathbf{W} \cdot (F_1 \mathbf{E}_1 + F_2 \mathbf{E}_2 + M \mathbf{E}_3) d\zeta, \quad (6.8)$$

Where F_i are externally applied forces on the cable in $\hat{\mathbf{E}}_i$ direction and M is the external moment. We perform spatial discretization of this weak form in the next section and derive expressions for mass, velocity convection, and stiffness matrices.

6.3 Linearisation

In this section, we linearise $G_{\text{NS}}(\mathbf{W}, \mathbf{U})$ about a configuration \mathbf{U}_0 . This help us to obtain the subsequent configuration of \mathbf{U}_0 through a Newton-Raphson iteration. Note that all other operators in (6.2) are linear. To linearise $G_{\text{NS}}(\mathbf{W}, \mathbf{U})$ we consider a small perturbation $\Delta\mathbf{U}$ about \mathbf{U}_0 and set $\mathbf{U} = \mathbf{U}_0 + \Delta\mathbf{U}$. We now express $\mathcal{D}(\mathbf{U})$ and $\mathbf{p}(\mathbf{U})$ as

$$\mathcal{D}(\mathbf{U}) = \mathcal{D}(\mathbf{U}^{(0)} + \Delta\mathbf{U}) \quad (6.9)$$

and

$$\mathbf{p}(\mathbf{U}) = \mathbf{p}(\mathbf{U}^{(0)} + \Delta\mathbf{U}), \quad (6.10)$$

respectively. Substituting (6.9) and (6.10) into (6.6) and expanding them about \mathbf{U}_0 upto $O(\Delta\mathbf{U})$ yields

$$G_{\text{NS}}^{(\text{lin})} = G_{\text{NS}}^{(1)} + G_{\text{NS}}^{(2)},$$

where

$$G_{\text{NS}}^{(1)} = l \int_0^1 (\mathcal{D}(\mathbf{U}^{(0)})\mathbf{W})\mathbf{\Lambda}(\tilde{\mathbf{U}}^{(0)})\mathbf{C}\mathbf{\Lambda}^T(\mathbf{U}^{(0)})(\mathcal{D}(\mathbf{U}^{(0)})\Delta\mathbf{U})d\zeta, \quad (6.11)$$

and

$$G_{\text{NS}}^{(2)} = l \int_0^1 (\bar{\mathcal{D}}\mathbf{W})\mathbf{G}(\mathbf{U}^{(0)})(\bar{\mathcal{D}}\Delta\mathbf{U})d\zeta, \quad (6.12)$$

with the differential operator

$$[\bar{\mathcal{D}}] = \begin{bmatrix} \frac{\partial}{\partial\zeta} & 0 & 0 \\ 0 & \frac{\partial}{\partial\zeta} & 0 \\ 0 & 0 & 1 \end{bmatrix},$$

and

$$[\mathbf{G}(\mathbf{U}^{(0)})] = \begin{bmatrix} 0 & 0 & -f_2(\mathbf{U}^{(0)}) \\ 0 & 0 & f_1(\mathbf{U}^{(0)}) \\ -f_2(\mathbf{U}^{(0)}) & f_1(\mathbf{U}^{(0)}) & -[(l + u_{1,\zeta}^{(0)})f_1(\mathbf{U}^{(0)}) + u_{2,\zeta}^{(0)}f_2(\mathbf{U}^{(0)})] \end{bmatrix}.$$

Finally, the linearised weak form of (6.2) about a configuration \mathbf{U}_0 as

$$\begin{aligned} G_{\text{M}}(\mathbf{W}, \Delta\mathbf{U}) + G_{\text{V}}(\mathbf{W}, \Delta\mathbf{U}) + G_{\text{LS}}(\mathbf{W}, \Delta\mathbf{U}) + G_{\text{NS}}^{(1)}(\mathbf{W}, \Delta\mathbf{U}) + G_{\text{NS}}^{(2)}(\mathbf{W}, \Delta\mathbf{U}) \\ + R(\mathbf{W}) + G_{\text{IF}}(\mathbf{W}) + G_{\text{F}}(\mathbf{W}) = 0, \end{aligned} \quad (6.13)$$

where

$$R(\mathbf{W}) = l \int_0^1 \mathcal{D}(\mathbf{U}_0) \mathbf{W} \cdot \mathbf{p}(\mathbf{U}_0) d\zeta$$

is the residue vector. We are now in a position to discretize (6.13) in space.

6.4 Spatial discretization

We perform spatial discretization through Galerkin projection as in [Simo and Vu-Quoc \(1986b\)](#); [Vu-Quoc and Li \(1995\)](#). We divide the computation domain $0 \leq \zeta \leq 1$ into several intervals and introduce shape functions to approximate $\Delta \mathbf{U}$ and \mathbf{W} as

$$\Delta \mathbf{U} = \sum_{i=1}^n \mathbf{N}_i(\zeta) \Delta \mathbf{q}_i(t) \quad (6.14)$$

and

$$\mathbf{W} = \sum_{i=1}^n \mathbf{N}_i(\zeta), \quad (6.15)$$

respectively, where n is the number of nodes in an interval,

$$[\mathbf{N}_i] = \begin{bmatrix} N_i & 0 & 0 \\ 0 & N_i & 0 \\ 0 & 0 & N_i \end{bmatrix},$$

is the shape function matrix and $\mathbf{q}(t)$ is the temporal variation of \mathbf{U} . We now consider two node linear elements for discretization and obtain the element mass matrix from (6.3) as

$$[\mathbf{M}](t) = l^2 [\mathbf{M}^{(\alpha\beta)}], \quad (6.16)$$

where

$$[\mathbf{M}^{(\alpha\beta)}] = \int_{\zeta_1}^{\zeta_2} [\mathbf{N}_\alpha][\mathbf{I}][\mathbf{N}_\beta] d\zeta,$$

with $\alpha, \beta = i, j$; see [App. B](#) for derivation. The velocity convection matrix for an element is

$$[\mathbf{S}](t) = l \dot{l} [\mathbf{S}^{(\alpha\beta)}], \quad (6.17)$$

where

$$[\mathbf{S}^{(\alpha\beta)}] = \int_{\zeta_1}^{\zeta_2} (1 - \zeta) [\mathbf{N}_\alpha][\mathbf{I}][\mathbf{N}_{\beta,\zeta}] - (1 - \zeta) [\mathbf{N}_{\alpha,\zeta}][\mathbf{I}][\mathbf{N}_\beta] d\zeta.$$

Similarly, linear element stiffness matrix is expressed as

$$[\mathbf{K}_l](t) = -\dot{l}^2[\mathbf{K}_{l(1)}^{(\alpha\beta)}] + \ddot{l}[\mathbf{K}_{l(2)}^{(\alpha\beta)}], \quad (6.18)$$

where

$$[\mathbf{K}_{l(1)}^{(\alpha\beta)}] = \int_{\zeta_1}^{\zeta_2} (1 - \zeta)^2 [\mathbf{N}_{\alpha,\zeta}] [\mathbf{I}] [\mathbf{N}_{\beta,\zeta}] d\zeta,$$

and

$$[\mathbf{K}_{l(2)}^{(\alpha\beta)}] = \int_{\zeta_1}^{\zeta_2} (1 - \zeta) [\mathbf{N}_{\alpha}] [\mathbf{I}] [\mathbf{N}_{\beta,\zeta}] d\zeta,$$

and element stiffness matrices, arising from $G_{\text{NS}}^{(\text{lin})}$ are expressed as

$$[\mathbf{K}_{n(1)}^{(\alpha\beta)}] = l \int_{\zeta_1}^{\zeta_2} [\mathcal{D}(\mathbf{q}^{(0)}) N_{\alpha}] [\mathbf{\Lambda}(\mathbf{q}^{(0)})] [\mathbf{C}] [\mathbf{\Lambda}(\mathbf{q}^{(0)})]^T [\mathcal{D}(\mathbf{q}^{(0)}) N_{\beta}] d\zeta, \quad (6.19)$$

and

$$[\mathbf{K}_{n(2)}^{(\alpha\beta)}] = l \int_{\zeta_1}^{\zeta_2} [\bar{\mathcal{D}} N_{\alpha}] [\mathbf{G}(\mathbf{q}^{(0)})] [\bar{\mathcal{D}} N_{\beta}] d\zeta. \quad (6.20)$$

The column of residue vector, is computed as

$$[\mathbf{R}^{(\alpha)}] = l \int_{\zeta_1}^{\zeta_2} [\mathcal{D}(\mathbf{q}^{(0)}) N_{\alpha}] \{\mathbf{p}(\mathbf{q}^{(0)})\} d\zeta. \quad (6.21)$$

Thus, we obtain all the relevant element stiffness matrices through spatial discretization. These matrices are then combined to get global mass, convection and stiffness matrices. We manipulate the global matrices to take care of the geometric boundary condition at $\zeta = 0$ and force boundary condition at $\zeta = 1$. We note that at $\zeta = 1$, force boundary condition is given by (5.39). This is taken care of by addition of the following matrix with the free end element mass matrix:

$$[\mathbf{M}]_a = \begin{bmatrix} m_a & 0 & 0 \\ 0 & m_a & 0 \\ 0 & 0 & 0 \end{bmatrix},$$

where m_a is the mass of the aerostat. Contributions from net buoyancy force F_b and sliding force $m_a \ddot{l}$ (as in (5.39)) are added to the external force column. Thus, spatial discretization of (6.13) is carried out. We now present a time marching scheme, that is used in the FE computations.

6.5 Time marching

Classical Newmark β algorithm is employed to compute the temporal evolution of \mathbf{q} . The algorithm of this method is discussed in detail in (Simo and Vu-Quoc, 1986b, 1988) and (Vu-Quoc and Li, 1995). We select time marching parameters β and γ , suitably so that the algorithm remains

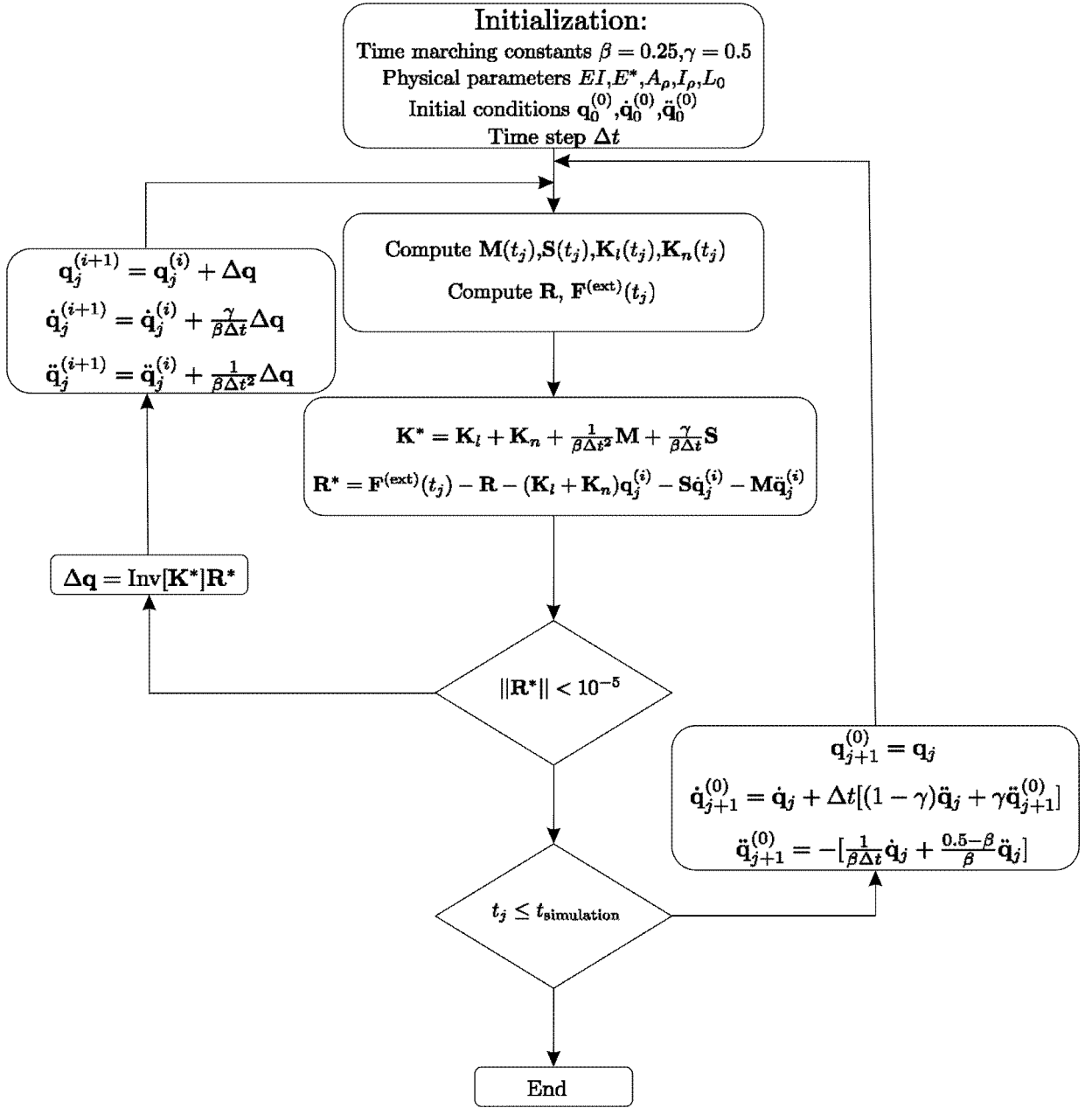


Fig. 6.1: Flowchart of computation scheme using Newmark time marching algorithm.

unconditionally stable. [Figure 6.1](#) shows the full computational algorithm for GE beams. Here the subscripts indicate the iteration number of time marching and superscripts denotes the number of Newton-Raphson iterations. We stop the Newton-Raphson iterations when the Euclidian norm of total residue $\|\mathbf{R}^*\|$ becomes less than a prescribed convergence tolerance. We set this tolerance to 10^{-5} in our computations. The computations are executed in MATLAB; see [App. C](#) for the code. We present validations of our computation in the next section.

6.6 Validation of the computation routine

We now validate our code against a benchmark problem of *pure bending of a cantilever beam*. This is followed by validation against a simulation result for damped vibration of a cantilever beam obtained by [Simo and Vu-Quoc \(1986b\)](#). We conclude this section by computing the total angular momentums of lengthening/shortening beams and compare them with net applied moment to the system.

6.6.1 Pure bending of a cantilever beam

The classical solution for pure bending of a cantilever beam gives the radius of curvature as $R = EI/M$, where M is the applied bending moment at the end of the cantilever; see ([Simo and Vu-Quoc, 1986c](#)). We now take a GE cantilever beam of length $l_0 = 1$. We see that, if EI is taken to be 2 and M to be 4π then, the cantilever should become a circle of radius $R = 1/2\pi$. This classical solution for pure bending of cantilever beams is also obtained by [Simo and Vu-Quoc \(1986c\)](#). First, we take a GE beam with 10 uniformly spaced elements and applied an end-moment of magnitude 4π in a single step. We see in [Fig. 6.2\(a\)](#) that under this moment the cantilever becomes a circle of radius $R = 0.1591/2\pi \approx$. Next, we perform the same

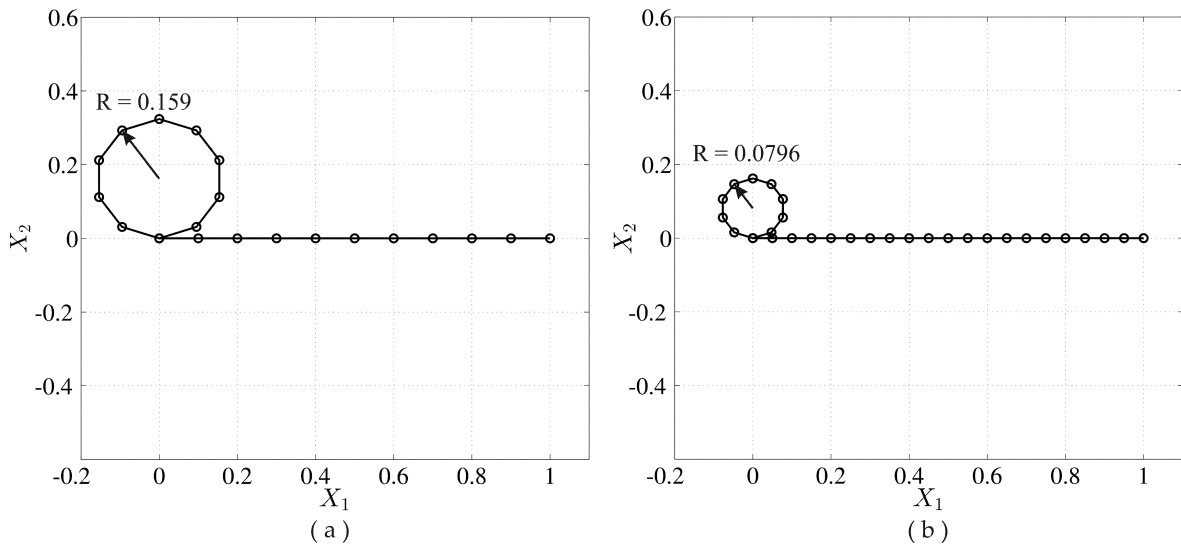


Fig. 6.2: (a) An uniform cantilever beam of $EI = 2$, subjected to a constant end-moment $M = 4\pi$, (b) the same beam, subjected to constant end-moment $M = 8\pi$.

investigation with $M = 8\pi$ and considering 20 uniformly spaced elements in the cantilever. We see in [Fig. 6.2\(b\)](#) that now the cantilever becomes rounded twice — forming a circle of radius $R = 0.0796 \approx 1/4\pi$.

6.6.2 Damped vibration of a cantilever beam

We now investigate an example problem for damped oscillation of a GE cantilever beam previously considered by [Simo and Vu-Quoc \(1986b\)](#). We take the beam to be of length $l_0 = 10$ and take 10 uniform elements of uniform length. The physical properties of the beam are: $EA = GA = 10^6$, $EI = 1000$, $A_\rho = 1$ and $I_\rho = 10$. Time step is considered to be $\Delta t = 0.001$. The cantilever beam is initially perturbed with a concentrated transverse force at its end; see [Fig. 6.3\(a\)](#). Coefficient of linear damping is taken to be $\mu = 0$ at the time of forcing and $\mu = 0.1$, after the force is released. Here the linear viscous damping model is considered by [Simo and Vu-Quoc \(1986b\)](#) and it is stated that more general dissipative mechanisms require a separate treatment. We see in [Fig. 6.3\(b\)](#) that the outcome from the present code matches

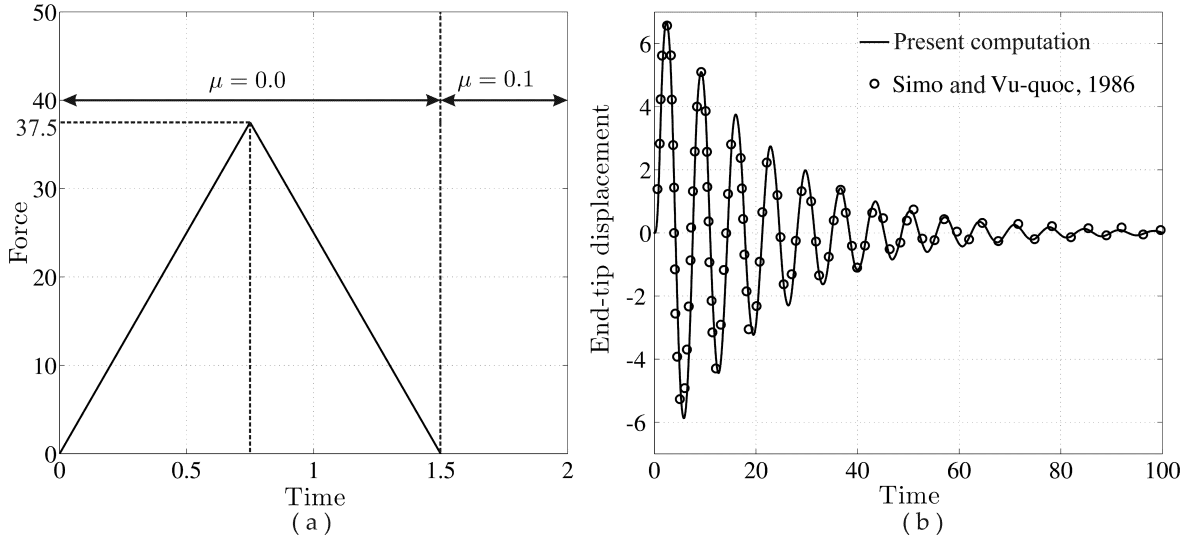


Fig. 6.3: (a) Profile of the transverse force, applied at the free end of the cantilever, (b) time series of damped oscillations of the cantilever.

the simulation results by [Simo and Vu-Quoc \(1986b\)](#). Amplitude of oscillation of the cantilever decreases due to damping and eventually becomes very small for $t > 100$.

6.6.3 Free vibrations of lengthening/shortening beams

The validations presented so far were for GE cantilever beams of constant length. We now validate our code for axially lengthening/shortening cantilever beams. We consider two cases: (a) lengthening at a rate of $v = 0.2 \text{ ms}^{-1}$ from an initial length of $L_0 = 10 \text{ m}$, followed by (b) investigations of a beam shortening at a rate of $v = 0.2 \text{ ms}^{-1}$ from an initial length of $L_0 = 10 \text{ m}$. In all cases, we consider the initial configuration of the cantilever to be as in [Fig. 6.4](#).

We check convergence of the routine by plotting the temporal evolution of total energy. We plot evolution of total energy of the system, taking different time steps Δt . We express the kinetic

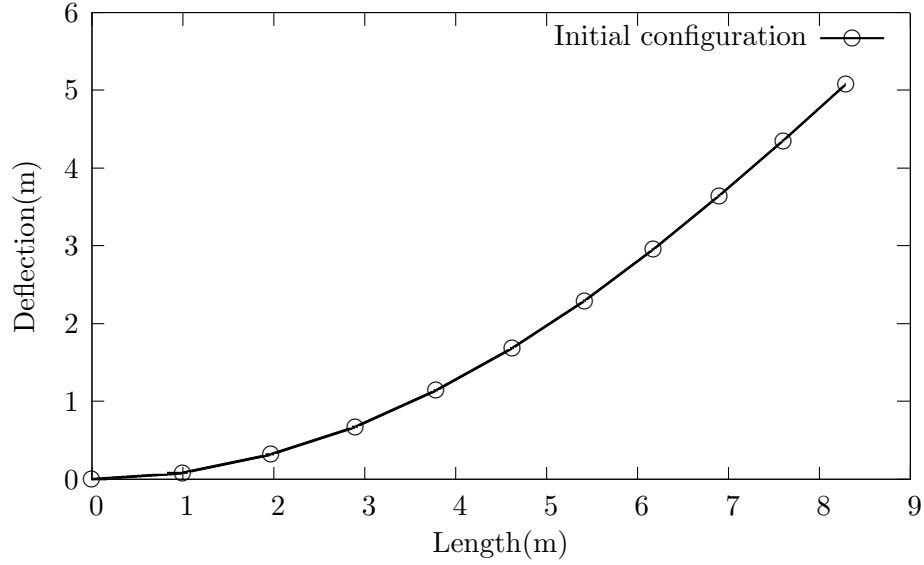


Fig. 6.4: Initial configuration of the cantilever beam.

energy of the system (as in [Simo and Vu-Quoc \(1986a\)](#)) as

$$E_k = \frac{1}{2} \int_0^{L_1(t)} [A_\rho(\dot{u}_1^2 + \dot{u}_2^2) + I_\rho \dot{\theta}^2] dX_1, \quad (6.22)$$

and potential energy as

$$E_p = \frac{1}{2} \int_0^{L_1(t)} [EA\Gamma_1^2 + GA\Gamma_2^2 + EI(\theta')^2] ds, \quad (6.23)$$

where s is the arc length parameter. It is shown by [Simo and Vu-Quoc \(1986a\)](#) that $\mathbf{\Gamma}$ remain invariant under superposed rigid body motions. Thus we rewrite the above in reference frame as

$$E_p = \frac{1}{2} \int_0^{L_1(t)} [EA\Gamma_1^2 + GA\Gamma_2^2 + EI(\theta')^2] dX_1. \quad (6.24)$$

We now express (6.22) and (6.24) in terms of the mapped primary variable ζ . We employ the transformations as shown in [Chapter 5](#) and perform computations for total energy.

We validate our code by balancing the rate of change of angular momentum of the system with net external moment. We note that the reaction moment at the fixed end of the beam is the only external moment on the system. Thus, rate of change of total angular momentum of the system must balance the moment at the fixed end. We compute total angular momentum with respect to the fixed end (as in [Simo and Vu-Quoc \(1986a\)](#)) as

$$\mathbf{H} = \int_0^{L_1(t)} \int_{-d}^d [\mathbf{r} \times (\rho \dot{\mathbf{r}})] dX_2 dX_1, \quad (6.25)$$

where then beam is taken to be of diameter $2d$. We now express the above as

$$\mathbf{H} = \int_0^{L_1(t)} \int_{-d}^d [(\mathbf{r} - \mathbf{r}_0) \times (\rho \dot{\mathbf{r}}) + \mathbf{r}_0 \times (\rho \dot{\mathbf{r}})] dX_2 dX_1. \quad (6.26)$$

The above expression of global angular momentum of the system is now expressed in convenient form as

$$\mathbf{H} = \int_0^{L_1(t)} [I_\rho \dot{\theta} \mathbf{E}_3 + \mathbf{r}_0 \times (A_\rho \dot{\mathbf{r}}_0)] dX_1. \quad (6.27)$$

We now express \mathbf{H} in terms of the mapped variable ζ as per the transformations, shown in [Chapter 5](#) and perform computations.

We now show validations of the FE routine. First, we consider a lengthening beam. We plot

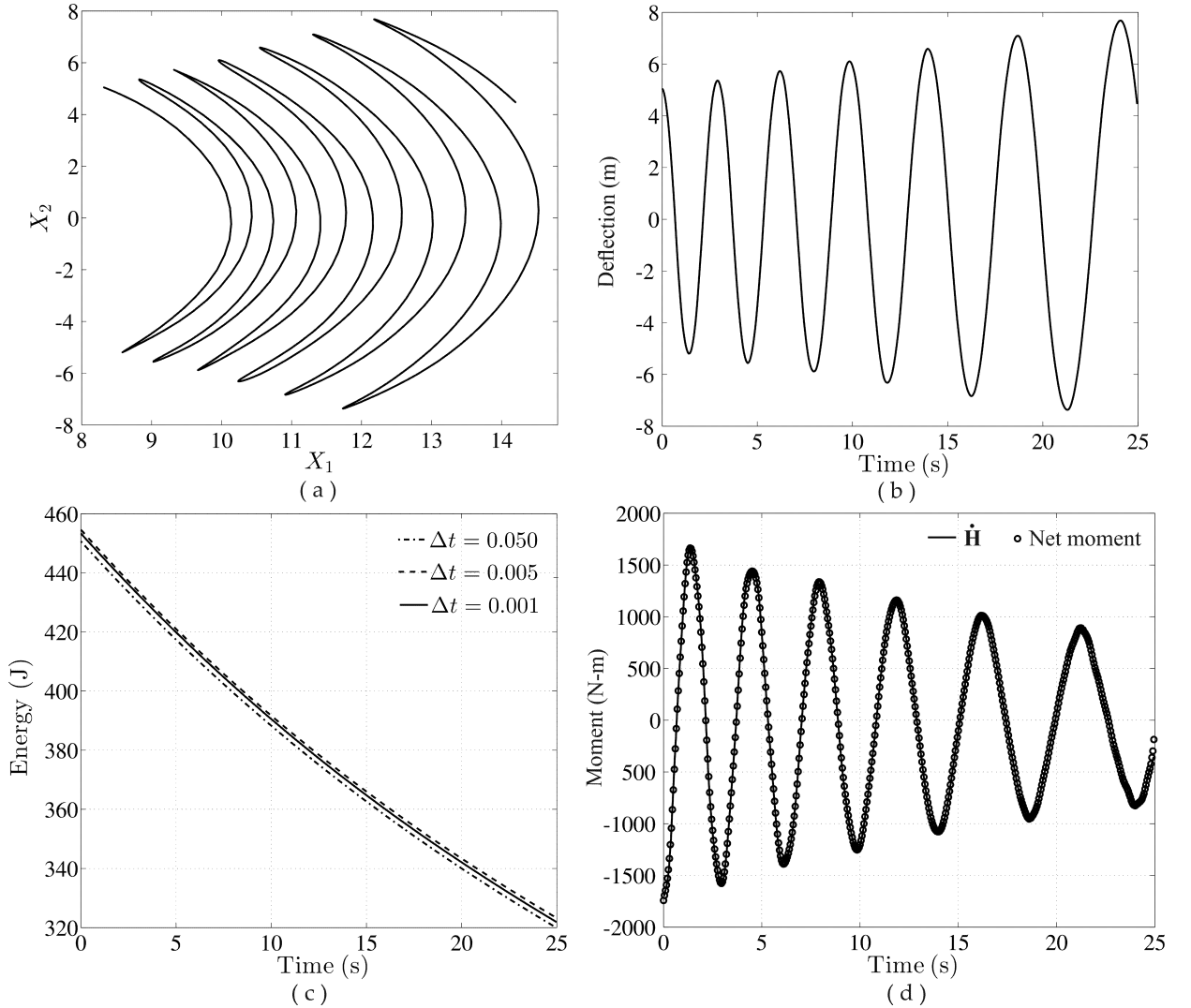


Fig. 6.5: (a) End-tip trajectory, (b) time series of the end-tip displacement, (c) evolution of the total energy in time, (d) angular momentum balance of a cantilever beam, lengthening at a rate of 0.2 ms^{-1} from an initial length $L_0 = 10 \text{ m}$.

the locus of the end-point and time series of the end-tip deflection of the cantilever in Figs. 6.5(a) and (b), respectively. We plot temporal evolution of total energy in Fig. 6.5(c). We note that as obtained for the linear string model, here also the total energy of the system decreases for lengthening beams. We also note that convergence is achieved by lowering Δt .

Next, we plot the rate of change of global angular momentum $\dot{\mathbf{H}}$ in Fig. 6.5(d). We see that $\dot{\mathbf{H}}$ equals the variation of the end moment at the fixed end of the cantilever. We also note that $\dot{\mathbf{H}}$ decreases as the length of the beam increases. This is due to decrease in the velocity of the material points with lengthening of the beam.

Similarly, we plot the locus of the end-tip and the time series of its oscillation, for a shortening beam in Figs. 6.6(a) and (b), respectively. Temporal variation of total energy is shown in Fig.

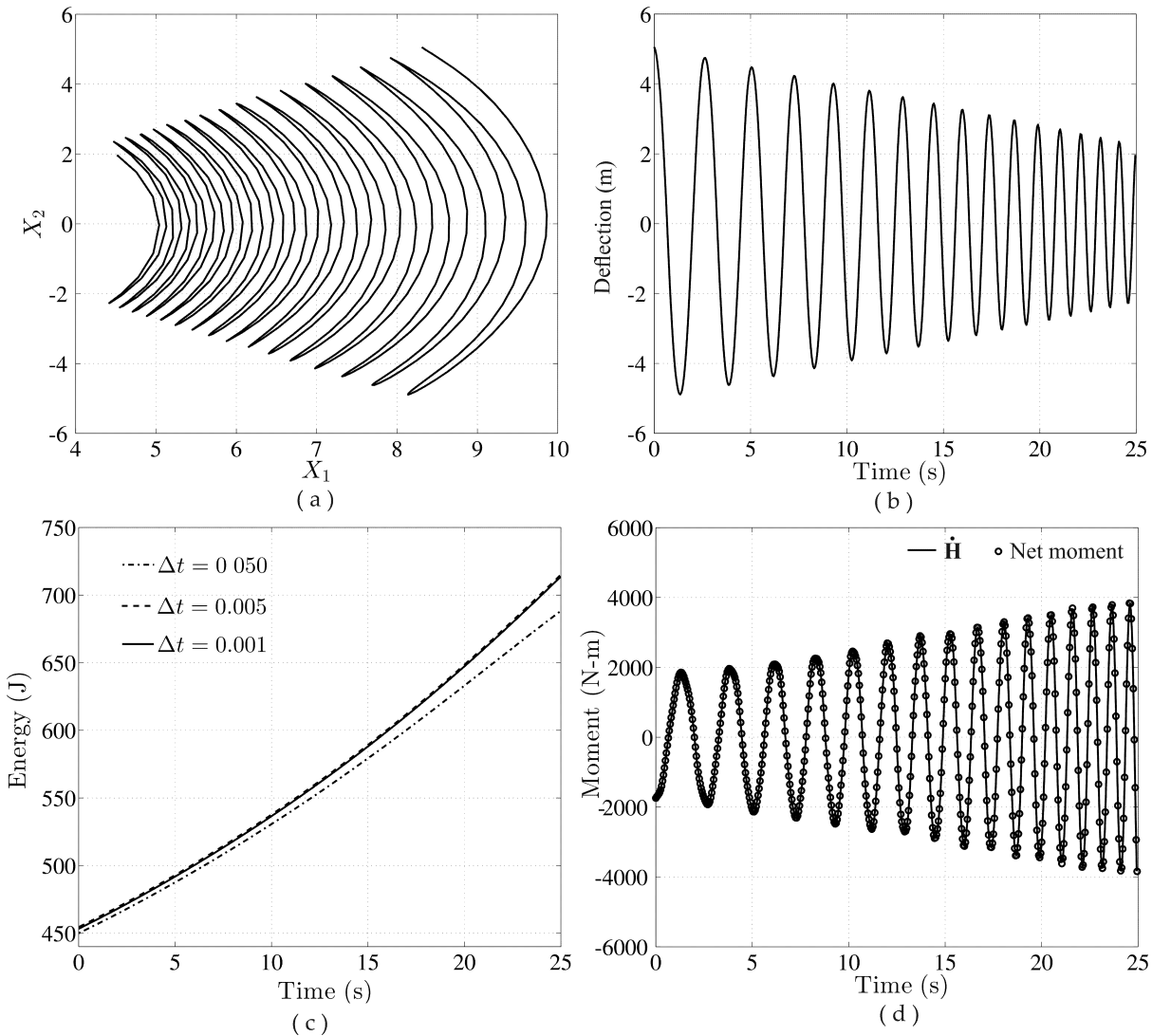


Fig. 6.6: (a) End-tip trajectory, (b) time series of the end-tip displacement, (c) evolution of the total energy in time, (d) angular momentum balance of a cantilever beam, shortening at a rate of 0.2 ms^{-1} from an initial length $L_0 = 10 \text{ m}$.

6.6(c). As seen for the linear cable model, here also, we see that total energy increases for a

shortening beam. Next, we plot $\dot{\mathbf{H}}$ along with the end moment at the fixed end in Fig. 6.6(d). Here we note that $\dot{\mathbf{H}}$ increases with time. This is due to increase in the velocity of material points of a shortening cantilever. As seen in Fig. 6.6(b), frequency of oscillation increases for a shortening cantilever, causing the velocity of its material points to increase. This causes total energy and $\dot{\mathbf{H}}$ to increase and eventually blow up to infinity as $L(t) \rightarrow 0$.

6.7 Summary

In this chapter a full FE algorithm is developed and implemented for lengthening/shortening GE cables. The computation routine is verified with various benchmark problems. We also validate the routine for lengthening/shortening cables by verifying the balance of total energy and global angular momentum of the system. We now proceed to stability analysis of lengthening/shortening cables.

Chapter 7

Stability Analysis of Lengthening/Shortening GE Cables

7.1 Introduction

Axially moving continua are susceptible to instabilities ([Wickert and Mote, 1990, 1991](#); [Parker, 1999](#); [Zajackowski and Lipiński, 1979](#)). In [Chapter 4](#), we saw that a lengthening cable always goes unstable after a certain time for a given rate of lengthening. There we analysed *quasi static* linear stability of lengthening/shortening cables through Lyapuniv's method ([LaSalle and Lefschetz, 1961](#)). In this chapter, we investigate stability of constant rate lengthening/shortening GE cables.

7.2 Stability analysis

In this section, we investigate stability of geometrically nonlinear systems. This is not as direct as stability analysis of linear systems (as in [Chapter 4](#)). Here the system is flexible and can undergo large deflection from the equilibrium. Thus, in this case it is convenient to analyse its stability about a *local dynamic equilibrium*. The local dynamic equilibrium is obtained by Newton-Raphson iteration of the following equation, obtained by spatial discretization followed by linearisation of the governing partial differential equations about its previous equilibrium configuration:

$$\mathbf{M}(t)\Delta\ddot{\mathbf{U}} + \mathbf{C}\Delta\dot{\mathbf{U}} + \mathbf{K}\Delta\mathbf{U} = \mathbf{R}(t), \quad (7.1)$$

where $\mathbf{R}(t)$ is the residual force column. This $\mathbf{R}(t)$ is the summation of external and inertial forces. Internal forces arises due to linearization of the system about the equilibrium position,

which leads to residual forces. This residual forces along with external forces in then balanced by incrementing \mathbf{U} as $\mathbf{U} + \Delta\mathbf{U}$. The iteration is stopped when the Euclidian norm of $\mathbf{R}(t)$ becomes less than certain convergence tolerance (here taken to be 10^{-5}). Thus, after achieving a new equilibrium configuration, we express (7.1) as

$$\mathbf{M}(t)\Delta\ddot{\mathbf{U}} + \mathbf{C}\Delta\dot{\mathbf{U}} + \mathbf{K}\Delta\mathbf{U} = 0. \quad (7.2)$$

We may interpret the above set of homogeneous ordinary differential equations as the equations of small linear oscillations $\Delta\mathbf{U}$ about any j^{th} configuration $\mathbf{U}^{(j)}$. A stability analysis of (7.2) by Lyapunov's method (see (LaSalle and Lefschetz, 1961)) refers to a linear stability analysis of the system, linearised about the j^{th} equilibrium position $\mathbf{U}^{(j)}$. Since we perform stability analysis about a *local configuration*, it is also known as *quasi-static* stability analysis (Nawrotzki and Eller, 2000). We term this as *local stability* analysis of GE cables. We now guess a solution to (7.2) as $\Delta\mathbf{U}(t) = \Delta\mathbf{U}_0\exp(\lambda t)$. Substitution of this in (7.2) leads to a polynomial eigenvalue problem as

$$\lambda^2\mathbf{M}(t)\Delta\mathbf{U}_0 + \lambda\mathbf{C}\Delta\mathbf{U}_0 + \mathbf{K}\Delta\mathbf{U}_0 = 0. \quad (7.3)$$

On solving the above eigenvalue problem, we obtain the eigenvalues $\lambda^{(i)}$, corresponding to i^{th} mode, for which the eigenvector is $\Delta\mathbf{U}_0^{(i)}$. We define the configuration $\mathbf{U}^{(j)}$ to be stable, whenever $\text{Re}(\lambda) \leq 0$ for all λ . Notions of stability, that result from λ being complex are summarized in table 4.1.

Since our interest lies in the stability analysis of lengthening/shortening cables, we do not investigate the eigenmode shapes of linearised oscillations about an instantaneous equilibrium position. Rather, we compute the eigenvalues after each equilibrium position is achieved. We now investigate some cases in the next section. This case studies will reflect how a *local* stability analysis predicts the stability of the system.

7.3 Stability of lengthening cables

In this section, we present stability analysis of a lengthening GE cable. We let the cable lengthen at various constant rates, after perturbing its end-mass with a constant force $F_0 = 400\text{N}$. Various physical parameters, considered for computations are given in table 7.1. We see in Fig 7.1(a) that the cable, which is lengthening at a constant rate $v = 12 \text{ ms}^{-1}$, stops oscillating after time t^* . Instead, it starts diverging from the equilibrium position, giving rise to instability. Instability in the cable is also indicated by temporal evolutions of the eigenvalues λ . We see in Fig 7.1(b) that the first eigenvalue posses a positive real part for $t > t^*$ and simultaneously, the imaginary part of it goes to zero. We also note from Fig 7.1(b) that the real parts of second and third eigenvalues remains zero throughout the computation time. Thus, we see from Figs 7.1(a) and (b) that a *local* instability of a configuration eventually leads the system to be unstable.

Table 7.1: Physical data, used in computation

Density of the material ρ (in Kgm^{-3})	7800
Cross section A (in m^2)	0.00001
Net buoyancy force F (in N)	1000
End mass m (in Kg)	10
Bending stiffness EI (in Nm^{-1})	1000
Axial/Bending stiffness (E^*)	10^5
$\tilde{\gamma} = A\rho L_0/I\rho$	1
Initial length of cable L_0 (in m)	1

Next, we do computations for a cable, lengthening at a rate of $v = 24 \text{ ms}^{-1}$, which is twice of the previous one. As shown in Fig 7.1(c), we note that the cable goes unstable earlier as compared to Fig 7.1(a). We also note that, the time t^* , upto which, the cable remains stable, is almost halved in the second case.

We note that lengthening GE cables behaves in a qualitatively similar manner to lengthening linear cables. As the rate of deployment increases, the critical time t^* , upto which the cable remains stable, comes down. The variation of critical time t^* with the rate of deployment v is shown in Fig 7.2(a). We develop the deployment charts in Figs 7.2(a) and (b), considering initial perturbation in the cable to be zero. This is unlike the initial perturbation, we considered in Figs 7.1(a) and (c). We note that the velocity of waves in a cable of constant length $L_0 = 1 \text{ m}$ is near 117 ms^{-1} , given physical parameters as table 7.1. Our computation also shows that at deployment at a rate $v > 117 \text{ ms}^{-1}$ leads to immediate instability. In this condition, the rate of deployment exceeds the speed of travelling wave in the cable — allowing the material points to move at a greater speed than the wave speeds in the cable. Waves speed in the cable is inversely proportional to its length. Thus, we see in Fig 7.2(a) that a greater length of the cable leads to instability at a lower rate of deployment.

From Fig 7.2(a), we obtain a critical time t^* for a given rate v , from which, we calculate maximum elevation $h^* = vt^*$ — upto which the aerostat can be deployed safely. The variation of h^* with v is shown in Fig 7.2(b). We also note that h^* increases if the v is set to be low. Slope of the curve, shown in Fig 7.2(b) becomes very small for $v \leq 30 \text{ ms}^{-1}$. Thus, we can conclude that, maximum elevation can be achieved if the rate of deployment is set to be less than 30 ms^{-1} . We see that Fig 7.2(b) is also qualitatively similar to Fig 4.2(b), which was developed for a linear cable model. We now compare the deployment charts of GE and linear cable models and investigate the limits, upto which these two models are comparable. We will see that some interesting physics, which cannot be captured by the liner model, are captured successfully by GEBT.

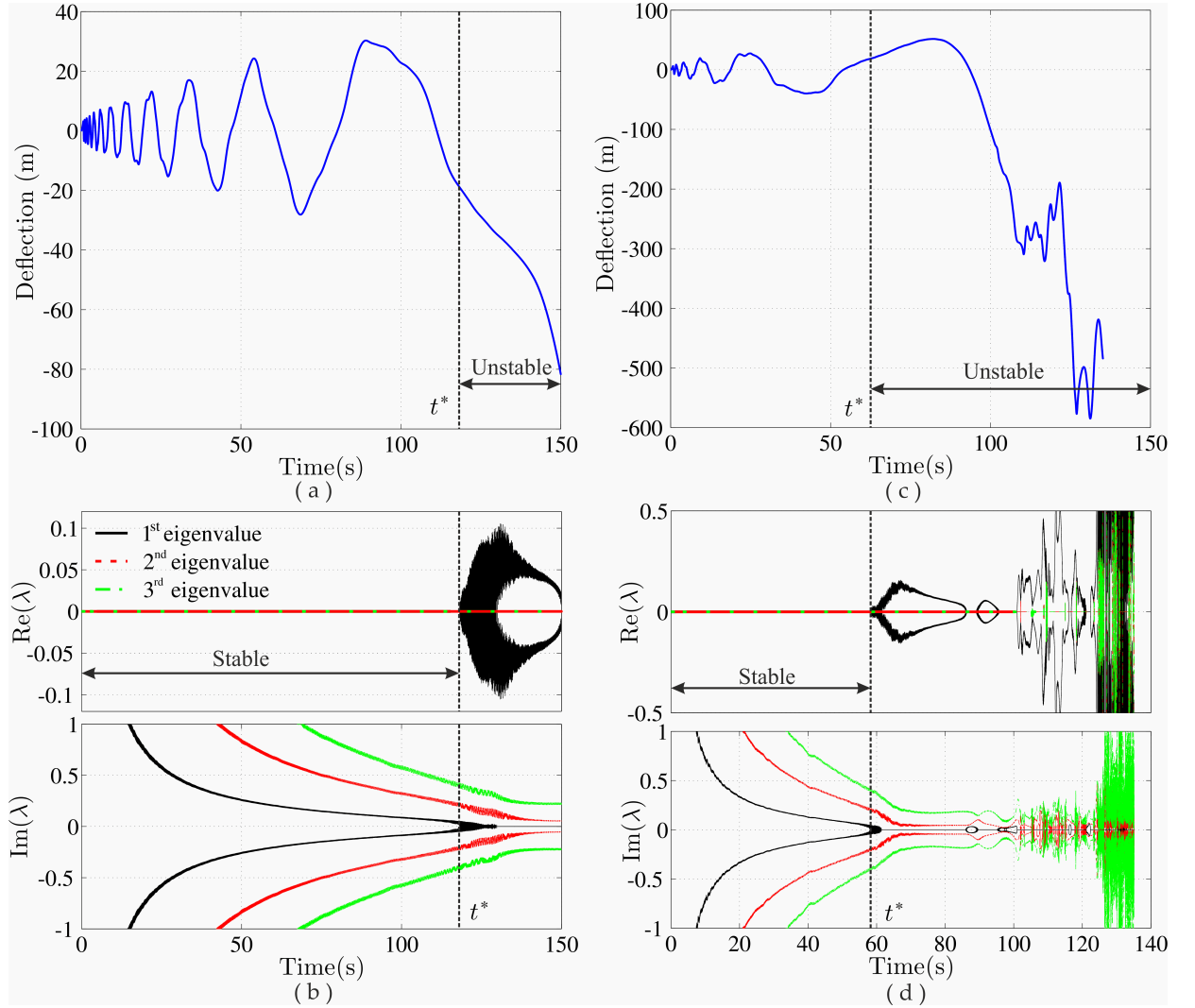


Fig. 7.1: (color online)(a) Time series of end-tip deflection, (b) evolutions of first three eigenvalues in time of a cable, lengthening at $v = 12 \text{ ms}^{-1}$. (c) Time series of end-tip deflection, (d) evolutions of first three eigenvalues in time of a cable, lengthening at $v = 24 \text{ ms}^{-1}$

7.4 Comparison with linear string model

We now compare the deployment charts, as shown in Figs 7.2(a) and (b) with that developed for a linear string model in Chapter 4. We have chosen the bending stiffness EI and mass per unit length $A\rho$ of the cable in such a way, that initially wave speeds in both linear and GE cables remain the same. Here we present all our results in dimensional form, as the non-dimensionalisation schemes for linear and GE cables are different. A comparison of deployment rate versus time plot for GE cables with linear cables is shown in Fig 7.3(a). Here we plot v versus t^* for various non-dimensional stiffness ratios E^* . The non-dimensional stiffness ratio E^* is the non-dimensional ratio of the axial stiffness to the bending stiffness of the cable — defined in Chapter 5. We keep the bending stiffness of the cable to be constant and vary E^* . We note

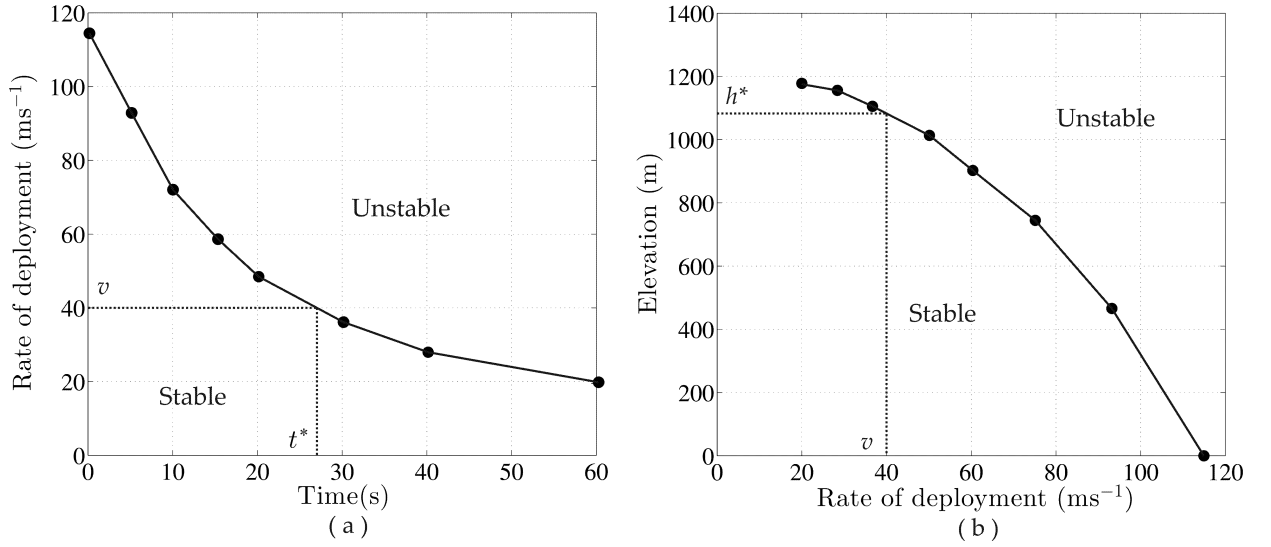


Fig. 7.2: Deployment charts: (a) variation of maximum rate of deployment v with time, (b) maximum achievable elevation with v .

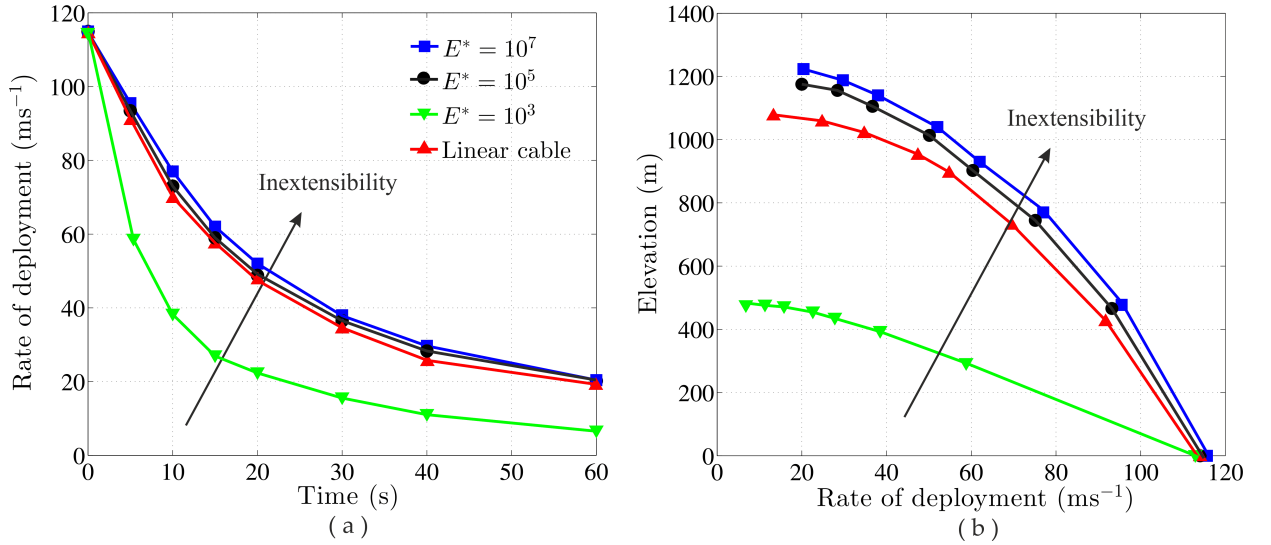


Fig. 7.3: (color online) Deployment charts (a) t^* vs. v plot for GE cables of various E^* along with the t^* vs. v plot for the linear cable model, (b) v vs. h^* plot for GE cables of various E^* and that for linear cable model.

that, for a constant bending stiffness EI , a higher value of E^* implies higher axial stiffness, which means the cable is inextensible.

We observe from Fig 7.3(a) that stability limits for an unperturbed, inextensible GE cable is commensurate to that of a linear string model, which is assumed to be inextensible. As shown in Fig 7.3(a), for a given rate v , an extensible GE cable becomes unstable earlier than an inextensible one. We also note from Fig 7.3(a) that the stability limits do not change for $E^* \geq 10^5$. Thus, we can conclude that, for $E^* \geq 10^5$, a GE cable becomes sufficiently inextensible so that it could behave like a linear cable.

Similarly, we see in Fig 7.3(b) that the limit of maximum allowable elevation for an inextensible GE cable is commensurate to that for a linear string model. In the other hand, the maximum allowable elevation gets reduced with increase in the extensibility of the cable.

We now consider only inextensible cables in the following computations. From here onwards, we fix E^* to be 10^5 and carry out computations. We saw that, the stability characteristics of an unperturbed, inextensible GE cable is similar to that of a linear cable. However, the cables, used in deployment of aerostat, may be subjected to high initial perturbations.

We now investigate the stability of GE cables, subjected to high initial perturbations. In all the cases, considered here, we will initially perturb the aerostat by a horizontal force. Modified deployment chart for various initial perturbations are shown in Fig 7.4(a) and the initial configurations of the cable are shown in Fig 7.4(b). We observe from Fig 7.4(a) that the stability

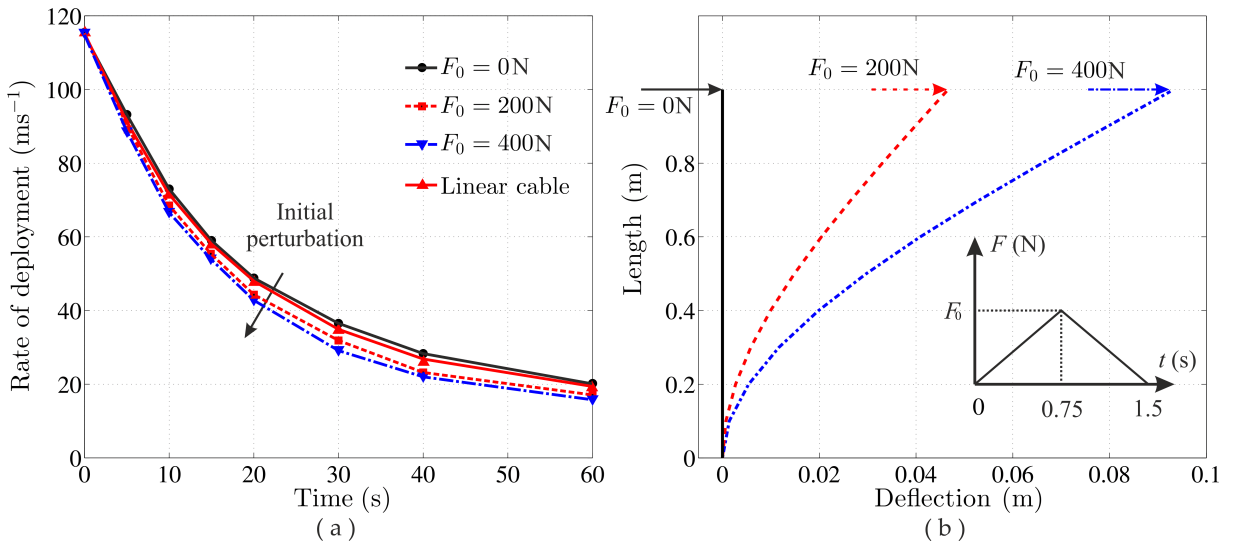


Fig. 7.4: (color online)(a) Modified deployment chart for inextensible GE cables, subjected to initial perturbations F_0 , (b) perturbed profile of the cable after applying F_0 at the end, (b)(inset) variation of perturbation with time.

limits for an unperturbed, inextensible GE cable is similar to that of a linear cable (as in Fig 7.3(a)). We see that a GE cable becomes unstable earlier as F_0 increases. In the other hand, if we set v to be low, i.e $v \leq 20 \text{ ms}^{-1}$, the stability limits for $F_0 = 200 \text{ N}$ and $F_0 = 400 \text{ N}$ remains the same. Therefore, if the rate of deployment is kept less than 20 ms^{-1} , the adverse effect of large perturbations on the cable may be avoided. However, even if the cable remains stable, large perturbations give rise to high amplitude oscillations of the cable, as shown in Fig 7.1(a) and Fig 7.1(c). Thus, material damping of the cable must play a crucial role in damping out this high amplitude oscillations. Damped vibrations of lengthening/shortening cables are not investigated in the current work. Next, we investigate the effect of air flow on the dynamics of the GE cable. We consider the cable, to be lengthening in a steady air flow and develop deployment charts for this case.

7.5 Effect of air flow on lengthening cables

We consider the effect of air flow on the aerostat only, as considered for a linear cable in [Chapter 4](#). The model of aerodynamic forces on the aerostat is taken to be same as [Chapter 4](#). In the computations, we take $\rho_{\text{air}} = 1.12 \text{ Kg m}^{-3}$ and radius of the spherical aerostat as $r = 1 \text{ m}$. We consider the atmospheric velocity profile as shown in [Fig 7.5\(a\)](#). This air flow profile is taken from ([Teixeira et al., 2008](#), Fig. 2). We see in [Fig 7.5\(b\)](#) that the cable oscillates about a shifted

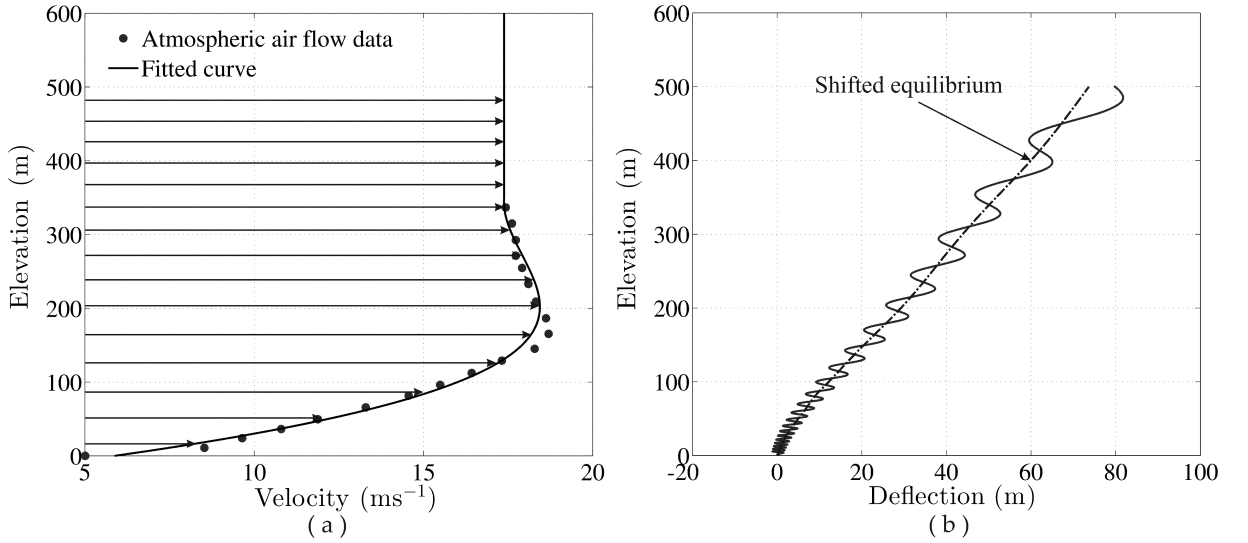


Fig. 7.5: (a) Atmospheric air flow data obtained from along with the curve fitted to it, (b) End trajectory of a lengthening cable, subjected to aerodynamic loading.

equilibrium position — determined by the air flow profile and the volume of the aerostat. The oscillation trajectory, shown in [Fig 7.5\(b\)](#) is qualitatively similar to, where we investigated a linear cable model. We also note that the shifted equilibrium keeps on shifting with elevation, even after the air flow profile becomes uniform. This is due to the aerostat's inertia, for which it keeps on deflecting.

We now analyse stability of the GE cable, subjected to aerodynamic forces. We first consider an air flow profile as [Fig 7.5\(a\)](#). Thus, the deployment chart gets modified as shown in [Fig 7.6](#). We note that given a constant rate of deployment, if the cable is subjected to aerodynamic forces due to subtle air flow like [Fig 7.5\(a\)](#), then it remains stable for a relatively longer period of time. Thus, it can be inferred from [Fig 7.6](#) that, the steady air flow is resulting a constraint motion of the cable. Eventually, this constraint motion is more stable than the free oscillations of the cable.

However, the airflow profile as shown in [Fig 7.5\(a\)](#) does not remain smooth in practice. We now consider perturbations to this basic airflow profile [Fig 7.5\(a\)](#) and investigate the stability of the system. We perturb the basic airflow profile u_0 as

$$u_0^* = u_0 + A_0 u_0 \sin(0.01z), \quad (7.4)$$

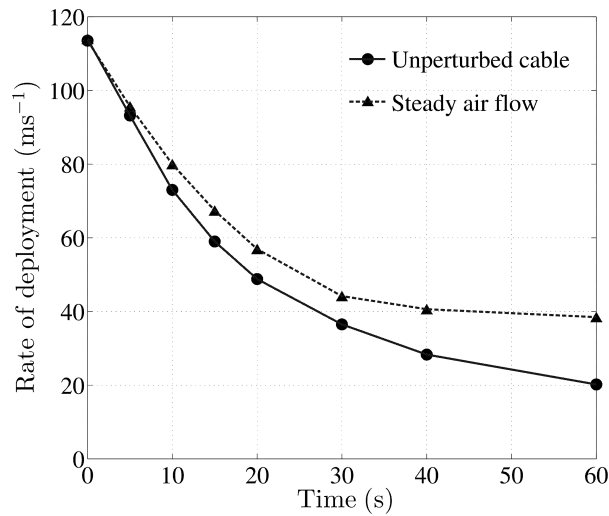


Fig. 7.6: Modified deployment chart for cables, subjected to steady air flow Fig 7.5(a)

where z is the elevation and A_0 is the amplitude of perturbation. The unperturbed and sinusoidally perturbed air flow fields are shown in Fig 7.7(a). We observe from Fig 7.7(b) that with

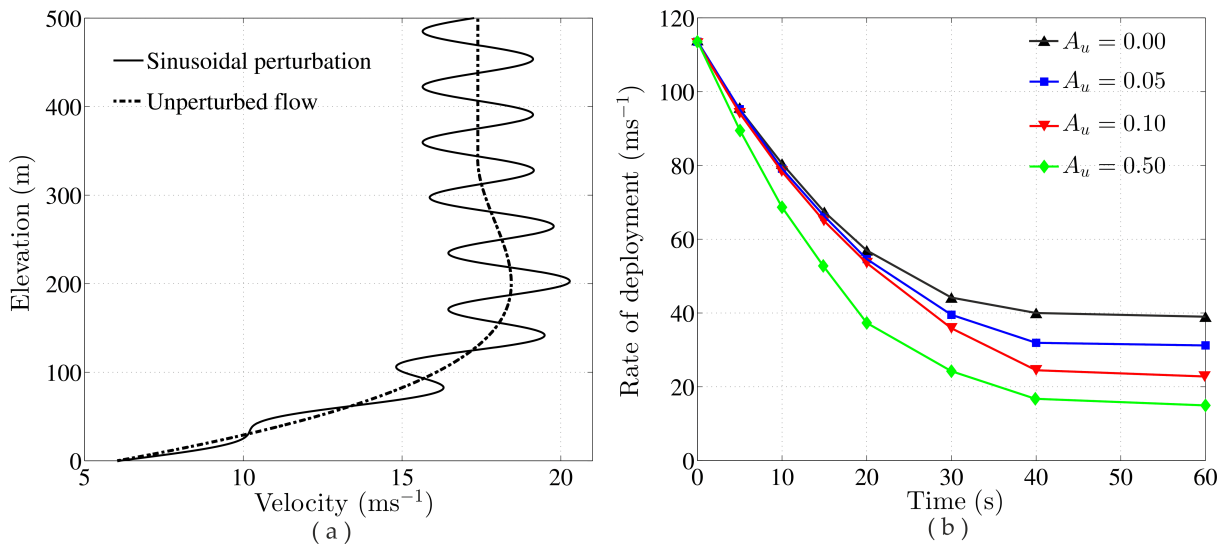


Fig. 7.7: (color online)(a) Unperturbed air flow profile along with the perturbed profile (7.4), (b) modified deployment chart for various A_0 .

increasing A_0 , the cable becomes more susceptible to instabilities. Thus, it can be inferred that, irregularity in the flow results the cable to become unstable earlier than the predicted critical time considering unperturbed flow. These high-amplitude perturbations are often strong enough to let any configuration to go unstable in the course of deployment. Once a configuration becomes *locally* unstable, eventually leads to instability.

Random perturbations with sudden jumps in the flow is not considered in our numerical investigations. This is due to the fact that, such perturbations and sudden jumps in the flow give rise to convergence issues. However, the sinusoidal perturbation, shown in Fig 7.7(a), helps us to

capture the response of the system under random perturbation. We now investigate the stability of shortening cables in light of *local* stability analysis — discussed in [Sec. 7.2](#).

7.6 Summary

In this chapter stability of lengthening GE cables are investigated in detail. We first defined our notion of *local* instability of a configuration. Effects of extensibility of the cable and initial perturbations were then investigated in detail. Effect of aerodynamic forces on stability were also analysed.

Chapter 8

Base excitation of Lengthening/Shortening GE Cables

8.1 Introduction

Aerostats are deployed from a platform, usually placed on the ground. As no foundation is absolutely rigid in practice we now investigate the dynamics of lengthening/shortening GE cables in presence of a non-rigid deployment platform. We investigate periodic transverse oscillations of the platform. Such oscillations may make the cable resonate, as shown by [González-Cruz et al. \(2016\)](#). We first investigate the frequency domain responses of lengthening/shortening GE cables, followed by a semi-analytical investigation of resonance in such cable. This semi-analytical investigation is accomplished by considering the rotations of the sections to be small, followed by obtaining a reduced-order model of the system by Galerkin projection; see [Hagedorn and Dasgupta \(2007, p. 47-49\)](#). We conclude by providing the frequency domain response of lengthening/shortening cables in light of temporal evolution of the natural frequencies of the reduced-order model.

8.2 Modified of equations of motion

We consider the cable is subjected to periodic base excitation $r(\bar{t}) = R_0 \sin(\omega_0 \bar{t})$ in the transverse direction; see [Fig. 8.1](#). We observe from [Fig. 8.1](#) that the kinematic variables, as introduced in [Chapter 4](#), are now expressed in terms of coordinate system \mathbf{E} , which is attached to the moving platform. Thus, the equations of motion, which was derived by considering \mathbf{E} to be an inertial frame, need to be modified. We consider \tilde{u}_2^* to be $\tilde{u}_2^* = \tilde{u}_2^{**} - r(\bar{t})$, where \tilde{u}_2^{**} is displacement in

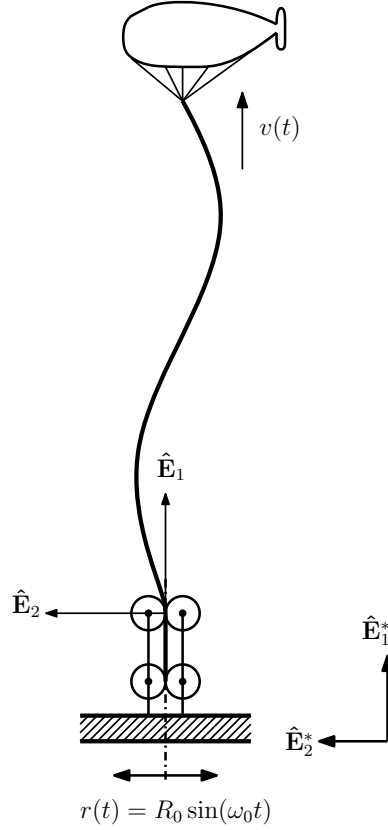


Fig. 8.1: Schematic of a lengthening/shortening cable, subjected to base excitation in the transverse direction.

$\hat{\mathbf{E}}_2^*$ direction, measured in the inertial coordinate frame \mathbf{E}^* . We now express (5.32) in *base-fixed* coordinate system \mathbf{E} as

$$\begin{aligned} & \tilde{\gamma} \left[\frac{\partial}{\partial \xi} \left\{ (1 - \xi)^2 \frac{\partial \tilde{u}_1^*}{\partial \xi} \right\} i^2 + 2 \frac{\partial^2 \tilde{u}_1^*}{\partial \xi \partial \bar{t}} (1 - \xi) \dot{l} + \frac{\partial \tilde{u}_1^*}{\partial \xi} (1 - \xi) \ddot{l} \right. \\ & \quad \left. + \frac{\partial^2 \tilde{u}_1^*}{\partial \bar{t}^2} l^2 + \ddot{l}^2 \right] = \frac{\partial \tilde{f}_1^*}{\partial \xi} L + \tilde{F}_1^* l^2, \\ & \tilde{\gamma} \left[\frac{\partial}{\partial \xi} \left\{ (1 - \xi)^2 \frac{\partial}{\partial \xi} (\tilde{u}_2^{**} + r(\bar{t})) \right\} i^2 + 2 \frac{\partial^2}{\partial \xi \partial \bar{t}} (\tilde{u}_2^{**} + r(\bar{t})) (1 - \xi) \dot{l} \right. \\ & \quad \left. + \frac{\partial}{\partial \xi} (\tilde{u}_2^{**} + r(\bar{t})) (1 - \zeta) \ddot{l} + \frac{\partial^2}{\partial \bar{t}^2} (\tilde{u}_2^{**} + r(\bar{t})) l^2 \right] = \frac{\partial \tilde{f}_2^*}{\partial \zeta} l + \tilde{F}_2^* l^2, \end{aligned} \quad (8.1)$$

and

$$\begin{aligned} & \frac{\partial}{\partial \zeta} \left\{ (1 - \zeta)^2 \frac{\partial \tilde{\theta}^*}{\partial \zeta} \right\} i^2 + 2 \frac{\partial^2 \tilde{\theta}^*}{\partial \zeta \partial \bar{t}} (1 - \zeta) \dot{l} + \frac{\partial \tilde{\theta}_2^*}{\partial \zeta} (1 - \zeta) \ddot{l} \\ & \quad + \frac{\partial^2 \tilde{\theta}^*}{\partial \bar{t}^2} l^2 = \frac{\partial \tilde{m}^*}{\partial \zeta} l + l \left\{ \frac{\partial \tilde{\mathbf{r}}_0^*}{\partial \zeta} \times \tilde{\mathbf{f}}^* \right\} \cdot \mathbf{E}_3 + \tilde{M}^* l^2. \end{aligned}$$

We note that in the above equation, r is only a function of time. This enables us to modify (8.1) further and express it as

$$\begin{aligned} & \tilde{\gamma} \left[\frac{\partial}{\partial \zeta} \left\{ (1-\zeta)^2 \frac{\partial \tilde{u}_1^*}{\partial \zeta} \right\} \dot{l}^2 + 2 \frac{\partial^2 \tilde{u}_1^*}{\partial \zeta \partial \bar{t}} (1-\zeta) \dot{l} + \frac{\partial \tilde{u}_1^*}{\partial \zeta} (1-\zeta) \ddot{l} \right. \\ & \quad \left. + \frac{\partial^2 \tilde{u}_1^*}{\partial \bar{t}^2} l^2 + \ddot{l}^2 \right] = \frac{\partial \tilde{f}_1^*}{\partial \zeta} l + \tilde{F}_1^* l^2, \\ & \tilde{\gamma} \left[\frac{\partial}{\partial \zeta} \left\{ (1-\zeta)^2 \frac{\partial}{\partial \zeta} (\tilde{u}_2^{**}) \right\} \dot{l}^2 + 2 \frac{\partial^2}{\partial \zeta \partial \bar{t}} (\tilde{u}_2^{**}) (1-\zeta) \dot{l} \right. \\ & \quad \left. + \frac{\partial}{\partial \zeta} (\tilde{u}_2^{**}) (1-\zeta) \ddot{l} + \frac{\partial^2}{\partial \bar{t}^2} (\tilde{u}_2^{**}) l^2 \right] = -\tilde{\gamma} l^2 \ddot{r}(t) + \frac{\partial \tilde{f}_2^*}{\partial \zeta} l + \tilde{F}_2^* l^2, \end{aligned} \quad (8.2)$$

and

$$\begin{aligned} & \frac{\partial}{\partial \zeta} \left\{ (1-\zeta)^2 \frac{\partial \tilde{\theta}^*}{\partial \zeta} \right\} \dot{l}^2 + 2 \frac{\partial^2 \tilde{\theta}^*}{\partial \zeta \partial \bar{t}} (1-\zeta) \dot{l} + \frac{\partial \tilde{\theta}_2^*}{\partial \zeta} (1-\zeta) \ddot{l} \\ & \quad + \frac{\partial^2 \tilde{\theta}^*}{\partial \bar{t}^2} l^2 = \frac{\partial \tilde{m}^*}{\partial \zeta} l + l \left\{ \frac{\partial \tilde{\mathbf{r}}_0^*}{\partial \zeta} \times \tilde{\mathbf{f}}^* \right\} \cdot \mathbf{E}_3 + \tilde{M}^* l^2. \end{aligned}$$

Thus, we obtain modified form of in the non-inertial coordinate frame \mathbf{E} . We see that in the frame \mathbf{E} , the boundary conditions remain the same. Thus, no modification is done in the boundary conditions of the system. We now present computationally obtained frequency domain response of lengthening/shortening GE cables.

8.3 Frequency domain response of lengthening cables

Frequency domain response of lengthening GE cables are shown in Fig. 8.2. We consider the

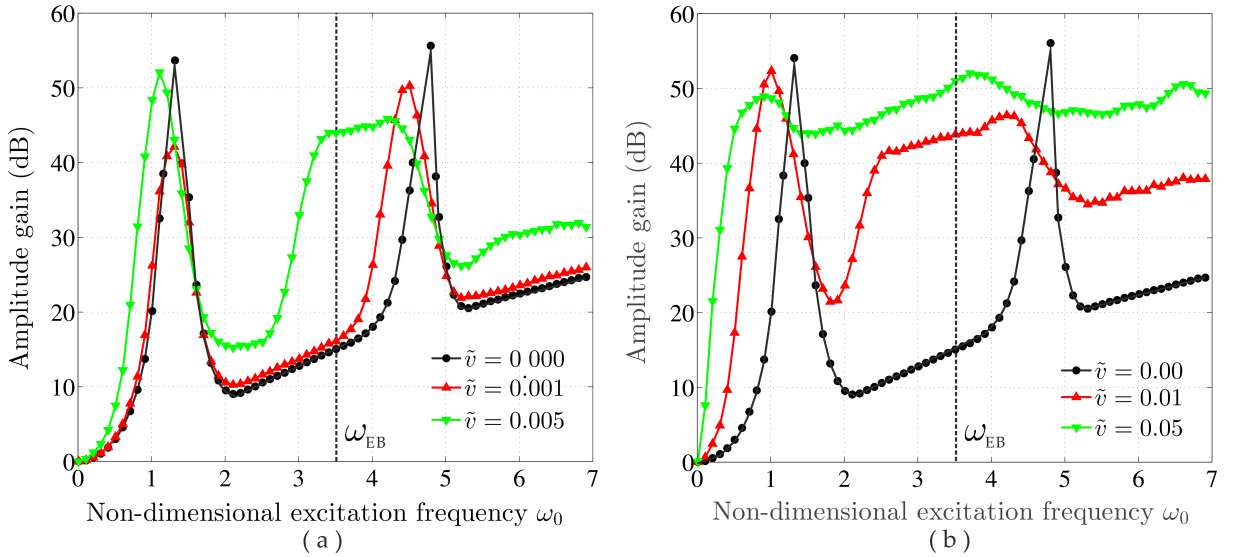


Fig. 8.2: (color online) Frequency domain response of lengthening cables for different rates of lengthening \tilde{v} .

cable to be inextensible, i.e $E^* = 10^5$. We take bending stiffness of the cable to be $EI = 1000\text{Nrad}^{-1}$ and perform computations upto $\bar{t} = 100$. We define amplitude gain in decibel as

$$\text{Amplitude gain} = 20 \log[\max(A_{\text{end}})/\max(A_{\text{end}})|_{\omega_0=0.01}], \quad (8.3)$$

where the maximum end deflection amplitude A_{end} is normalized by A_{end} for $\omega_0 = 0.01$. Thus, we always obtain amplitude gain near $\omega_0 = 0$ as unity.

We see in Fig. 8.2(a) and (b) that there are two frequencies between $0 \leq \omega_0 \leq 7$, where a GE cable of constant length $L_0 = 1$ resonates. We also observe that the second resonant frequency is slightly higher than the first natural frequency of an Euler-Bernoulli (EB) beam. This motivates us to investigate the first resonance, which apparently looks like a *subharmonic resonance* at nearly equal to $1/3^{\text{rd}}$ of the second peak. This investigation is accomplished by considering the GE cable to be a free cantilever beam, having high bending stiffness. This assumption enables us to perform asymptotic approximations by considering the rotation θ to be small.

Another feature we note from Fig. 8.2(a) and (b) that with the deployment rate \tilde{v} , the first and second resonance bandwidths increase and eventually, the cable starts resonating at a lower ω_0 . Finally, we observe from Fig. 8.2(b) that for $\tilde{v} = 0.05$ the cable resonates for all values of $\omega_0 > 0.5$. We investigate this phenomena through a reduced-order model in the next section.

8.4 Reduced-order models

In this section, we first develop a reduced-order model of a GE cable of constant length, followed by reduced-order model of lengthening/shortening GE cables.

8.4.1 Cable of constant length

We now develop a reduced order model of a cable of constant length $L = L_0$. We see that if the ratio E^* is of $O(1)$, we expect the rotations of a section to be small. We now express the rotation of sections θ^* as $\theta^* = \theta_0^* + \epsilon\bar{\theta}$, where $0 < \epsilon \ll 1$. We take the base state θ_0^* of oscillations as the trivial equilibrium position $\theta_0^* = 0$. We now retain terms upto $O(\epsilon)$ and express $\mathbf{\Lambda}$ as

$$\mathbf{\Lambda} = \begin{bmatrix} 1 & -\epsilon\bar{\theta} \\ \epsilon\bar{\theta} & 1 \end{bmatrix}.$$

We now set the length of the cable to be unity and take $\gamma = 1$. We also set all external forces to be zero, so that (8.2) can now be expressed as

$$\begin{aligned}\frac{\partial^2 \tilde{u}_1^*}{\partial \bar{t}^2} &= \frac{\partial \tilde{f}_1^*}{\partial \zeta}, \\ \frac{\partial^2 \tilde{u}_2^*}{\partial \bar{t}^2} &= \frac{\partial \tilde{f}_2^*}{\partial \zeta}\end{aligned}\quad (8.4)$$

and

$$\frac{\partial^2 \tilde{\theta}^*}{\partial \bar{t}^2} = \frac{\partial \tilde{m}^*}{\partial \zeta} + \left\{ \frac{\partial \tilde{\mathbf{r}}_0^*}{\partial \zeta} \times \tilde{\mathbf{f}}^* \right\} \cdot \mathbf{E}_3.$$

In order to obtain a reduced-order model, we consider \tilde{u}_1^* , \tilde{u}_2^* and $\tilde{\theta}^*$ as the following

$$\begin{aligned}\tilde{u}_1^* &= u_1^{(0)}(t) \sin\left(\frac{\pi}{2}\zeta\right), \\ \tilde{u}_2^* &= u_2^{(0)}(t) \sin\left(\frac{\pi}{2}\zeta\right)\end{aligned}\quad (8.5)$$

and

$$\bar{\theta} = \theta^{(0)}(t) \sin\left(\frac{\pi}{2}\zeta\right),$$

where the shape functions are taken to be $\sin(\pi\zeta/2)$, which satisfies the geometric boundary conditions. We now substitute (8.5) into (8.4), followed by a Galerkin projection (Hagedorn and Dasgupta, 2007, p. 47-49). This enables us to obtain a single-mode approximation of (8.4) as a set of ordinary differential equations as

$$\begin{aligned}\ddot{u}_1^{(0)} + \frac{\pi^2}{4} E^* u_1^{(0)} \left(1 + \frac{1}{4} \epsilon^2 (\theta^{(0)})^2 \right) &= 0, \\ \ddot{u}_2^{(0)} + \frac{\pi^2}{4} E^* u_2^{(0)} \left(1 + \frac{1}{4} \epsilon^2 (\theta^{(0)})^2 \right) + E^* \left(\epsilon \theta^{(0)} + \frac{3}{2} \epsilon^3 (\theta^{(0)})^3 \right) &= 0 \\ \text{and } \ddot{\theta}^{(0)} + \epsilon \frac{\pi^2}{4} \theta^{(0)} + E^* \left(\epsilon \theta^{(0)} + \frac{3}{4} \epsilon^3 (\theta^{(0)})^3 \right) + E^* u_1^{(0)} \left(\frac{1}{3} \epsilon \theta^{(0)} + \frac{1}{5} \epsilon^3 (\theta^{(0)})^3 \right) &= 0 \\ -E^* u_2^{(0)} \left(1 + \frac{1}{2} \epsilon^2 (\theta^{(0)})^2 \right) &= 0.\end{aligned}\quad (8.6)$$

We now retain upto $O(\epsilon)$ terms in the above and express it as

$$\begin{aligned}\ddot{u}_1^{(0)} + \frac{\pi^2}{4} E^* u_1^{(0)} &= 0, \\ \ddot{u}_2^{(0)} + \frac{\pi^2}{4} E^* u_2^{(0)} + E^* \epsilon \theta^{(0)} &= 0 \\ \text{and } \ddot{\theta}^{(0)} + \epsilon \frac{\pi^2}{4} \theta^{(0)} + E^* \epsilon \theta^{(0)} + E^* u_1^{(0)} \frac{2}{3} \epsilon \theta^{(0)} - E^* u_2^{(0)} \epsilon \theta^{(0)} &= 0.\end{aligned}\quad (8.7)$$

We see that evolution of $u_1^{(0)}$ has a very little contribution in transverse dynamics of the cable. Hence we drop the first equation of (8.7) and express it as

$$\ddot{u}_2^{(0)} + \frac{\pi^2}{4} E^* u_2^{(0)} + E^* \epsilon \theta^{(0)} = 0 \quad (8.8)$$

and

$$\ddot{\theta}^{(0)} + \epsilon \frac{\pi^2}{4} \theta^{(0)} + E^* \epsilon \theta^{(0)} - E^* u_2^{(0)} = 0.$$

The above equation is the reduced-order model of (8.5), we obtain through a single-mode approximation of a cantilever GE cable. We see that (8.8) are a set of two simultaneous ordinary differential equations in $u_2^{(0)}$ and $\theta^{(0)}$. Thus the reduced-order system has two natural frequencies, namely $\omega_{GE}^{(1)}$ and $\omega_{GE}^{(2)}$. Variation of the natural frequencies with ϵ is shown in Fig. 8.3. We

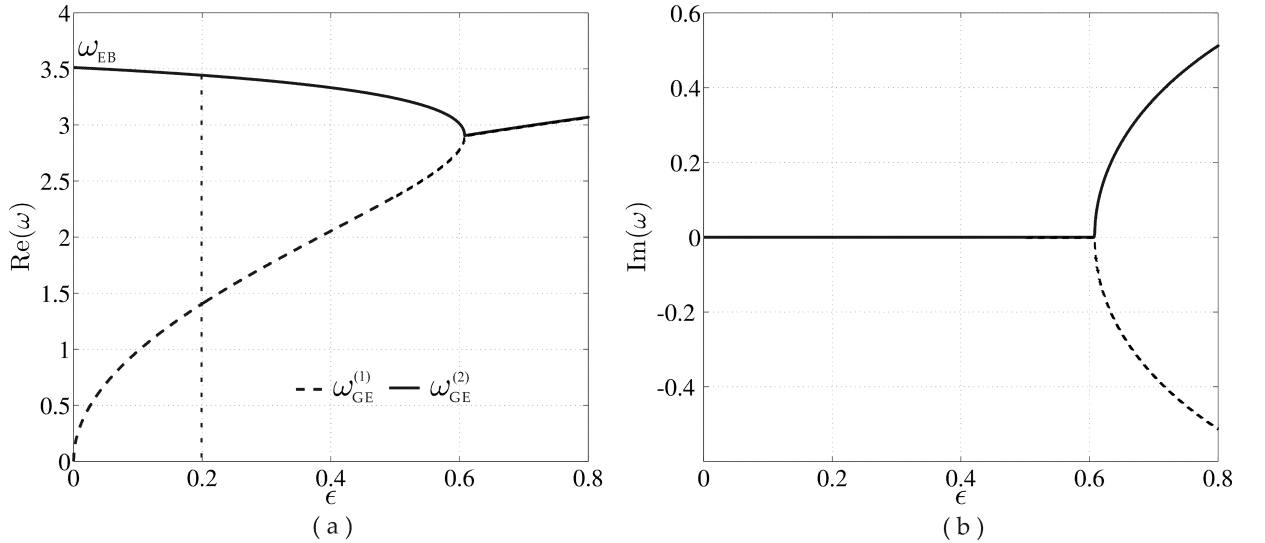


Fig. 8.3: Variation of natural frequencies of (8.8) with ϵ , (a) real parts of natural frequencies, (b) imaginary parts of natural frequencies.

observe from Fig. 8.3(a) that at $\epsilon = 0$, the system have only one natural frequency. It is also noted from (8.8) that, at $\epsilon = 0$ first equation of (8.8) becomes independent of the rotational degree of freedom $\theta^{(0)}$. Thus, we obtain a single natural frequency of transverse oscillations $u_2^{(0)}$. This is the limiting condition, where a GE cable behaves like an EB beam, in which, only transverse degree of freedom is considered. Two natural frequencies (8.8) are obtained for $0 < \epsilon \ll 1$. This indicates coupling between the transverse and rotational degrees-of-freedom. We note from Fig. 8.3(a) that $\omega_{GE}^{(2)} \approx \omega_{EB}$ for $0 < \epsilon \ll 1$. Thus, it can be concluded that, GEBT can capture the *sub-frequency* resonance of highly stiff cantilever beams. Experimental investigations, done by González-Cruz et al. (2016), also show *sub-frequency* resonance of cantilevers, which cannot be captured by EB beam model. Finally, for $\epsilon > 0.6$, both the natural frequencies $\omega_{GE}^{(1)}$ and $\omega_{GE}^{(2)}$ become complex; see Fig. 8.3(b). It demonstrates the failure of asymptotic approximation for $\epsilon > 0.6$.

We select the stiffness ratio E^* to be 5, which enables us to obtain the first natural frequency of an equivalent EB beam from (8.8) for $\epsilon = 0$. The approximation (8.8) holds good near $\epsilon \approx 0.2$, as shown in Fig. 8.4, where we compare the frequency domain response of the single-mode approximation (8.8) with computation. We now investigate the range of E^* , in which the ap-

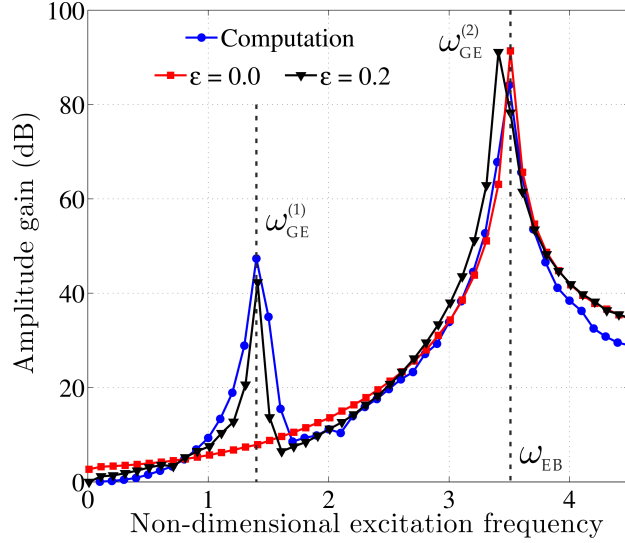


Fig. 8.4: (color online) Comparison of computationally obtained frequency domain response of the system with that of the reduced order model.

proximation holds good. We note that E^* is the non-dimensional ratio of axial stiffness to the bending stiffness. Thus, given a constant axial stiffness, a greater value of E^* refers to a highly flexible beam. Therefore, we expect the small rotation approximation to fail for higher values of E^* . In Fig. 8.5, we compare $\omega_{GE}^{(2)}$ with the computed one for various E^* . We see in Fig. 8.5 that, the approximation holds good for $E^* \leq 5.2$. In the next section we will investigate base

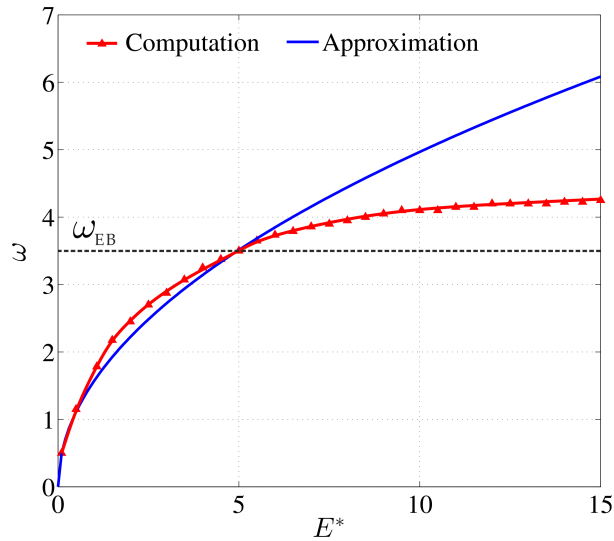


Fig. 8.5: (color online) Comparison of computed second resonant frequency of the system with the second natural frequency of the reduced order model for $\epsilon = 0$, with stiffness ratio E^* .

excitations of lengthening/shortening cables. We will proceed in a similar manner to obtain the reduced-order model of a lengthening cable.

8.4.2 Lengthening/shortening at constant rate

We now investigate a reduced-order model for lengthening/shortening cables in the limit of rotation of the sections to be small. Proceeding in a similar manner as the previous section leads to

$$l^2 \ddot{u}_2^{(0)} + \tilde{v} l \dot{u}_2^{(0)} + \frac{\pi^2}{4} l E^* u_2^{(0)} + E^* l \epsilon \theta^{(0)} - \tilde{v}^2 \left(\frac{1}{2} + \frac{\pi^2}{12} \right) u_2^{(0)} = 0 \quad (8.9)$$

and

$$l^2 \ddot{\theta}^{(0)} + \tilde{v} l \dot{\theta}^{(0)} + \epsilon \frac{\pi^2}{4} \theta^{(0)} + E^* l \epsilon \theta^{(0)} - \tilde{v}^2 \left(\frac{1}{2} + \frac{\pi^2}{12} \right) \theta^{(0)} - E^* l u_2^{(0)} = 0,$$

where l is the length of the cable and \tilde{v} is its rate of lengthening/shortening. The above equation is the reduced order model of (8.2). We now evaluate temporal evolutions of two natural frequencies of (8.9), i.e, $\omega_{\text{GE}}^{(1)}$ and $\omega_{\text{GE}}^{(2)}$ by considering rate of lengthening/shortening to be small. This consideration enables us to assume l to be constant at a given instant of time \bar{t} and evaluate $\omega_{\text{GE}}^{(1)}$ and $\omega_{\text{GE}}^{(2)}$ at \bar{t} . Thus, we obtain temporal evolutions of $\omega_{\text{GE}}^{(1)}$ and $\omega_{\text{GE}}^{(2)}$ for a constant rate of lengthening $\tilde{v} = 0.005$, as depicted in Fig. 8.6(a). We observe from Fig. 8.6(a) that $\omega_{\text{GE}}^{(1)}$ and $\omega_{\text{GE}}^{(2)}$ are decreasing with time. This is similar to the temporal evolution of the first natural frequency, obtained from a linear cable model in Figs. 3.2(a) and (b) of Chapter 3.

We now investigate the frequency domain response of the cable, lengthening at $\tilde{v} = 0.005$; see Fig. 8.6(b). We take deployment time to be $\bar{t} = 100$ and then calculate amplitude gain as defined in (8.3). We note from Fig. 8.6(b) that instead of resonating at some particular frequencies, the cable resonates at certain ranges of excitation frequencies. We define this frequency ranges as *resonance bands*. Resonating at certain bands of frequencies may be explained in light of temporal evolutions of $\omega_{\text{GE}}^{(1)}$ and $\omega_{\text{GE}}^{(2)}$.

We first choose a time duration \bar{t}^* (say 100) of deployment. We note from Fig. 8.6(a) that at $\bar{t} = \bar{t}^*$, the first natural frequency of the cable becomes ω_1^* , at which it starts resonating. We see that, for excitation frequency $\omega_0 > \omega_1^*$, the cable starts resonating at $\bar{t} < \bar{t}^*$ and continues exhibiting high amplitude oscillations upto $\bar{t} = \bar{t}^*$. This phenomena continues till $\omega_0 \leq \omega_1^0$, which is the first natural frequency of the cable, which is kept at its initial length. Thus, given the duration of deployment \bar{t}^* , the cable resonates for all $\omega_1^* \leq \omega_0 \leq \omega_1^0$. We define this range as the first resonance band $\Delta\omega_1 = \omega_1^0 - \omega_1^*$. Similarly, the second resonance band $\Delta\omega_2$ can be defined as the range of excitation frequencies, at which the second resonance takes place; see Fig. 8.6(b). We also show resonance bands $\Delta\omega_1$ and $\Delta\omega_2$ in the computed frequency domain response Fig. 8.6(b). We obtain a good match in the computed and approximated resonance

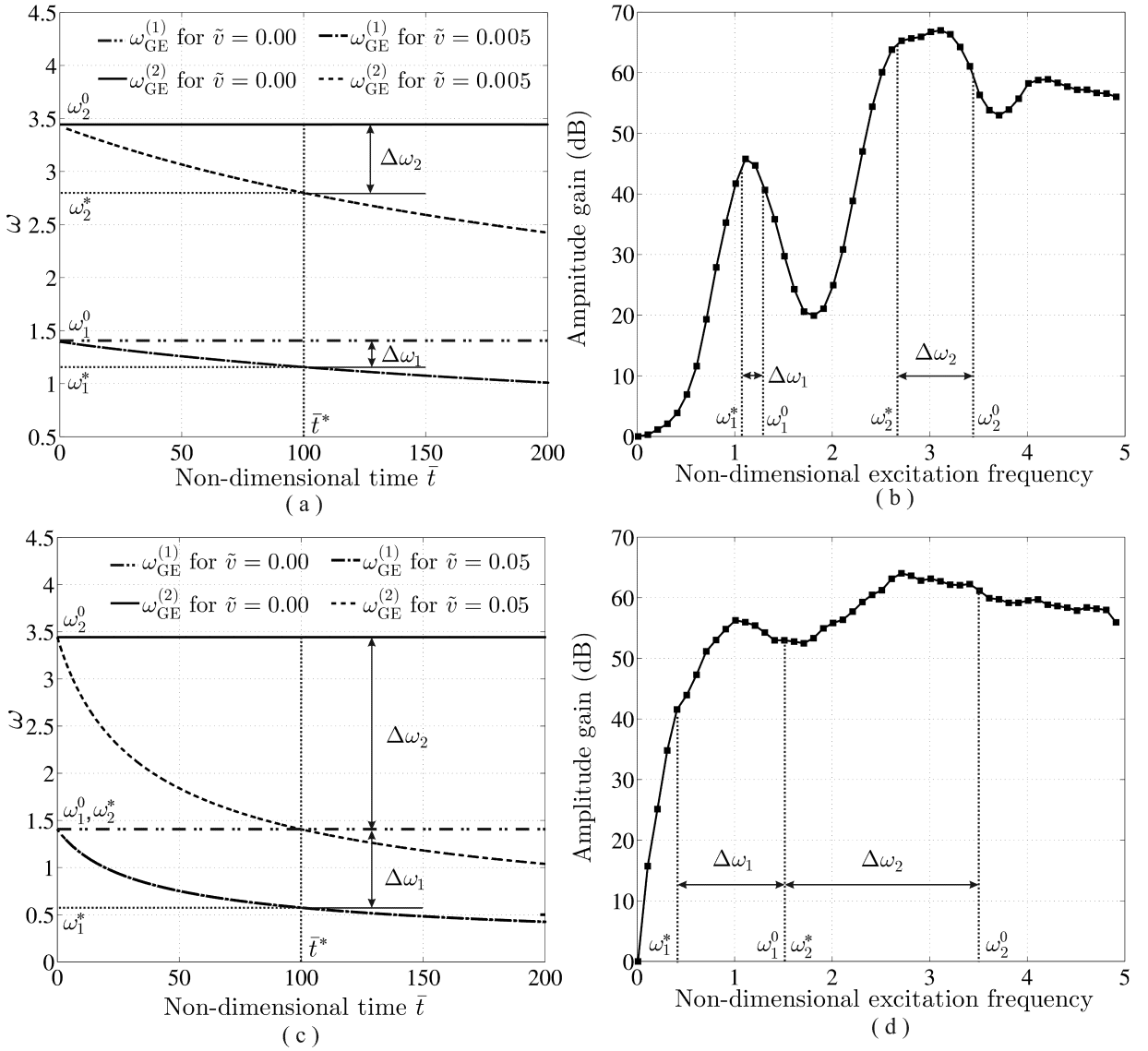


Fig. 8.6: (a) Evolution of $\omega_{GE}^{(1)}$ and $\omega_{GE}^{(2)}$ with time, (b) computed frequency domain response of a cable, lengthening at a rate of $\tilde{v} = 0.005$ upto $\bar{t} = 100$. (c) Evolution of $\omega_{GE}^{(1)}$ and $\omega_{GE}^{(2)}$ with time, (d) computed frequency domain response of a cable, lengthening at a rate of $\tilde{v} = 0.05$ upto $\bar{t} = 100$

bands.

Width of these resonance bands $\Delta\omega_1$ and $\Delta\omega_2$ depend on both the rate and duration of deployment. It is observed from Fig. 8.6(a) that if the cable is extended for a longer duration say $\bar{t} = 150$, then both $\Delta\omega_1$ and $\Delta\omega_2$ will increase and eventually, will overlap.

Broadening and overlapping of resonance bands at a relatively low \bar{t} is seen for a greater rate of deployment. As shown in Fig. 8.6(c), given the same duration of deployment $\bar{t} = 100$, $\Delta\omega_1$ and $\Delta\omega_2$ increase for a greater $\tilde{v} = 0.05$. This shows a limiting case where $\Delta\omega_1$ and $\Delta\omega_2$ just touches each other. We also note that the first and second resonance bands overlap for $\bar{t} > \bar{t}^*$. This is also reflected in the computed frequency domain response, as shown in Fig. 8.6(d), in

which we see that the cable resonates at any $\omega_0 \geq \omega_1^*$. We also note from Fig. 8.6(d) that the cable resonates even after $\omega_0 > \omega_2^0$. This may happen due to overlapping of the next higher resonance band with $\Delta\omega_2$. Natural frequencies of the cable greater than $\omega_{GE}^{(2)}$ cannot be obtained from the reduced order model (8.9). However, approximations of resonance bands upto $\omega_0 \leq \omega_2^0$ is obtained satisfactorily.

We now investigate frequency domain response of shortening cables. We first plot in Fig. 8.7(a)

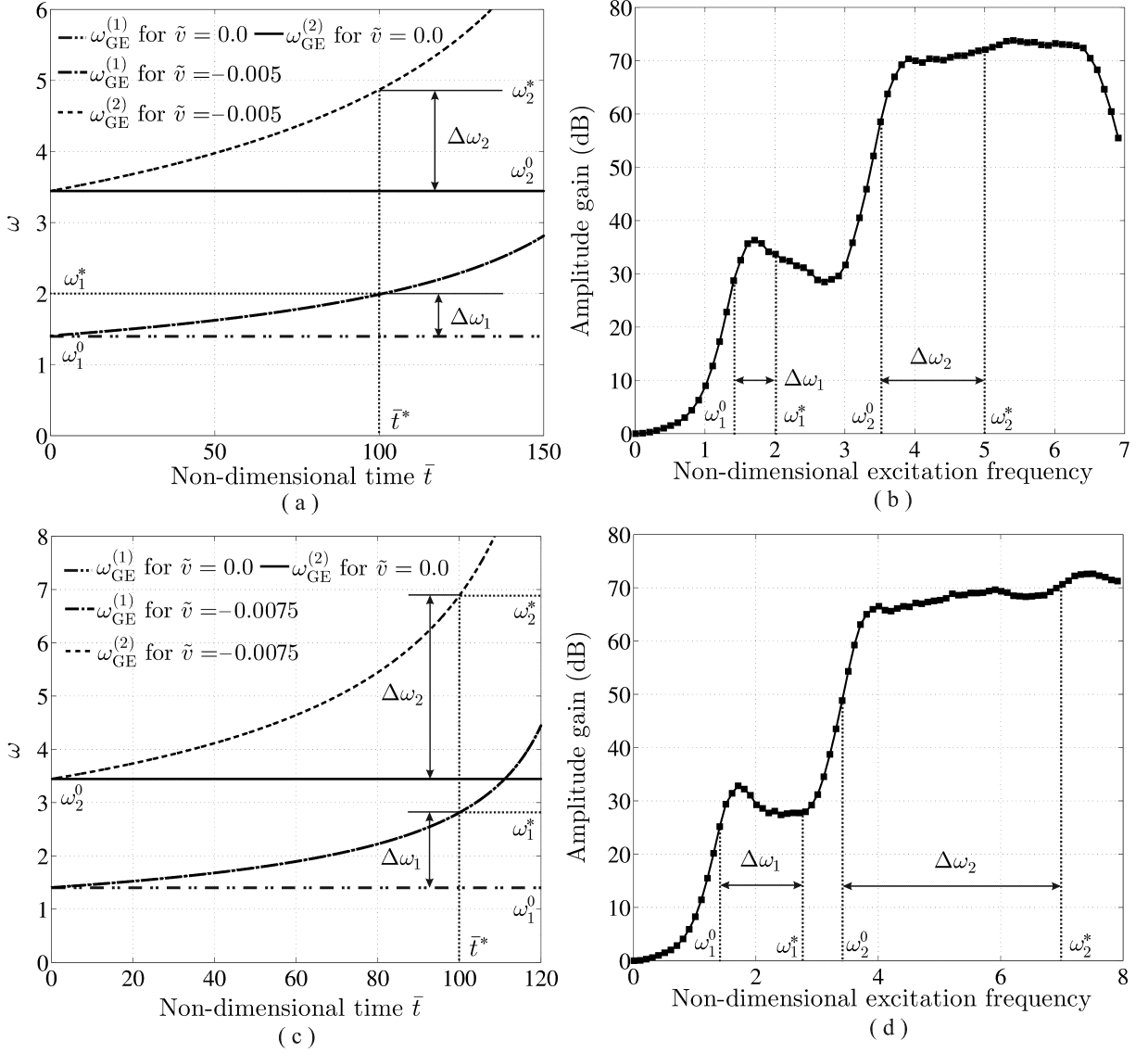


Fig. 8.7: (a) Evolution of $\omega_{GE}^{(1)}$ and $\omega_{GE}^{(2)}$ with time, (b) computed frequency domain response of a cable, shortening at a rate of $\tilde{v} = 0.005$ upto $\bar{t} = 100$. (c) Evolution of $\omega_{GE}^{(1)}$ and $\omega_{GE}^{(2)}$ with time, (d) computed frequency domain response of a cable, shortening at a rate of $\tilde{v} = 0.0075$ upto $\bar{t} = 100$

the temporal evolutions of $\omega_{GE}^{(1)}$ and $\omega_{GE}^{(2)}$ for shortening at a rate of $\tilde{v} = 0.005$. As seen for the linear cable model in Figs. 3.1(b) and (c) of Chapter 3, here also natural frequencies increase with time and eventually blows up to infinity for $l \rightarrow 0$.

Here we see that the cable starts resonating at $\omega_0 \geq \omega_1^0$ and continues to resonate upto $\omega_0 = \omega_1^*$, which is the first natural frequency of the cable at $\bar{t} = \bar{t}^*$. This is unlike a lengthening cable, where resonance starts at ω_1^* and continues upto ω_1^0 . Here we define resonance band width as $\Delta\omega_1 = \omega_1^* - \omega_1^0$. Similarly, the second resonance band is defined as $\Delta\omega_2 = \omega_2^* - \omega_2^0$.

We now observe from Fig. 8.7(b) that the approximations for resonance bands $\Delta\omega_1$ and $\Delta\omega_2$ holds good. However, we see the cable to continue resonating for $\omega_0 > \omega_1^2$ upto $\omega_0 \approx 6.5$. This is due to overlapping of the second band $\Delta\omega_2$ with the third resonance band, which the reduced-order model (8.9) fails to capture.

Width of the resonance bands $\Delta\omega_1$ and $\Delta\omega_2$ are seen to increase for a greater rate of shortening ($\tilde{\nu} = 0.0075$) in Fig. 8.7(c). This is also reflected in the computed frequency domain response in Fig. 8.7(d), where we see $\Delta\omega_1$ and $\Delta\omega_2$ to become broad. Here also, we see the cable to continue resonating at $\omega_0 > \omega_2^*$ due to overlapping of $\Delta\omega_2$ with the next resonant band.

Thus, we see that the reduced-order model (8.9) successfully explains the broadening of first two resonance bands while lengthening/shortening and also gives (at least qualitative) explanation for broad band resonance at higher excitation frequencies while lengthening/shortening.

8.5 Summary

In this chapter the frequency domain response of lengthening/shortening GE cables is investigated in detail. Results were understood through a reduced-order model for lengthening/shortening GE cables. To this end, we first obtained and validated a reduced model of a GE cable of constant length. The model is also employed to explain the existence of a weak *sub-frequency* resonance in cantilever beams. The reduced-order model for cables of changing length was obtained in a similar manner. This model successfully explained the broad band resonance of lengthening/shortening cables, and provided physical insight in its vibrations.

Chapter 9

Concluding Remarks

In this thesis, we investigated two different models of lengthening/shortening heavy cables. First, we considered the simplest linear string model to investigate the physical problem. This is followed by investigation of the aerostat system by modeling the cable as a geometrically exact beam.

We derived equations of motion of linear elastic lengthening/shortening cables through variational principle [Chapter 2](#).

Next, in [Chapter 3](#) we presented asymptotic approximation for free vibration of slowly lengthening/shortening cables. The approximations matched well to the computed evolution of amplitude in time and also matched qualitatively with the evolutions of natural frequency and energy of the first eigenmode. Asymptotic approximations to the reduced order models of lengthening/shortening cables are not addressed in any of the existing literatures as per best of our knowledge.

In [Chapter 4](#), we presented the stability analysis of lengthening/shortening cables in light of Lyapunov's method. We considered the aerostat to be deployed at a constant rate. We developed deployment charts, based on this stability analysis. This charts readily gave the estimate for maximum achievable elevation for a given rate of deployment. Critical remarks are also made on *inherent instability* of shortening cables.

In this chapter, we also investigated the forced vibration of lengthening/shortening cables through computations. We considered the simplest model of aerodynamic force on the aerostat, which was approximated to be a rigid sphere. The frequency domain response showed the tendency of strong resonance near certain excitation frequencies. Forced vibrations and frequency domain response of lengthening/shortening cables are not addressed in any existing literature.

Finally, we concluded this part with two case studies. To investigate a more realistic case, here we considered the aerostat to be deployed with non-constant rates. Our computed results for specific cases are in a good agreement with the prescribed deployment limits, which were obtained by taking a constant rate of deployment.

Next two chapters of the thesis, i.e, [Chapter 5](#) and [Chapter 6](#) are devoted towards development of geometrically exact beam theory (GEBT) for lengthening/shortening cables and development of FE computation scheme, respectively. We followed [Vu-Quoc and Li \(1995\)](#) for derivation and also for computations. Our routine for lengthening/shortening GE cables are validated against some benchmark results, enlightened in [Simo \(1985\)](#) and [Simo and Vu-Quoc \(1986a\)](#).

Linear stability analysis of lengthening/shortening GE cables, with respect to instantaneous configurations are addressed in [Chapter 7](#). We found a good match of stability limits for GE cables with that for linear elastic cables, provided the GE cable is considered to be of high axial stiffness, i.e inextensible. It is also found from stability analysis that extensible cables become unstable earlier than the inextensible one. Next, we investigated the effect of large initial perturbations and obtained modified deployment charts for that. We also investigated the effect of aerodynamic forces on the system and on its stability. Finally, we concluded this chapter by investigating stability of shortening cables.

Lengthening/shortening GE cables, subjected to base excitations are investigated in [Chapter 8](#). Through computations, we found an additional *sub-frequency* resonance in the GE cables. This resonance is found to be near $1/3^{\text{rd}}$ of the second resonant frequency, which is commensurate to the first natural frequency of an EB beam. This is investigated further through a reduced-order model, which revealed the existence of a lower natural frequency of the system, due to an additional rotational degree-of-freedom, which is considered only in the GEBT. The broadening of resonance bandwidth with rate of deployment of lengthening/shortening cables are also investigated through a reduced-order model. We saw that reduced-order model of GE cables gave comprehensive insight to the broad-banded resonance of lengthening/shortening GE cables. Investigation of base excitation of lengthening/shortening GE cables thorough computations, followed by a reduced-order model and their comparison is not addressed in any any existing literature as per best of our knowledge.

This work may be extended further by incorporating the effect of surrounding fluid (air in this case) in a more comprehensive manner. Our routine for GE cables may be coupled with a computation routine for the surrounding fluid. However, the fluid-solid coupling may give rise to computational issues, which should be handled efficiently.

Appendix A

FE Computation and Validation for Lengthening/Shortening Linear Cables

In this section we present finite element (FE) discretization of (2.15) along with the boundary conditions (2.16) and (2.17). We express (2.15) along with the force boundary condition (2.17) in weighted residual form as

$$\begin{aligned} & \int_{\zeta_i}^{\zeta_j} \tilde{W}(\zeta) \left[lW(\zeta)\ddot{q}(\bar{t}) + 2(1-\zeta)\dot{l}W'(\zeta)\dot{q}(\bar{t}) + (1-\zeta)\ddot{l}W'(\zeta)q(\bar{t}) \right. \\ & + \left. \left\{ (1-\zeta)^2 \frac{\dot{l}^2}{l} W'(\zeta) \right\}_{,\zeta} q(\bar{t}) - \left\{ \left(\frac{1}{l} - \tilde{m} \frac{\dot{l}}{l} - \left(\frac{1}{F} + \dot{l} \right) (1-\zeta) \right) W' \right\}_{,\zeta} q(\bar{t}) \right] d\zeta \\ & + \left[\tilde{W}(\zeta) \left\{ \tilde{m}W(\zeta)\ddot{q}(\bar{t}) + \left(\frac{1}{l} - \tilde{m} \frac{\dot{l}}{l} \right) W'(\zeta)q(\bar{t}) \right\} \right]_{\zeta=1} = 0, \end{aligned}$$

where \tilde{y} is expressed in terms of spatial and temporal components as $\tilde{y} = W(\zeta)q(\bar{t})$ and $\tilde{W}(\zeta)$ is the weighting function. We now integrate the fourth and fifth term of the equation by parts

and obtain the following:

$$\begin{aligned}
& \int_{\zeta_i}^{\zeta_j} \tilde{W}(\zeta) \left[lW(\zeta)\ddot{q}(\bar{t}) + 2(1-\zeta)\dot{l}W'(\zeta)\dot{q}(\bar{t}) + (1-\zeta)\ddot{l}W'(\zeta)q(\bar{t}) \right] d\zeta - \\
& \left[\int_{\zeta_i}^{\zeta_j} (1-\zeta)^2 \frac{\dot{l}^2}{l} W' \tilde{W}'(\zeta) d\zeta \right] q(\bar{t}) + \left[\int_{\zeta_i}^{\zeta_j} \left\{ \frac{1}{l} - \tilde{m} \frac{\ddot{l}}{l} - \left(\frac{1}{\bar{F}} + \ddot{l} \right) (1-\zeta) \right\} W' \tilde{W}' d\zeta \right] q(\bar{t}) \\
& + \left[(1-\zeta)^2 \frac{\dot{l}^2}{l} W'(\zeta) \tilde{W}(\zeta) \right]_{\zeta_i}^{\zeta_j} q(\bar{t}) - \left[\left\{ \frac{1}{l} - \tilde{m} \frac{\ddot{l}}{l} - \left(\frac{1}{\bar{F}} + \ddot{l} \right) (1-\zeta) \right\} W'(\zeta) \tilde{W}(\zeta) \right]_{\zeta_i}^{\zeta_j} q(\bar{t}) \\
& + \left[\tilde{W}(\zeta) \left\{ \tilde{m} W(\zeta) \ddot{q}(\bar{t}) + \left(\frac{1}{l(\bar{t})} - \tilde{m} \frac{\ddot{l}}{l} \right) W'(\zeta) q(\bar{t}) \right\} \right]_{\zeta=1} = 0. \tag{A1}
\end{aligned}$$

We adopt Galerkin method for spatial discretization. In this method, the approximating function $W(\zeta)$ and the weighting function $\tilde{W}(\zeta)$ are taken to be same. We assume linear interpolating functions for a two noded cable element ij , and express $W(\zeta)$ and $\tilde{W}(\zeta)$ as

$$W(\zeta)q(\bar{t}) = [N_i \ N_j] [q_i(\bar{t}) \ q_j(\bar{t})]^T \quad \text{and} \quad \tilde{W}(\zeta) = [N_i \ N_j]^T.$$

where

$$N_i = 1 - \frac{\zeta - \zeta_i}{h^e} \quad \text{and} \quad N_j = \frac{\zeta - \zeta_i}{h^e},$$

for all $\zeta_i \leq \zeta \leq \zeta_j$ and $N_i = N_j = 0$, otherwise. We now express element mass, damping and stiffness matrices for an element ij in index notation as $(\alpha, \beta = 1, 2)$

$$\begin{aligned}
M_{\alpha\beta}^{(ij)} &= l \int_{\zeta_i}^{\zeta_j} N_\alpha N_\beta d\zeta \\
C_{\alpha\beta}^{(ij)} &= 2\dot{l} \int_{\zeta_i}^{\zeta_j} (1-\zeta) N'_\alpha N_\beta d\zeta \\
K_{\alpha\beta}^{(ij)} &= \ddot{l} \int_{\zeta_i}^{\zeta_j} N'_\alpha N_\beta d\zeta - \frac{\dot{l}^2}{l} \int_{\zeta_i}^{\zeta_j} (1-\zeta)^2 N'_\alpha N'_\beta d\zeta \\
&+ \int_{\zeta_i}^{\zeta_j} \left[\frac{1}{l} - \tilde{m} \frac{\ddot{l}}{l} - \left\{ \frac{1}{\bar{F}} + \ddot{l} \right\} (1-\zeta) \right] N'_\alpha N'_\beta d\zeta.
\end{aligned}$$

The above element matrices are then assembled to form the global mass, damping and stiffness matrices. Boundary terms in (A1) cancel each other at the time of assembly. Only one boundary contribution should be added to the last diagonal element of the global mass matrix as the contribution of the end mass. All other boundary terms either vanish or get cancelled at $\zeta = 1$. We now get the fundamental equation of structural dynamics as

$$\mathbf{M}(\bar{t})\ddot{\mathbf{q}}(\bar{t}) + \mathbf{C}(\bar{t})\dot{\mathbf{q}}(\bar{t}) + \mathbf{K}(\bar{t})\mathbf{q}(\bar{t}) = 0. \tag{A2}$$

The above equation is solved by explicit Newmark time marching algorithm to obtain temporal evolutions $q_i(\bar{t})$ of each nodal displacements. This equation represents a polynomial eigenvalue

problem. Eigenvalues and eigenvectors of (A2) represents the eigenfrequencies and eigenmode shapes of the cable. Stability analysis of the system, based on eigenvalues is discussed in Chapter 4.

Various physical data, taken for computations are listed in table A1.

We validate our FE computation by considering a benchmark problem of free hanging cable;

Table A1: Physical data, used in computation and approximation

Physical Data	
Density of the material (ρ in Kgm^{-3})	7800
Cross section (A in m^2)	0.00001
Net buoyancy force (F in N)	1000
End mass (m in Kg)	10

see (Hagedorn and Dasgupta, 2007, p. 19-22). Comparison of first three natural frequencies, obtained by our computation with their corresponding theoretical values are shown in table A2. The domain ζ is divided into 20 equal elements and the initial configuration of the cable is taken

Table A2: Validation of the FE solution and convergence check. The number of elements, taken in the computations is denoted by n.

	Theo.	n=5	n=10	n=20	n=50	n=100
First natural frequency (rads^{-1})	3.7585	3.7705	3.7672	3.7664	3.7661	3.7661
Second natural frequency (rads^{-1})	8.6446	8.9486	8.7283	8.6665	8.6482	8.6456
Third natural frequency (rads^{-1})	13.5306	15.1873	14.0454	13.6915	13.5760	13.5582

to be $\eta(\zeta, 0) = 0.01\zeta^4$.

Appendix B

Computations of Element Matrices for GE Beams

In this section we derive element mass, velocity convection and stiffness matrices from the weak form as shown in (6.13). We only show the derivation of element mass matrix from the mass operator (6.3). Rest of the element matrices can be obtained through similar kind of manipulations. The mass operator as defined in (6.3) is:

$$G_M(\mathbf{W}, \mathbf{U}) = l^2 \int_0^1 \mathbf{W} \cdot \mathbf{I} \cdot \frac{\partial^2 \mathbf{U}}{\partial t^2} d\zeta, \quad (\text{B.1})$$

We consider an element to be two noded and write the two shape functions as

$$N_i = 1 - \frac{\zeta - \zeta_i}{h^e} \quad \text{and} \quad N_j = \frac{\zeta - \zeta_i}{h^e},$$

where h^e is the length of the element and N_i and N_j are two shape functions, corresponds to an element that spans from ζ_i to ζ_j . We see that at each node, we have three nodal parameters to compute. We express u_1, u_2 and θ in $\zeta_i \leq \zeta \leq \zeta_j$ as

$$\begin{aligned} u_1(\zeta, t) &= N_i(\zeta)q_{u_1}^{(i)}(t) + N_j(\zeta)q_{u_1}^{(j)}(t), \\ u_2(\zeta, t) &= N_i(\zeta)q_{u_2}^{(i)}(t) + N_j(\zeta)q_{u_2}^{(j)}(t) \\ \text{and} \quad \theta(\zeta, t) &= N_i(\zeta)q_{\theta}^{(i)}(t) + N_j(\zeta)q_{\theta}^{(j)}(t), \end{aligned}$$

respectively. This enables us to express \mathbf{U} in matrix form as

$$[\mathbf{U}] = \begin{bmatrix} N_i & 0 & 0 & N_j & 0 & 0 \\ 0 & N_i & 0 & 0 & N_j & 0 \\ 0 & 0 & N_i & 0 & 0 & N_j \end{bmatrix} \begin{bmatrix} q_{u_1}^{(i)} \\ q_{u_2}^{(i)} \\ q_{\theta}^{(i)} \\ q_{u_1}^{(j)} \\ q_{u_2}^{(j)} \\ q_{\theta}^{(j)} \end{bmatrix},$$

where $\zeta_i \leq \zeta \leq \zeta_j$. Because we employ Glaerkin projection, the weighting functions \mathbf{W} are taken to be same as \mathbf{U} . Thus, we express \mathbf{W} as in matrix form as

$$[\mathbf{W}] = \begin{bmatrix} N_i & 0 & 0 \\ 0 & N_i & 0 \\ 0 & 0 & N_i \\ N_j & 0 & 0 \\ 0 & N_j & 0 \\ 0 & 0 & N_j \end{bmatrix}.$$

Substituting $[\mathbf{U}]$, $[\mathbf{W}]$ and $[\mathbf{I}]$ in (B.1) we obtain

$$[\mathbf{G}]_{\text{M}} = l^2 \int_{\zeta_i}^{\zeta_j} \begin{bmatrix} N_i & 0 & 0 \\ 0 & N_i & 0 \\ 0 & 0 & N_i \\ N_j & 0 & 0 \\ 0 & N_j & 0 \\ 0 & 0 & N_j \end{bmatrix} \begin{bmatrix} A_{\rho} & 0 & 0 \\ 0 & A_{\rho} & 0 \\ 0 & 0 & I_{\rho} \end{bmatrix} \begin{bmatrix} N_i & 0 & 0 & N_j & 0 & 0 \\ 0 & N_i & 0 & 0 & N_j & 0 \\ 0 & 0 & N_i & 0 & 0 & N_j \end{bmatrix} \begin{bmatrix} \ddot{q}_{u_1}^{(i)} \\ \ddot{q}_{u_2}^{(i)} \\ \ddot{q}_{\theta}^{(i)} \\ \ddot{q}_{u_1}^{(j)} \\ \ddot{q}_{u_2}^{(j)} \\ \ddot{q}_{\theta}^{(j)} \end{bmatrix} d\zeta.$$

We express the above in convenient form as

$$[\mathbf{G}]_{\text{M}} = [\mathbf{M}] \{\ddot{\mathbf{q}}\}, \quad (\text{B.2})$$

where $[\mathbf{M}]$ is the element mass matrix:

$$[\mathbf{M}] = l^2 \int_{\zeta_i}^{\zeta_j} \begin{bmatrix} A_\rho N_i^2 & 0 & 0 & A_\rho N_i N_j & 0 & 0 \\ 0 & A_\rho N_i^2 & 0 & 0 & A_\rho N_i N_j & 0 \\ 0 & 0 & I_\rho N_i^2 & 0 & 0 & I_\rho N_i N_j \\ A_\rho N_j N_i & 0 & 0 & A_\rho N_j^2 & 0 & 0 \\ 0 & A_\rho N_j N_i & 0 & 0 & A_\rho N_j^2 & 0 \\ 0 & 0 & I_\rho N_j N_i & 0 & 0 & I_\rho N_j^2 \end{bmatrix} d\zeta.$$

The above is further expressed in convenient form:

$$[\mathbf{M}] = l^2 \begin{bmatrix} [\mathbf{M}^{(ii)}] & [\mathbf{M}^{(ij)}] \\ [\mathbf{M}^{(ji)}] & [\mathbf{M}^{(jj)}] \end{bmatrix},$$

where

$$[\mathbf{M}^{(\alpha\beta)}] = \int_{\zeta_1}^{\zeta_2} [\mathbf{N}_\alpha][\mathbf{I}][\mathbf{N}_\beta] d\zeta,$$

with $\alpha, \beta = i, j$ and $[\mathbf{N}_\alpha]$ is defined as

$$[\mathbf{N}_\alpha] = \begin{bmatrix} N_\alpha & 0 & 0 \\ 0 & N_\alpha & 0 \\ 0 & 0 & N_\alpha \end{bmatrix}.$$

Similarly, expressions for element velocity convection and stiffness matrices can be calculated.

Appendix C

MATLAB Code for Lengthening/Shortening GE Cables

```
1 % Code for an Axially Lengthening/Shortening GE Cantilever Beam
2 % Rates of lengthening/shortening are taken to be constant
3 clear all;
4 tic
5 global EA GA EI vel L EA2 GA2 EI2 el tim EIR
6 % Newmark time marching scheme constants
7 beta = 0.25; delta = 0.5;
8 %% -----
9 % Length and no of elements
10 L0=1; el=10; node=el+1;
11 mu = 0; % Damping ratio
12 tol = 1e-5; %convergence tolerance
13 l=1/el;
14 ma = 10; % dimensionless mass of the aerostat
15 rad = 1; % dimensionless radius of the aerostat
16 %% -----
17 % Material Properties
18 EA1 = 10^8; GA1 = EA1;
19 EI1 = 10^4;
20 % physical properties
21 EA2 = EA1/EI1; GA2 = EA1/EI1; EI2 = 1;
22 EA = EA1/EI1; GA =EA1/EI1; EI = 1;EIR = 1;
23 deltt = 0.1; % time step
24 vel=0.0; % rate of lengthening/shortening
25 m=1; tt=0;vv=0;
26 t =0;
27 %% -----
```

```

28 % Initial conditions
29 u = zeros(node,1); v=zeros(node,1); th = zeros(node,1);
30 du = zeros(node,1); dv=zeros(node,1); dth = zeros(node,1);
31 ddu = zeros(node,1); ddv=zeros(node,1); ddth = zeros(node,1);
32 %% -----
33 %% Time marching starts here
34 while (t<=10)
35     tim = t;
36     L = L0+vel*t;
37     %% Remesh the integration domain in each iteration
38     eel = 1-(5/el)*(L0/L);
39     eell = eel/(el-1);
40     sx = (0:1:1)';
41     %% -----
42     %% Construct global mass stiffness and gyroscopic matrices
43     Mg = zeros(3*node,3*node);
44     Gg = zeros(3*node,3*node); Sg = zeros(3*node,3*node); Kg = zeros(3*node
,3*node);
45     for i=1:1:length(sx)-1
46         [me,de,se] = elmass(sx(i),sx(i+1));
47         Mg(3*i-2:3*i+3,3*i-2:3*i+3)=me+ Mg(3*i-2:3*i+3,3*i-2:3*i+3);
48         Gg(3*i-2:3*i+3,3*i-2:3*i+3)=de+ Gg(3*i-2:3*i+3,3*i-2:3*i+3);
49         Sg(3*i-2:3*i+3,3*i-2:3*i+3)=se+ Sg(3*i-2:3*i+3,3*i-2:3*i+3);
50     end
51     %% Lumped mass at the end tip
52     Mg(end-2:end,end-2:end) = Mg(end-2:end,end-2:end)+[ma 0 0; 0 ma 0; 0 0
0];
53     Mgext = Mg(4:3*node,4:3*node);
54     Ggext = Gg(4:3*node,4:3*node);
55     Sgext = Sg(4:3*node,4:3*node);
56     Dgext = Ggext;
57     %% -----
58     b = 1; e=0; ke=0; pe=0; am = 0;
59     %% -----
60     ddu1 = -(du/(delt*beta)+((0.5-beta)/beta)*ddu);
61     du = du +delt*((1-delta)*ddu+delta*ddu1);
62     ddu = ddu1;
63     ddv1 = -(dv/(delt*beta)+((0.5-beta)/beta)*ddv);
64     dv = dv +delt*((1-delta)*ddv+delta*ddv1);
65     ddv = ddv1;
66     ddth1 = -(dth/(delt*beta)+((0.5-beta)/beta)*ddth);
67     dth = dth +delt*((1-delta)*ddth+delta*ddth1);
68     ddth = ddth1;
69     %% -----

```

```

70     num=1;
71     while(b>tol)
72         if (length(b)>500)
73             pause
74         end
75         R=zeros(3*node); FA =zeros(3*node);
76         Kg = zeros(3*node,3*node);
77         %% Global stiffness matrix
78         for i=1:1:el
79             pp=i;
80             [k,r,fa] = elstiff(pp,u(i,1),v(i,1),th(i,1),u(i+1,1),v(i+1,1),
th(i+1,1),sx(i),sx(i+1));
81             Kg(3*i-2:3*i+3,3*i-2:3*i+3)=k + Kg(3*i-2:3*i+3,3*i-2:3*i+3);
82             R(3*i-2:3*i+3,1)= r + R(3*i-2:3*i+3,1);
83             FA(3*i-2:3*i+3,1)= fa + FA(3*i-2:3*i+3,1);
84         end
85         R1 = R(4:3*node,1);
86         FA1 = FA(4:3*node,1);
87         Rext=zeros(length(R1),1);
88         Kgext = Kg(4:3*node,4:3*node);
89         Rext(end,1) = R1(end,1);
90         K =(Kgext+(1/(beta*delt^2))*Mgext+(delta/(delt*beta))*Dgext+Sgext);
91         f = zeros((3*node-3),1);
92         %% -----
93         a = zeros(length(f),1); c = zeros(length(f),1); di = zeros(length(f)
,1);
94         for j=2:1:(node)
95             a(3*j-5,1)=ddu(j,1); c(3*j-5,1)=du(j,1); di(3*j-5,1)=u(j,1);
96             a(3*j-4,1)=ddv(j,1); c(3*j-4,1)=dv(j,1); di(3*j-4,1)=v(j,1);
97             a(3*j-3,1)=ddth(j,1); c(3*j-3,1)=dth(j,1); di(3*j-3,1)=th(j,1);
98         end
99         %% -----
100        f(end-2) = 1000/EIR+f(end-2); % constant upward pull
101        if (t<.25)
102            f(end-1) = f(end-1)+0.1/.25/EIR*t; % small initial perturbation
103        end
104        %% -----
105        f=L*f+FA1;
106        Dgext = Ggext;
107        f1 = f-R1-Mgext*a-Dgext*c-Sgext*di;
108        delp = K\f1;
109        b(num)=norm(f1);
110        q=norm(delp);
111        %% -----

```

```

112     u = u + [0; delp(1:3:(length(delp)-2),1)];
113     v = v + [0; delp(2:3:(length(delp)-1),1)];
114     th = th + [0; delp(3:3:(length(delp)),1)];
115     du = du + (delta/(delt*beta))*[0; delp(1:3:(length(delp)-2),1)];
116     dv = dv + (delta/(delt*beta))*[0; delp(2:3:(length(delp)-1),1)];
117     dth = dth + (delta/(delt*beta))*[0; delp(3:3:(length(delp)),1)];
118     ddu = ddu + (1/(beta*delt^2))*[0; delp(1:3:(length(delp)-2),1)];
119     ddv = ddv + (1/(beta*delt^2))*[0; delp(2:3:(length(delp)-1),1)];
120     ddth = ddth + (1/(beta*delt^2))*[0; delp(3:3:(length(delp)),1)];
121     num=num+1;
122     %% -----
123     end
124     %% -----
125     % Calculate total energy, angular momentum and end moment
126     for i=1:l:el
127         zz = elenergy(u(i),u(i+1),v(i),v(i+1),th(i),th(i+1),du(i),du(i+1),
dv(i),dv(i+1),dth(i),dth(i+1),sx(i),sx(i+1)) );
128         aa = elangum(u(i),u(i+1),v(i),v(i+1),th(i),th(i+1),du(i),du(i+1),
dv(i),dv(i+1),dth(i),dth(i+1),sx(i),sx(i+1)) );
129         e = e + zz(1);
130         ke = ke +zz(2);
131         pe = pe + zz(3);
132         am = am+aa;
133     end
134     amm(m) = am;
135     Lam = [cos(th(2)/2) -sin(th(2)/2); sin(th(2)/2) cos(th(2)/2)];
136     C = [EA 0; 0 GA];
137     n = Lam*C*Lam'*[1+u(2)/(1*L)-cos(th(2)/2); v(2)/(1*L)-sin(th(2)/2)];
138     mom(m) = -EI*(th(2))/(1*L)+n(1)*v(2)-n(2)*(10-L+L*1/2+u(2));
139     en(m) = e;
140     enk(m) = ke;
141     enp(m) = pe;
142     %% -----
143     vv(m)=v(end); uu(m)=u(end); tth(m) = th(end);
144     dvv(m)=dv(end);
145     y=v; tt(m)=t; hh(m)=L;
146     n=1;
147     for n=1:l:length(u)
148         x(n)=sx(n)*L+u(n);
149     end
150     xcr(m) = x(end); ycr(m) = y(end);
151     %% -----
152     %% -----
153     % Animation

```

```

154     hold on;
155     h1 = plot(y(1:end-1),x(1:end-1),'b','LineWidth',3);
156     h11 = plot(y(end-1:end),x(end-1:end),'r','LineWidth',3);
157     h12 = plot(y(end),x(end),'ro','LineWidth',1);
158     h2 = plot(y(end),x(end),'k','LineWidth',1);
159     str = ['time = ' num2str(t) 's'];
160     h3 = text(0,39.00,str,'FontSize',14,'FontName','Palatino Linotype');
161     axis([-30.5 30.5 -0.5 30.5 ])
162     P(m)=getframe;
163     delete(h1)
164     delete(h11)
165     delete(h12)
166     delete(h3)
167     %% -----
168     t=t+delt;
169     m=m+1;
170 end
171 movie(P,1,60)
172 movie2avi(P, 'myPeaks.avi', 'compression', 'None');
173 toc

```

```

1 function z = gauss3p(fun,l,u)
2 % Routine for single point Gauus quadrature
3 xbar = (l+u)/2; h = (u-l)/2;
4 z=2*feval(fun,xbar)*h;

```

```

1 function [me,de,se] = elmass(x1,x2)
2 % Function to numerically integrate "emass", "gyro" and "stiff" functions
3 global h xx
4 xx=x1;
5 h=x2-x1;
6 me = gauss3p('emass',x1,x2);
7 de = gauss3p('gyro',x1,x2);
8 se = gauss3p('stiff',x1,x2);

```

```

1 function z = emass(x)
2 % Function to compute element mass matrices
3 global h A I xx L
4 x1=xx;
5 A = 1; I = 10;
6 S1 = (h-(x-x1))/(h);
7 S2 =(x-x1)/(h);
8 psi = [S1 0 0 S2 0 0; 0 S1 0 0 S2 0; 0 0 S1 0 0 S2];
9 M = [A 0 0; 0 A 0; 0 0 I];

```

```
10 z =L^2*psi 'M*psi;
```

```
1 function z = gyro(x)
2 % Function to compute the element velocity convection matrices
3 global vel xx h A I L
4 x1=xx;
5 S1 = (h-(x-x1))/(h);
6 S2 = (x-x1)/(h);
7 ps1 = [S1 0 0; 0 S1 0; 0 0 S1]; ps2 = [S2 0 0; 0 S2 0; 0 0 S2];
8 dps1 = [-1/h 0 0; 0 -1/h 0; 0 0 -1/h]; dps2 = [1/h 0 0; 0 1/h 0; 0 0 1/h];
9 D = [A 0 0; 0 A 0; 0 0 I];
10 zz11 = ps1 *(D*dps1)-dps1 *(D*ps1); zz12 = ps1 *(D*dps2)-dps1 *(D*ps2);
11 zz21 = ps2 *(D*dps1)-dps2 *(D*ps1); zz22 = ps2 *(D*dps2)-dps2 *(D*ps2);
12 z = (L*vel*(1-x))*[zz11 zz12; zz21 zz22];
```

```
1 function z = stiff(x)
2 % Function to compute linear element stiffness matrix
3 global vel xx h A I
4 x1=xx;
5 S1 = (h-(x-x1))/(h);
6 S2 = (x-x1)/(h);
7 dps1 = [-1/h 0 0 1/h 0 0; 0 -1/h 0 0 1/h 0; 0 0 -1/h 0 0 1/h];
8 D = [A 0 0; 0 A 0; 0 0 I];
9 z = -vel^2*(1-x)^2*dps1 *D*dps1;
```

```
1 function [ke,pd,fa] = elstiff(pp,v1,v2,t1,w1,w2,t2,x1,x2)
2 % Function to numerically integrate "stmat", "stgeo", "res" and "fappl"
3 % functions
4 global u11 u12 theta1 h u21 u22 theta2 xx ii
5 ii=pp;
6 u11 = v1; u12 = v2; theta1 = t1; u21 = w1; u22 = w2; theta2 = t2; xx=x1;
7 h=x2-x1;
8 k1 = gauss3p('stmat',x1,x2);
9 k2 = gauss3p('stgeo',x1,x2);
10 ke = k1+k2;
11 z1 = gauss3p('res',x1,x2);
12 pd = z1;
13 fa = gauss3p('fappl',x1,x2);
```

```
1 function z = stmat(x)
2 % Function to compute first part of the linearised stiffness matrix
3 global u11 u12 theta1 h u21 u22 theta2 EA GA EI xx L ii el EA2 GA2 EI2
4 x1=xx;
5 uu11=u11; uu12=u12; th1=theta1; uu21 = u21; uu22 = u22; th2 = theta2;
```

```

6 N1 = (h-(x-x1))/h; N2 = (x-x1)/h;
7 lam = [cos(th1*N1+th2*N2) -sin(th1*N1+th2*N2) 0; sin(th1*N1+th2*N2) cos(th1
      *N1+th2*N2) 0; 0 0 1];
8 if(ii < e1)
9 C = [EA 0 0; 0 GA 0; 0 0 EI];
10 D1 = [-1/h 0 (uu22-uu12)*N1/(h);
11 0 -1/h -(L+(uu21-uu11)/h)*N1;
12 0 0 -1/h ];
13 D2 = [1/h 0 (uu22-uu12)*N2/(h);
14 0 1/h -(L+(uu21-uu11)/h)*N2;
15 0 0 1/h ];
16 z11 = D1'*(lam*C*lam'*D1); z12 = D1'*(lam*C*lam'*D2);
17 z22 = D2'*(lam*C*lam'*D2); z21 = D2'*(lam*C*lam'*D1);
18 z = [z11 z12; z21 z22];
19 else
20 C = [EA2 0 0; 0 GA2 0; 0 0 EI2];
21 D1 = [-1/h 0 (uu22-uu12)*N1/(h);
22 0 -1/h -(L+(uu21-uu11)/h)*N1;
23 0 0 -1/h ];
24 D2 = [1/h 0 (uu22-uu12)*N2/(h);
25 0 1/h -(L+(uu21-uu11)/h)*N2;
26 0 0 1/h ];
27 z11 = D1'*(lam*C*lam'*D1); z12 = D1'*(lam*C*lam'*D2);
28 z22 = D2'*(lam*C*lam'*D2); z21 = D2'*(lam*C*lam'*D1);
29 z = [z11 z12; z21 z22];
30 end

```

```

1 function z = stgeo(x)
2 % Function to compute second part of the linearised stiffness matrix
3 global u11 u12 theta1 h u21 u22 theta2 EA GA EI xx L ii e1 EA2 GA2 EI2
4 x1=xx;
5 uu11=u11; uu12=u12; th1=theta1; uu21 = u21; uu22 = u22; th2 = theta2;
6 N1 = (h-(x-x1))/h; N2 = (x-x1)/h;
7 lam = [cos(th1*N1+th2*N2) -sin(th1*N1+th2*N2) 0; sin(th1*N1+th2*N2) cos(th1
      *N1+th2*N2) 0; 0 0 1];
8 if(ii < e1)
9 C = [EA 0 0; 0 GA 0; 0 0 EI];
10 N = C*lam'*( [L+(uu21-uu11)/h ; (uu22-uu12)/h ; (th2-th1)/h] -[L*cos(th1*N1+
      th2*N2); L*sin(th1*N1+th2*N2); 0] );
11 n = lam*N;
12 G = [0 0 -n(2,1); 0 0 n(1,1); -n(2,1) n(1,1) -((L+(uu21-uu11)/(h))*n(1,1)+(
      uu22-uu12)*n(2,1)/(h))];
13 D11 = [-1/h 0 0 ; 0 -1/h 0 ; 0 0 N1] ;
14 D22 = [1/h 0 0 ; 0 1/h 0 ; 0 0 N2] ;

```

```

15 z11= D11'*(G*D11); z12 = D11'*(G*D22);
16 z22 = D22'*(G*D22); z21 = D22'*(G*D11);
17 z = [z11 z12; z21 z22];
18 else
19 C = [EA2 0 0; 0 GA2 0; 0 0 EI2];
20 N = C*lam'*( [L+(uu21-uu11)/h ; (uu22-uu12)/h ; (th2-th1)/h ] -[L*cos(th1*N1+
      th2*N2); L*sin(th1*N1+th2*N2); 0]);
21 n = lam*N;
22 G = [0 0 -n(2,1); 0 0 n(1,1); -n(2,1) n(1,1) -((L+(uu21-uu11)/(h))*n(1,1)+(
      uu22-uu12)*n(2,1)/(h))];
23 D11 = [-1/h 0 0 ; 0 -1/h 0 ; 0 0 N1 ] ;
24 D22 = [1/h 0 0 ; 0 1/h 0 ; 0 0 N2] ;
25 z11= D11'*(G*D11); z12 = D11'*(G*D22);
26 z22 = D22'*(G*D22); z21 = D22'*(G*D11);
27 z = [z11 z12; z21 z22];
28 end

```

```

1 function z= res(x)
2 % Function to compute the residue column
3 global u11 u12 theta1 h u21 u22 theta2 EA GA EI xx L ii el EA2 GA2 EI2
4 x1=xx;
5 uu11=u11; uu12=u12; th1=theta1; uu21 = u21; uu22 = u22; th2 = theta2;
6 N1 = (h-(x-x1))/h; N2 = (x-x1)/h;
7 lam = [cos(th1*N1+th2*N2) -sin(th1*N1+th2*N2) 0; sin(th1*N1+th2*N2) cos(th1
      *N1+th2*N2) 0; 0 0 1];
8 if(ii<el)
9 C= [EA 0 0; 0 GA 0; 0 0 EI];
10 N = C*lam'*( [L+(uu21-uu11)/h ; (uu22-uu12)/h ; (th2-th1)/h ] -[L*cos(th1*N1+
      th2*N2); L*sin(th1*N1+th2*N2); 0]);
11 n = lam*N;
12 D1 = [-1/h 0 (uu22-uu12)*N1/(h);
13 0 -1/h -(L+(uu21-uu11)/h)*N1;
14 0 0 -1/h ];
15 D2 = [1/h 0 (uu22-uu12)*N2/(h);
16 0 1/h -(L+(uu21-uu11)/h)*N2;
17 0 0 1/h ];
18 z1= D1'*n;
19 z2= D2'*n;
20 z=[z1(1); z1(2); z1(3); z2(1); z2(2); z2(3)];
21 else
22 C= [EA2 0 0; 0 GA2 0; 0 0 EI2];
23 N = C*lam'*( [L+(uu21-uu11)/h ; (uu22-uu12)/h ; (th2-th1)/h ] -[L*cos(th1*N1+
      th2*N2); L*sin(th1*N1+th2*N2); 0]);
24 n = lam*N;

```

```

25 D1 = [-1/h  0      (uu22-uu12)*N1/(h);
26      0  -1/h  -(L+(uu21-uu11)/h)*N1;
27      0   0      -1/h  ];
28 D2 = [1/h  0      (uu22-uu12)*N2/(h);
29      0  1/h  -(L+(uu21-uu11)/h)*N2;
30      0   0      1/h  ];
31 z1= D1'*n;
32 z2= D2'*n;
33 z=[z1(1); z1(2); z1(3); z2(1); z2(2); z2(3)];
34 end

```

```

1 function z = fappl(x)
2 % Function to compute total externally applied body forces
3 global h xx L A
4 x1 = xx;
5 N1 = (h-(x-x1))/h; N2 = (x-x1)/h;
6 z1 = (1*L^2)*[ -9.81*A*N1 ; 0; 0; -9.81*A*N2 ; 0 ; 0];
7 z = z1;

```

```

1 function E = elangum(uu1,uu2,vv1,vv2,tth1,tth2,uud1,uud2, vvd1, vvd2, ttd1,
    ttd2,x1,x2)
2 % Function to numerically integrate "angm" function
3 global xx ud1 ud2 td1 td2 u1 u2 vd1 vd2 v1 v2 th1 th2 h
4 xx = x1; h = x2-x1;
5 ud1 = uud1; ud2 = uud2; td1 = ttd1; td2 = ttd2; u1 = uu1; u2 = uu2;
    vd1 = vvd1;
6 vd2 = vvd2; v1 = vv1; v2 = vv2; th1 = tth1; th2 = tth2;
7 E = gauss2p('angm',x1,x2);

```

```

1 function z= angm(x)
2 % Function to compute total angular momentum of the system
3 global A I xx ud1 ud2 td1 td2 u1 u2 vd1 vd2 v1 v2 th1 th2 h vel L
4 x1=xx;
5 N1 = (h-(x-x1))/h; N2 = (x-x1)/h;
6 z = (A*((10-L+L*x+u1*N1+u2*N2)*((vd1*N1+vd2*N2)+(vel*(1-x)*(v2-v1)/(h*L)))
    -(v1*N1+v2*N2)*((ud1*N1+ud2*N2)+(vel*(1-x)*(u2-u1)/(h*L))+vel))+I*((td1*
    N1+td2*N2)+(vel*(1-x)*(th2-th1)/(h*L))))*L;

```

```

1 function E = elenergy(uu1,uu2,vv1,vv2,tth1,tth2,uud1,uud2, vvd1, vvd2, ttd1
    ,ttd2,x1,x2)
2 % Function to numerically integrate "energy", "kenergy" and "penergy"
3 % functions
4 global xx ud1 ud2 td1 td2 u1 u2 vd1 vd2 v1 v2 th1 th2 h
5 xx = x1; h = x2-x1;

```

```

6 ud1 = uud1; ud2 = uud2; td1 = ttd1; td2 = ttd2; u1 = uu1; u2 = uu2;
  vd1 = vvd1;
7 vd2 = vvd2; v1 = vv1; v2 = vv2; th1 = tth1; th2 = tth2;
8 E = gauss3p('energy',x1,x2);
9 E = [E ; gauss3p('kenenergy',x1,x2)];
10 E = [E ; gauss3p('penenergy',x1,x2)];

```

```

1 function z= energy(x)
2 % Function to compute total energy
3 global EA GA EI A I xx ud1 ud2 td1 td2 v1 v2 th1 th2 h vel L
4 x1=xx;
5 N1 = (h-(x-x1))/h; N2 = (x-x1)/h;
6 K = 0.5*(A*(((ud1*N1+ud2*N2)+(vel*(1-x)*(u2-u1)/(h*L))+vel)^2+((vd1*N1+vd2*
  N2)+(vel*(1-x)*(v2-v1)/(h*L)))^2)+I*((td1*N1+td2*N2)+(vel*(1-x)*(th2-th1
  ))/(h*L)))^2);
7 lam = [cos((th1*N1+th2*N2)) -sin((th1*N1+th2*N2)); sin((th1*N1+th2*N2)) cos
  ((th1*N1+th2*N2))];
8 str = [1+(u2-u1)/(h*L)-cos((th1*N1+th2*N2)) ; (v2-v1)/(h*L)-sin((th1*N1+th2
  *N2))];
9 gamma = lam'*str;
10 P = 0.5*(EA*gamma(1)^2+GA*gamma(2)^2+EI*((th2-th1)/(h*L))^2);
11 z = L*(P+K);

```

```

1 function z= kenergy(x)
2 % Function to compute total kinetic energy
3 global A I xx ud1 ud2 td1 td2 vd1 vd2 h
4 x1=xx;
5 N1 = (h-(x-x1))/h; N2 = (x-x1)/h;
6 K = 0.5*(A*((ud1*N1+ud2*N2)^2+(vd1*N1+vd2*N2)^2)+I*(td1*N1+td2*N2)^2);
7 z = K;

```

```

1 function z= penenergy(x)
2 % Function to compute total potential energy
3 global EA GA EI xx u1 u2 v1 v2 th1 th2 h
4 x1=xx;
5 N1 = (h-(x-x1))/h; N2 = (x-x1)/h;
6 lam = [cos((th1*N1+th2*N2)) -sin((th1*N1+th2*N2)); sin((th1*N1+th2*N2)) cos
  ((th1*N1+th2*N2))];
7 str = [1+(u2-u1)/h-cos((th1*N1+th2*N2)) ; (v2-v1)/h-sin((th1*N1+th2*N2))];
8 gamma = lam'*str;
9 P = 0.5*(EA*gamma(1)^2+GA*gamma(2)^2+EI*((th2-th1)/h)^2);
10 z = P;

```

Bibliography

- TJ Anderson, B Balachandran, and AH Nayfeh. Nonlinear resonances in a flexible cantilever beam. *Journal of Vibration and Acoustics*, 116(4):480–484, 1994.
- SS Antman. The theory of rods. In *Linear Theories of Elasticity and Thermoelasticity*, pages 641–703. Springer, 1973.
- CM Bender and SA Orszag. *Advanced Mathematical Methods for Scientists and Engineers I*. Springer Science & Business Media, 1999.
- P Betsch and P Steinmann. Frame-indifferent beam finite elements based upon the geometrically exact beam theory. *International journal for numerical methods in engineering*, 54(12):1775–1788, 2002.
- M Brand and MB Rubin. A constrained theory of a cosserat point for the numerical solution of dynamic problems of non-linear elastic rods with rigid cross-sections. *International Journal of Non-Linear Mechanics*, 42(2):216–232, 2007.
- DQ Cao and RW Tucker. Nonlinear dynamics of elastic rods using the cosserat theory: modelling and simulation. *International Journal of Solids and Structures*, 45(2):460–477, 2008.
- DQ Cao, D Liu, and C H-T Wang. Three-dimensional nonlinear dynamics of slender structures: Cosserat rod element approach. *International Journal of Solids and Structures*, 43(3):760–783, 2006.
- J Chung, CS Han, and K Yi. Vibration of an axially moving string with geometric non-linearity and translating acceleration. *Journal of Sound and Vibration*, 240(4):733–746, 2001.
- J Cooper. Asymptotic behavior for the vibrating string with a moving boundary. *Journal of mathematical analysis and applications*, 174(1):67–87, 1993.
- S Corrsin and J Lumley. On the equation of motion for a particle in turbulent fluid. *Applied Scientific Research*, 6(2):114–116, 1956.

- CA González-Cruz, JC Jauregui-Correa, and G Herrera-Ruiz. Nonlinear response of cantilever beams due to large geometric deformations: Experimental validation. *Strojniški vestnik—Journal of Mechanical Engineering*, 62(3):187–196, 2016.
- F Gosselin, MP Paidoussis, and AK Misra. Stability of a deploying/extruding beam in dense fluid. *Journal of sound and vibration*, 299(1):123–142, 2007.
- P Hagedorn and A Dasgupta. *Vibrations and waves in continuous mechanical systems*. John Wiley & Sons, 2007.
- W Hahn. On difference differential equations with periodic coefficients. *Journal of Mathematical Analysis and Applications*, 3(1):70–101, 1961.
- EJ Hinch. *Perturbation methods*. Cambridge university press, 1991.
- P Jung, S Leyendecker, J Linn, and M Ortiz. A discrete mechanics approach to the cosserat rod theory—part 1: static equilibria. *International journal for numerical methods in engineering*, 85(1):31–60, 2011.
- A Kumaniecka and J Nizioł. Dynamic stability of a rope with slow variability of the parameters. *Journal of sound and vibration*, 178(2):211–226, 1994.
- J La Salle, S Lefschetz, and RC Alverson. Stability by liapunov’s direct method with applications. *Physics Today*, 15:59, 1962.
- JP LaSalle. Stability theory for ordinary differential equations. *Journal of Differential Equations*, 4(1):57–65, 1968.
- JP LaSalle and S Lefschetz. *Stability by Liapunov’s direct method: with applications*, volume 4. Academic Press New York, 1961.
- MR Maxey and JJ Riley. Equation of motion for a small rigid sphere in a nonuniform flow. *Physics of Fluids (1958-1988)*, 26(4):883–889, 1983.
- T Most, C Bucher, and Y Schorling. Dynamic stability analysis of non-linear structures with geometrical imperfections under random loading. *Journal of Sound and Vibration*, 276(1):381–400, 2004.
- P Nawrotzki and C Eller. Numerical stability analysis in structural dynamics. *Computer Methods in Applied Mechanics and Engineering*, 189(3):915–929, 2000.
- AH Nayfeh, MI Younis, and EM Abdel-Rahman. Reduced-order models for mems applications. *Nonlinear dynamics*, 41(1-3):211–236, 2005.
- RG Parker. Supercritical speed stability of the trivial equilibrium of an axially-moving string on an elastic foundation. *Journal of Sound and Vibration*, 221(2):205–219, 1999.

- E Reissner. On one-dimensional large-displacement finite-strain beam theory. *Studies in applied mathematics*, 52(2):87–95, 1973.
- A Roy and A Chatterjee. Vibrations of a beam in variable contact with a flat surface. *Journal of Vibration and Acoustics*, 131(4):041010, 2009.
- JC Simo. A finite strain beam formulation. the three-dimensional dynamic problem. part i. *Computer methods in applied mechanics and engineering*, 49(1):55–70, 1985.
- JC Simo and L Vu-Quoc. On the dynamics of flexible beams under large overall motions—the plane case: Part i. *Journal of Applied Mechanics*, 53(4):849–854, 1986a.
- JC Simo and L Vu-Quoc. On the dynamics of flexible beams under large overall motions—the plane case: Part ii. *Journal of Applied Mechanics*, 53(4):855–863, 1986b.
- JC Simo and L Vu-Quoc. A three-dimensional finite-strain rod model. part ii: Computational aspects. *Computer methods in applied mechanics and engineering*, 58(1):79–116, 1986c.
- JC Simo and L Vu-Quoc. On the dynamics in space of rods undergoing large motions—a geometrically exact approach. *Computer methods in applied mechanics and engineering*, 66(2):125–161, 1988.
- JC Simo and KK Wong. Unconditionally stable algorithms for rigid body dynamics that exactly preserve energy and momentum. *International Journal for Numerical Methods in Engineering*, 31(1):19–52, 1991.
- A Stokes. A floquet theory for functional differential equation. *Proceedings of The National Academy of Sciences*, 48(8):1330–1334, 1962.
- B Tabarrok, CM Leech, and YI Kim. On the dynamics of an axially moving beam. *Journal of the Franklin Institute*, 297(3):201–220, 1974.
- S Tadikonda and H Baruh. Dynamics and control of a translating flexible beam with a prismatic joint. *Journal of dynamic systems, measurement, and control*, 114(3):422–427, 1992.
- CM Tchen. *Mean value and correlation problems connected with the motion of small particles suspended in a turbulent fluid*. PhD thesis, TU Delft, Delft University of Technology, 1947.
- J Teixeira, B Stevens, CS Bretherton, R Cederwall, JD Doyle, JC Golaz, AAM Holtslag, SA Klein, JK Lundquist, DA Randall, et al. Parameterization of the atmospheric boundary layer. *Bulletin of the American Meteorological Society*, 89(4):453, 2008.
- Y Terumichi, M Ohtsuka, M Yoshizawa, Y Fukawa, and Y Tsujioka. Nonstationary vibrations of a string with time-varying length and a mass-spring attached at the lower end. *Nonlinear Dynamics*, 12(1):39–55, 1997.

- M Tjernstrom and AS Smedman. Atmospheric boundary layer. *Journal of geophysical research*, 98(C3):4809–4826, 1993.
- L Vu-Quoc and S Li. Dynamics of sliding geometrically-exact beams: large angle maneuver and parametric resonance. *Computer methods in applied mechanics and engineering*, 120(1):65–118, 1995.
- JA Wickert and CD Mote. Classical vibration analysis of axially moving continua. *Journal of Applied Mechanics*, 57(3):738–744, 1990.
- JA Wickert and CD Mote. Response and discretization methods for axially moving materials. *Applied Mechanics Reviews*, 44(11S):S279–S284, 1991.
- JA Wickert and CD Mote Jr. On the energetics of axially moving continua. *The Journal of the Acoustical Society of America*, 85(3):1365–1368, 1989.
- J Zajaczkowski and J Lipiński. Instability of the motion of a beam of periodically varying length. *Journal of Sound and Vibration*, 63(1):9–18, 1979.
- WD Zhu and J Ni. Energetics and stability of translating media with an arbitrarily varying length. *Journal of Vibration and Acoustics*, 122(3):295–304, 2000.
- WD Zhu, J Ni, and J Huang. Active control of translating media with arbitrarily varying length. *Journal of vibration and acoustics*, 123(3):347–358, 2001.